FERMILAB-THESIS-2005-110

Thesis for the Degree of Doctor of Philosophy

Measurement of B_c Production Cross Section in $p\bar{p}$ Collisions at $\sqrt{s} = 1.96$ TeV

Ilsung Cho

Department of Physics, Major in Particle Physics

The Graduate School

December 2005

The Graduate School
SungKyunKwan University

SUNGKYUNKWAN UNIVERSITY

Measurement of B_c Production Cross Section in $p\bar{p}$ Collisions at $\sqrt{s} = 1.96$ TeV

Ilsung Cho

Department of Physics, Major in Particle Physics
The Graduate School

Supervised by Professor Intae Yu

Approved as a qualified thesis of Ilsung Cho
for the degree of Doctor of Philosophy
by the Evaluation Committee

December 2005

Chairman Prof. Yoonbai Kim

Prof. Young-Il Choi

Prof. DongHee Kim

Prof. Youngjoon Kwon

Prof. Intae Yu

The Graduate School Council, SungKyunKwan University

SUNG KYUN KWAN UNIVERSITY

Thesis advisor
Intae Yu

Author
Ilsung Cho

Measurement of B_c Production Cross Section in $p\bar{p}$ Collisions at $\sqrt{s} = 1.96$ TeV

Abstract

We measured B_c meson production cross section using semileptonic decay channel, $B_c \to J/\psi e\nu$. Background contributions from fake electron, electron from photon pair production and $b\bar{b}$ contamination were estimated using hadron tracks in data and from Monte Carlo simulations. From a J/ψ triggered data sample of $360pb^{-}1$ collected by the CDF II detector, 110.4 ± 15.3 B_c signal events were observed above a background level of $75.1 \pm 4.2 \pm 13.2$. After kinematic acceptance and reconstruction efficiency corrections, the production cross section relative to that of the B^+ meson in the kinematic range of $p_T > 4$ GeV/c and rapidity $\mid y \mid < 1$, $\sigma(B_c) \times BR(B_c \to J/\psi\ell\nu)/\sigma(B) \times BR(B \to J/\psi K)$, was derived to be 0.284 ± 0.040(stat.) $\pm$ 0.043(yield) $\pm$ 0.065(acceptance).

SUNGKYUNKWAN UNIVERSITY

Contents

SUNGKYUNKWAN UNIVERSITY

SUNGKYUNKWAN UNIVERSITY

SUNG KYUN KWAN UNIVERSITY

SUNG KYUN KWAN UNIVERSITY

List of Figures

SUNGKYUNKWAN UNIVERSITY

SUNGKYUNKWAN UNIVERSITY

SUNG KYUN KWAN UNIVERSITY

SUNGKYUNKWAN UNIVERSITY

SUNG KYUN KWAN UNIVERSITY

SUNGKYUNKWAN UNIVERSITY

SUNG KYUN KWAN UNIVERSITY

SUNGKYUNKWAN UNIVERSITY

SUNG KYUN KWAN UNIVERSITY

SUNG KYUN KWAN UNIVERSITY

List of Tables

SUNG KYUN KWAN UNIVERSITY

SUNGKYUNKWAN UNIVERSITY

SUNG KYUN KWAN UNIVERSITY

SUNG KYUN KWAN UNIVERSITY

Chapter 1

Introduction

Theoritical and experimental studies of the heavy quark sector in the Standard Model are of a great interest to complete the whole quantitative picture of fundamental interactions. We need the perfect understanding of QCD interactions binding the quark into hadrons to distinguish the hadronic dynamics at the quark level.

In 1986 the B_c meson decay, containing two heavy quarks of bottom and charm , were considered in the pioneering paper written by Bjorken [1]. Ten years later of his prediction the B_c was discovered by the CDF collaboration [47] and This discovery confirmed the theoretical predictions on its mass, production rate and lifetime.

During the period of upgrate the CDF collaboration have developed its detector according to increasing collision energy and collision rate of the Tevatron. We could expect an increase of statistics of B_c and the precision mesurement of B_c property will provide us with a new understanding in the study of doubly heavy hadrons.

SUNGKYUNKWAN UNIVERSITY

1.1 B_c production at Tevatron

The B_c meson is the ground state of $\bar{b}c$ system which in many respects is an intermediate between charmonium and bottonium systems . However because the B_c mesons carry flavour, they provide a window for studying the heavy-quark dynamics that is very different from those provided by $c\bar{c}$- and $b\bar{b}$-quarkonia

The hadronic production of B_c has been studied by several theoriest in the framework of QCD perturbation theory treating $\bar{b}c$ coupling and wave functions in a nonrelativistic approximation[2, 3, 23, 26, 27, 28, 30].

The production mechanism for $\bar{b}c$ differ from those for $b\bar{b}$, because two heavy quark-antiquark paris must be created in the collision. While a $b\bar{b}$ pair can be created at order α_s^2 by the parton processes $q\bar{q}, gg \to \bar{b}b$, The lowest order mechanisms for creating $\bar{b}c$ are the order-α_s^4 processes $q\bar{q}, gg \to (\bar{b}c)(b\bar{c})$ [29, 31].

The parton subprocess of gluon-gluon fusion, $gg \to B_c^+ + b + \bar{c}$ dominates at Tevatron. Figure 1.3 1.4 1.5 1.61.7 show 36 Feynman diagrams for $gg \to B_c^+ + b + \bar{c}\ \alpha_s^4$ subprocess.

The majority of the B_c mesons at Tevatron are also produced indirectly via the decay of excited $\bar{b}c$ mesons. Because $\bar{b}c$ states have rich spectroscopy of the orbital and angular-momentum exitations ,the excited states cascade down through the spectrum via a sequence of hadronic and electromagnetic transitions until they reach the ground state , which decays via the weak interaction [25, 23].

We can summarize the production of a B_c at Tevatron as proceeding in three steps.

- a $\bar{b}$ and c with small relative momemtum are created by a parton collison
- the $\bar{b}$ and c bind to from the B_c or one of its excited states below the BD threshold
- The excited states all cascade down to the ground state B_c via hadronic

SUNGKYUNKWAN UNIVERSITY

or electro magnetic transition with the emission of photons and pion-pion pairs

Figure 1.1 and 1.2 show the cross section of $\bar{b}c$ mesons. all existing calculation for the cross section of $\bar{b}c$ mesons have been carried out within color-singlet model. The $\bar{b}c$ is assumed to be created in a color-singlet state with the same angular-momentum quantum numbers as the meson. The production of $\bar{b}c$ mesons in the color-singlet model at leading order in α_s was studied in reffernce [29]. The result of the order-α_s^4 color-singlet model calculation for $d\sigma/dp_T$ of the B_c meson at the Tevatron at 1.8 TeV are presented in Figure. 1.1. The cross section integrated over p_T greater than $p_{T\,min}$ is shown in Figure 1.2. The prediction includes the feeddown from B_c^*, but not from any of the higher $\bar{b}c$ states. The cross sections are integrated over $|y| < 1$. In our calculations we used the following values of parameters. The quark masses were taken to be $m_c = 1.5$ GeV and $m_b = 4.8$ GeV. The QCD coupling constant was frozen at the value $\alpha_s = 0.23$, which describes the experimental data of the OPAL Collaboration on the production of additional $c\bar{c}$-pairs in e^+e^--annihilation [4, 5, 6].

The cross-section for B_c mesons is roughly three orders of magnitude smaller than that for B mesons due to the presence of two heavy quark-antiquark pairs in the final state.

1.2 Spectroscopy of B_c

The $\bar{b}c$ states have rich spectroscopy of the orbital and angular-momentum exitations [27]. Below the threshold of the decay into $B-D$ pair, one can expect 16 extremely narrow states which cascadely decay into the ground pseudoscalar state with mass of about 6.3 GeV by radiating photons and pion pairs. The predicted spectrum is shown in Figure 1.9.

The annihilation decays can occure due to weak interactions only and, hence, are suppressed for excited levels. The charm-beauty quarkonium states are intermediate to the charminium and bottomonium systems. the properties

SUNGKYUNKWAN UNIVERSITY

of B_c mesons are a special case in quarkonium spectroscopy as they are the only quarkonia consisting of heavy quarks with different flavors. Because they carry flavor they cannot annihilate into gluons so are more stable with width less than a ~ 100 KeV. Excited B_c states lying below BD(and BD^* or B^*D) threshold can only undergo radiative or hadronic transitions to the ground state B_c which then decays weakly [25]. This result in $\bar{b}c$ system has a rich spectroscopy of orbital and angular-momentum excitations below $B^{(*)}D^{(*)}$ threshold which are more stable than their charmonium and bottomonium states.

The masses of the B_c and the other states in the $\bar{b}c$ spectrum can be predicted using potential models. The basic equation of the model is the rest frame Schrödinger-type equation [27].

$$H|\Psi\rangle = [H_0 + V_{q\bar{q}}(\vec{p},\vec{r})]|\Psi\rangle = E|\Psi\rangle \tag{1.1}$$

where,

$$H_0 = \sqrt{p^2 + m_q^2} + \sqrt{p^2 + m_{barq}^2} \tag{1.2}$$

The effective quark-antiquark potential $V_{q\bar{q}}(\vec{p},\vec{r})$, was found by equating the scattering amplitude of free quarks, using a scattering kernel with the desired Dirac structure, with the effects between bound quarks inside a hadron. Due to relativistic effects the potential is momentum dependent in addition to being coordinate dependent. To first order in $(v/c)^2$, $V_{q\bar{q}}(\vec{p},\vec{r})$ reduces to the standard nonrelativistic result.

$$V_{q\bar{q}}(\vec{p},\vec{r}) \to V(\vec{r}) = H_{q\bar{q}}^{conf} + H_{q\bar{q}}^{cont} + H_{q\bar{q}}^{ten} + H_{q\bar{q}}^{S.O.} \tag{1.3}$$

where

$$H_{q\bar{q}}^{conf} = C + br - \frac{4}{3}\frac{\alpha_s(r)}{r} \tag{1.4}$$

includes the spin-independent linear confinement and Coulomb-like interaction,

SUNGKYUNKWAN UNIVERSITY

$$H_{q\bar{q}}^{cont} = \frac{32\pi}{9}\frac{\alpha_s(r)}{m_q m_{\bar{q}}}\vec{S}_q \cdot \vec{S}_{\bar{q}}\delta^3(\vec{r}) \tag{1.5}$$

is the color contact interaction,

$$H_{q\bar{q}}^{ten} = \frac{4}{3}\frac{\alpha_s(r)}{m_q m_{\bar{q}}}\frac{1}{r^3}\left[\frac{3\vec{S}_q \cdot \vec{r}\vec{S}_{\bar{q}} \cdot \vec{r}}{r^2} - \vec{S}_q \cdot \vec{S}_{\bar{q}}\right] \tag{1.6}$$

is the color tensor interaction,

$$H_{q\bar{q}}^{S.O.} = H_{q\bar{q}}^{S.O.(cm)} + H_{q\bar{q}}^{S.O.(tp)} \tag{1.7}$$

is the spin-orbit interaction with

$$H_{q\bar{q}}^{S.O.(cm)} = \frac{4\alpha_s(r)}{3r^3}\left(\frac{\vec{S}_q}{m_q m_{\bar{q}}} + \frac{\vec{S}_{\bar{q}}}{m_q m_{\bar{q}}} + \frac{\vec{S}_q}{{m^2}_q} + \frac{\vec{S}_{\bar{q}}}{{m^2}_{\bar{q}}}\right) \cdot \vec{L} \tag{1.8}$$

its color magnetic pieces arising from one-gluon exchange and

$$H_{q\bar{q}}^{S.O.(tp)} = -\frac{1}{2r}\frac{\partial H_{q\bar{q}}^{conf}}{\partial r}\left(\frac{\vec{S}_q}{{m^2}_q} + \frac{\vec{S}_{\bar{q}}}{{m^2}_{\bar{q}}}\right) \cdot \vec{L} \tag{1.9}$$

the Thomas precession term. In these formulas $\alpha_s(r)$ is the running coupling constant of QCD.

The predicted B_c mass spectrum from the Hamiltonian is shown in Figure 1.8. The B_c mass is in the range of 6.247 GeV/c^2 - 6.286 GeV/c^2 and the ground state of its mass is 6.271 GeV/c^2 with an uncertainty of 10 MeV/c^2 - 20 MeV/c^2 .

1.3 The decay of B_c and inclusive decay rate

The B_c mesons decay via weak interaction [25]. The weak decay of B_c meson processes can be subdivided into three classes :

SUNGKYUNKWAN UNIVERSITY

- The $\bar{b}$-quark decay with the spectator c-quark($\bar{b} \to X$). This decay result in final states such as $B_c^+ \to J/\psi\pi, J/\psi D_s^+, J/\psi l^+\nu_l$
- The c-quark decay with the spectator $\bar{b}$-quark.($c \to X$) This decay result in final states such as $B_c^+ \to B_s^0\pi^+, B_s^0 l^+\nu$
- The annihilation channel $B_c^+ \to l^+\nu_l(c\bar{s}, u\bar{s})$, where $l = e,\ \mu,\ \tau$.

Figure 1.10 shows Feynmann diagram for the each B_c decay. In the $\bar{b} \to \bar{c}c\bar{s}$ decays one separates also the Pauli interference [1] with the c-quark from the initial state. In accordance with the given classification, the total width is the sum over the partial widths

$$\Gamma(total) = \Gamma(\bar{b} \to X) + \Gamma(c \to X) + \Gamma(\text{ann.}) + \Gamma(\text{PI}) \tag{1.10}$$

The dominant contribution into B_c lifetime comes from the c-quark decays($\sim$ 70%) while the b-quark decays and weak innihilation add about 20% and 10% respectively.

Here is a rough estimate of the B_c width. At now we ingnore the Pauli interference contribution for that.

In the spectator approximation :

$$\Gamma(\bar{b} \to X) = \frac{9G_F^2|V_{cb}|^2 m_b^5}{192\pi^3} \simeq 4.8 \times 10^{-4} eV \tag{1.11}$$

and

$$\Gamma(c \to X) = \frac{5G_F^2|V_{cs}|^2 m_c^5}{192\pi^3} \simeq 3.3 \times 10^{-4} eV \tag{1.12}$$

where we use $|V_{cb}| = 0.0412$, $|V_{cs}| = 0.974$, m_b=4.25 GeV/c^2 , and m_c=0.125 GeV/c^2

Annihilation widths such as $\bar{b}c+ \to l^+\nu_l$ are given by the expression

[1] An interference between different diagrams providing the same final state

SUNG KYUN KWAN UNIVERSITY

$$\Gamma(\text{ann.}) = \sum_{i=\tau,c} \frac{G_F^2}{8\pi} |V_{bc}|^2 f_{B_c}^2 M m_i^2 (1 - m_i^2/m_{Bc}^2)^2 \cdot C_i \ , \tag{1.13}$$

where m_i is the mass of the heavier fermion in the given decay chennel. For lepton channels C_i=1 while for quark channels $C_i = 3|V_{qq'}|^2$. In the nonrelativiatic limit the pseudoscalar decay constant, f_{B_c},is proportional to the wave function at the origin and is given by the van Royen-Weisskopf formula

$$f_{B_c} = \frac{2\sqrt{3}}{M}\psi(0) \tag{1.14}$$

Using the Mock-Meson approach of $f_{B_c} \approx 400 MeV$, which leads to the annihilation width of

$$\Gamma(ann) = 67 \times 10^{-6} eV \tag{1.15}$$

Adding this result to the spectator contributions gives Γ(total)=8.8×10^{-4} eV corresponding to a B_c lifetime of $\tau = 0.75$ ps .which is in rough agreement with the measured value from the CDF run I experiment. Recently a lot of efforts was directed to study the long-lived doubly heavy hadrons [2] on the basis of modern understanding of QCD dynamics in the weak decays of heavy flavors in the framework of today approaches[3]: the Operator Product Expansion, sum rules of QCD [15, 16, 17] and NRQCD [18], and potential models adjusted due to the data on the description of hadrons with a single heavy quark.

The result of calculation for the total B_c width in inclusive Operator Production Expansion method and the exclusive potential model approachs give the values consistent with each other. if one takes into account the largest uncertainty, which comes from the quark masses (especially the charm quark).

The result of calculation is

$$\tau(B_c) = 0.55 \pm 0.15 \text{ ps}, \tag{1.16}$$

[2]Reviews on the physics of B_c meson can be found in refs. [7, 8, 9, 10, 11, 12, 13]

[3]See the program on the heavy flavour physics at Tevatron in [14].

SUNGKYUNKWAN UNIVERSITY

which agrees with the measured value of the B_c lifetime from the CDF Run I. Table 1.1 shows the branching ratio of the B_c decay modes calculated in manner of Operator Production Expansion.

Table 1.1: The branching ratios of the B_c decay modes calculated in the framework of inclusive Operator Production Expansion approach, by summing up the exclusive modes in the potential model [19, 20, 21] and according to the semi-inclusive estimates in the sum rules of QCD and NRQCD [22].

B_c decay mode	OPE, %	PM, %	SR, %
$\bar{b} \to \bar{c}l^+\nu_l$	3.9 ± 1.0	3.7 ± 0.9	2.9 ± 0.3
$\bar{b} \to \bar{c}u\bar{d}$	16.2 ± 4.1	16.7 ± 4.2	13.1 ± 1.3
$\sum \bar{b} \to \bar{c}$	25.0 ± 6.2	25.0 ± 6.2	19.6 ± 1.9
$c \to sl^+\nu_l$	8.5 ± 2.1	10.1 ± 2.5	9.0 ± 0.9
$c \to su\bar{d}$	47.3 ± 11.8	45.4 ± 11.4	54.0 ± 5.4
$\sum c \to s$	64.3 ± 16.1	65.6 ± 16.4	72.0 ± 7.2
$B_c^+ \to \tau^+\nu_\tau$	2.9 ± 0.7	2.0 ± 0.5	1.8 ± 0.2
$B_c^+ \to c\bar{s}$	7.2 ± 1.8	7.2 ± 1.8	6.6 ± 0.7

1.4 Analysis overview

From a J/ψ triggered data sample of 360 pb^{-1} collected by the CDF II detector, we performed the measurement on the B_c production cross section using $B_c \to J/\psi e\nu$ semileptonic decay mode.

To measure the B_c production cross section we started from optimization of the electron identification algorithm by studying the reconstruction efficiency and the fake electron rate using well-identified electron and hadron tracks. The track-based electron-reconstruction algorithm was introduced to identify low elergy electron. Then we estimated the background sizes and shapes with selection criteria developed from experience of $B^+ \to J/\psi K^+$ reconstruction and kinematic properties of the B_c semileptonic decays. We used data directly together with Monte Carlo simulation without looking events in the signal window during the background study. Finally, we opened the box and calculated

SUNGKYUNKWAN UNIVERSITY

the signal excess over the background with pre-defined selection. The relative cross section to the B^+ was calculated from the signal yield after correction of acceptances and reconstruction efficiencies.

In this paper we begin with a summary of the experiment apparatus and particle detection, triggers, data samples and selection criteria for the B_c final state, as well as for background estimate. The event yield and backgrounds from fake electon, residual conversion and $b\bar{b}$ are discussed. We finally give the B_c production cross section relative to that of the B^+ meson.

SUNGKYUNKWAN UNIVERSITY

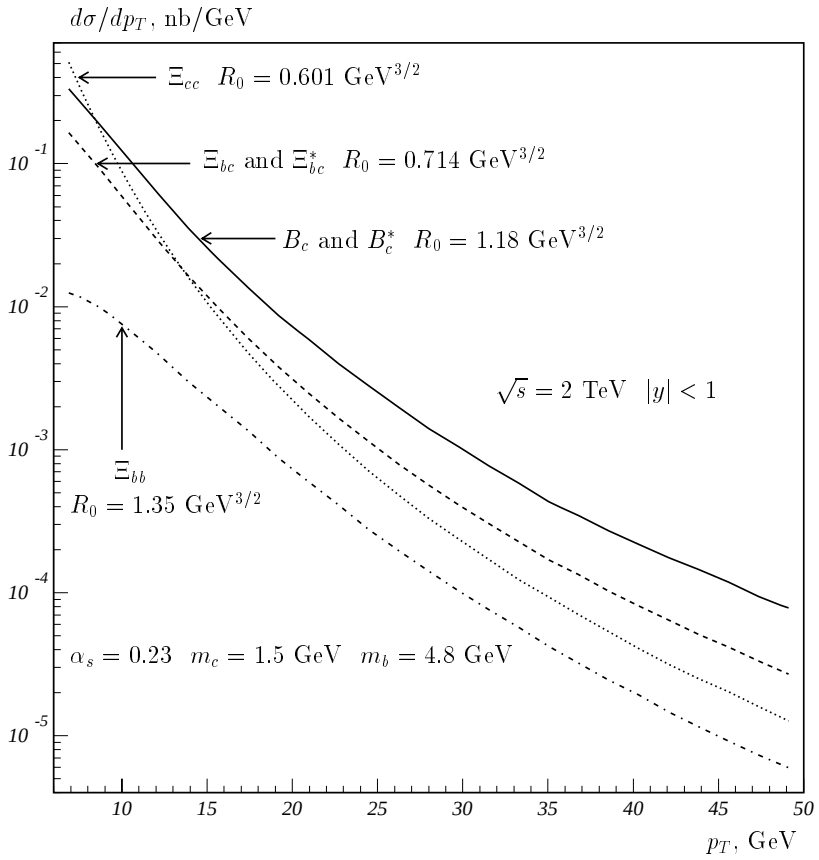

Figure 1.1: Differential cross sections for the B_c meson and doubly-heavy baryons.

SUNGKYUNKWAN UNIVERSITY

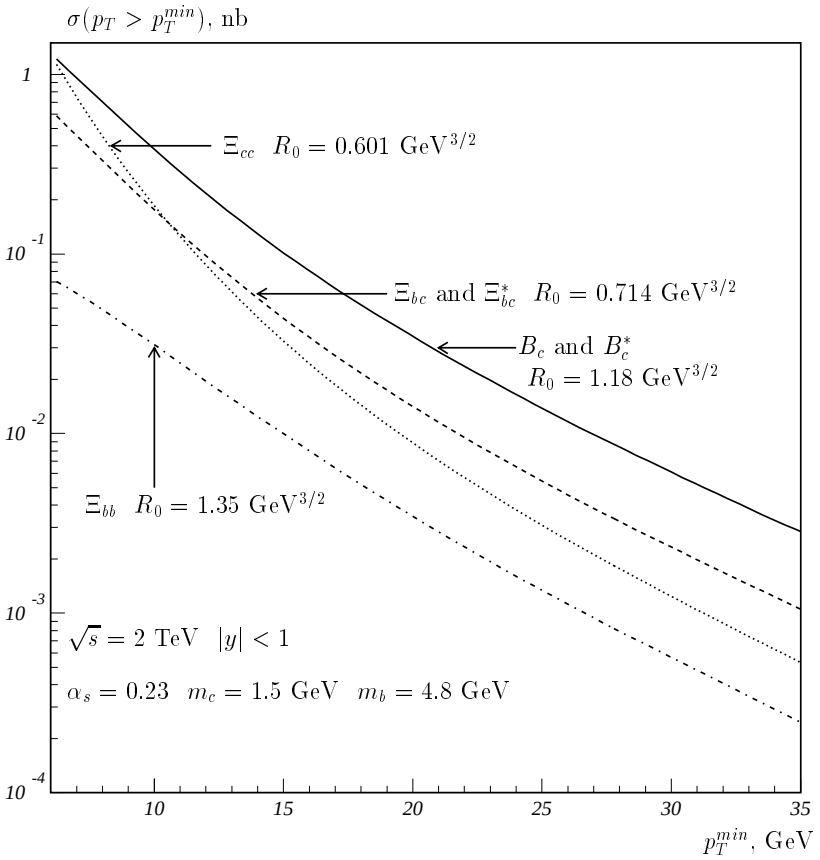

Figure 1.2: Integrated cross sections for the B_c meson and doubly-heavy baryons.

SUNGKYUNKWAN UNIVERSITY

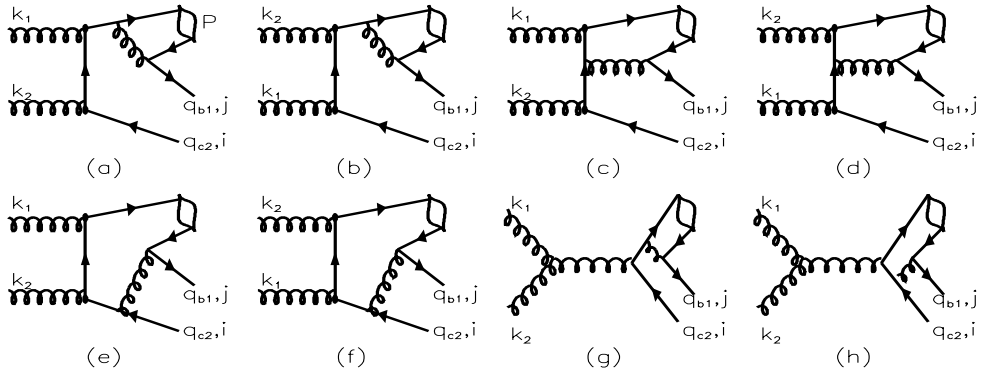

Figure 1.3: Feynman diagrams that can be directly grouped into the cc subset. Here i and j are the color indices of $\bar{c}$ and b respectively.

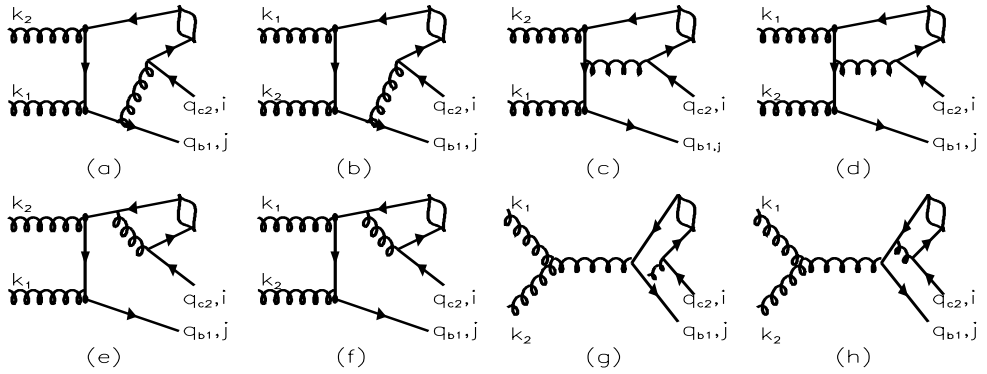

Figure 1.4: Feynman diagrams that can be directly grouped into the bb subset. Here i and j are the color indices of $\bar{c}$ and b respectively.

SUNGKYUNKWAN UNIVERSITY

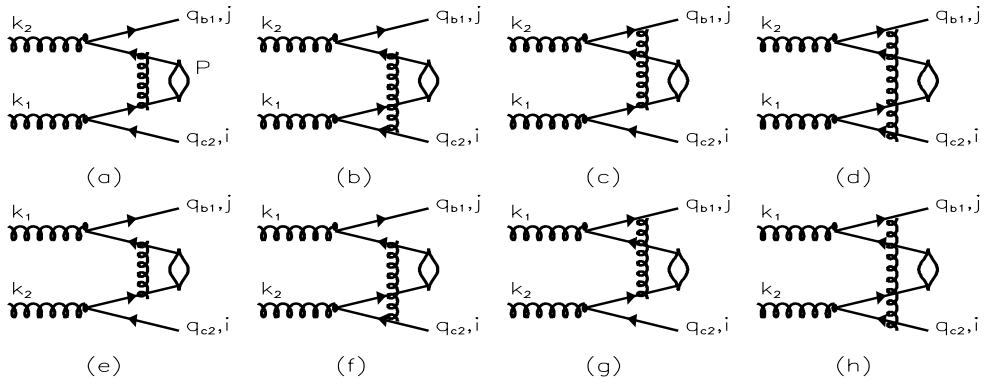

Figure 1.5: Feynman diagrams that can be directly grouped into the cb or bc subsets, where the first four diagrams belong to the cb subset, while the last four belong to the bc subset. Here i and j are the color indices of $\bar{c}$ and b respectively.

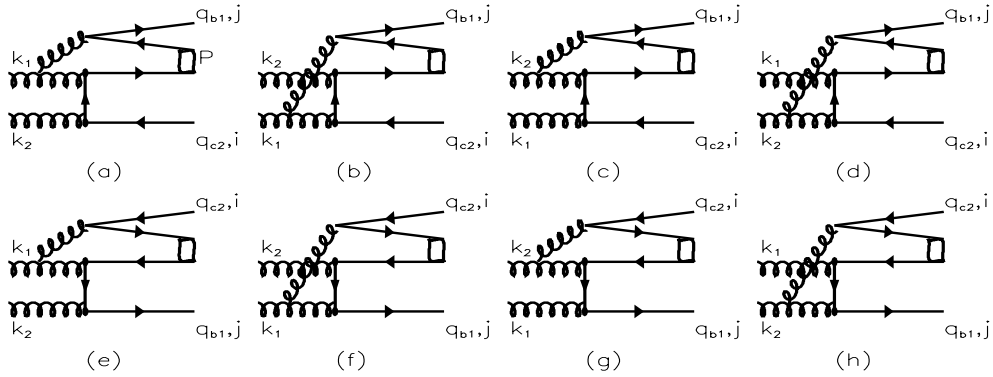

Figure 1.6: Feynman diagrams with only one three-gluon vertex, which can not be directly grouped into the cc, bb, cb and bc subsets. Here i and j are the color indices of $\bar{c}$ and b respectively.

SUNGKYUNKWAN UNIVERSITY

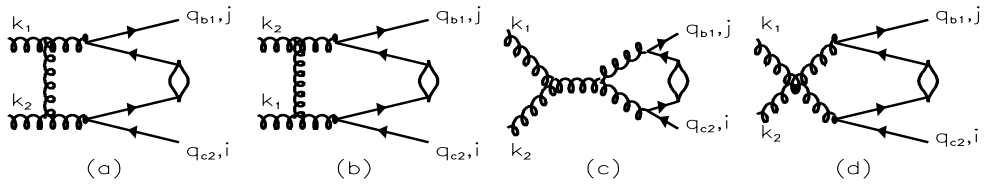

Figure 1.7: Feynman diagrams with two three-gluon vertices or with a four-gluon vertex, which can not be directly grouped into the cc, bb, cb and bc subsets. Here i and j are the color indices of $\bar{c}$ and b respectively.

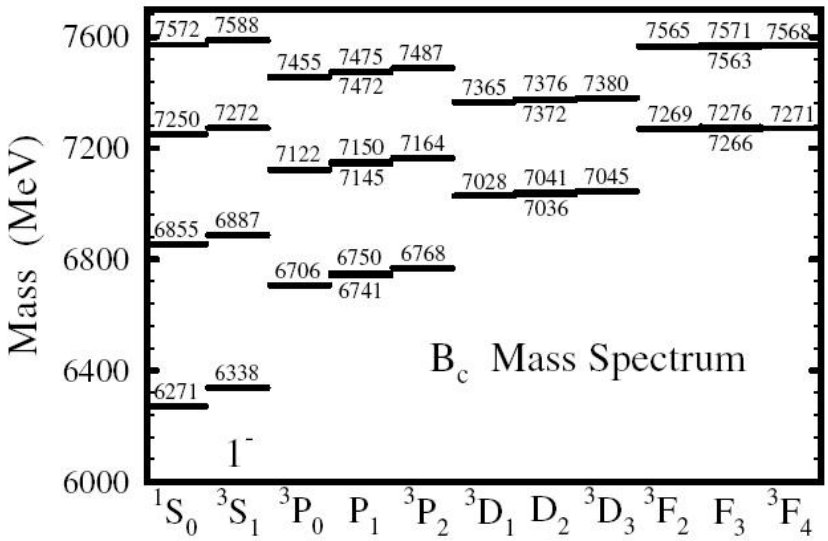

Figure 1.8: The B_c mass spectrum calculated from the potential model [27].

SUNGKYUNKWAN UNIVERSITY

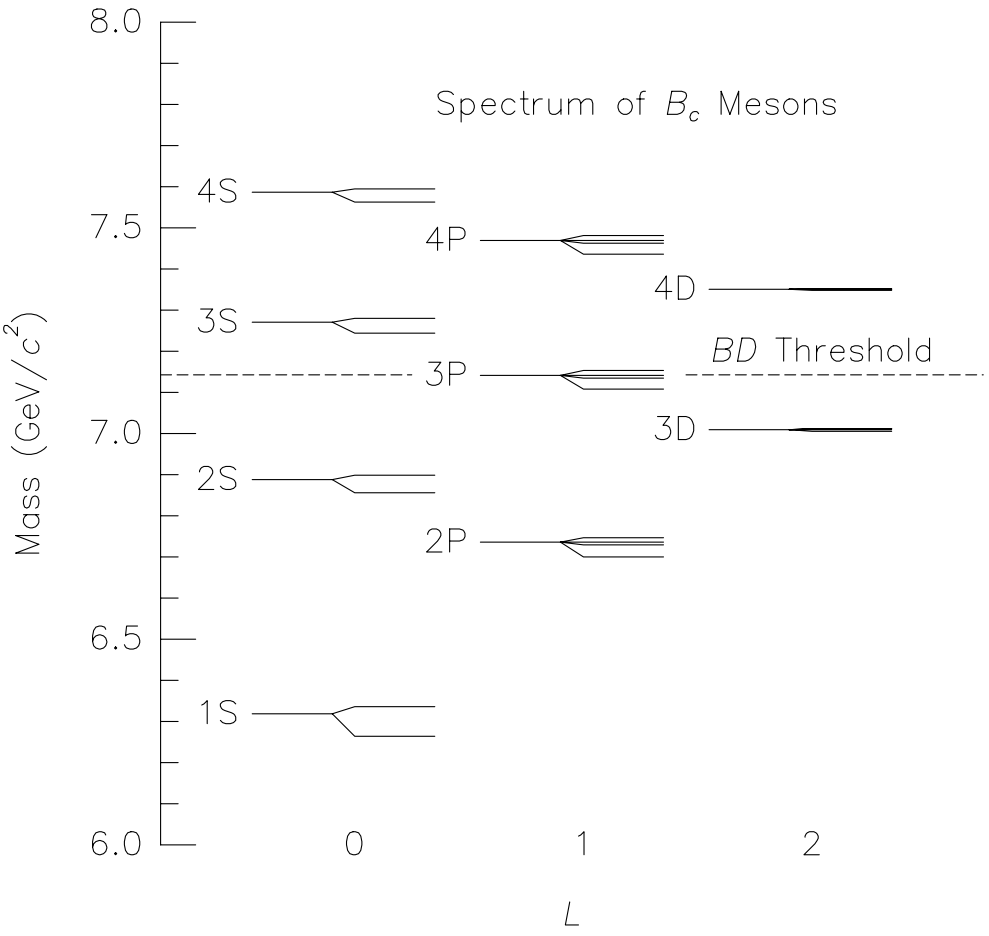

Figure 1.9: Predicted spectrum for the $\bar{b}c$ mesons in Ref [3]. The dashed line shows the threshold of the decay into $B - D$ pair

SUNG KYUN KWAN UNIVERSITY

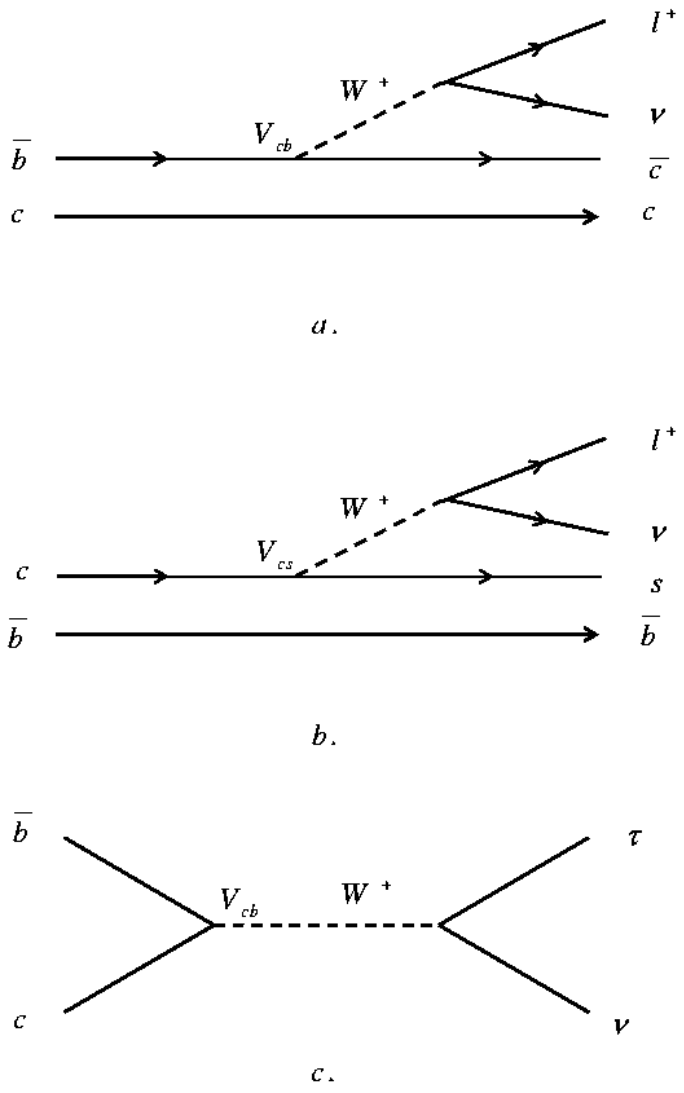

Figure 1.10: Feynmann diagrams for B_c decay: (a) The c-quark decay with the spectator $\bar{b}$-quark.($c \to X$), (b) The $\bar{b}$-quark decay with the spectator c-quark($\bar{b} \to X$), (c) The annihilation channel $B_c^+ \to l^+\nu_l(c\bar{s}, u\bar{s})$, , where $l = e,\ \mu,\ \tau$.

SUNGKYUNKWAN UNIVERSITY

Chapter 2

Experimental Apparatus

The Tavatron proton-antiproton Collider is the highest-energy particle collider currently operational anywhere in the world. The Collider Detector at Fermilab(CDF) is an azimuthally and forward-backword symmetric apparatus designed to study proton-antiproton collisions at the Tevatron.

During the period between 1997 and 2001 both the accelerator complex and CDF underwent major upgrade to increase instantaneous luminosity and take data sample of eventually 2 fb^{-1} of integrated luminosity or more. The upgraded accelerator has a shorter time between beam crossings than its predecessor: 396 ns in the current 36-bunch mode compared to 3.5 μs in the old 6-bunch mode. The new configuration required detector upgrades to ensure a maximum response time shorter than the time between beam crossings.

This chapter describe the accelerator and the detector components used to identify and measure properties of the particles produced during the $p\bar{p}$ collisions.

SUNG KYUN KWAN UNIVERSITY

2.1 Accelerator

The Tevatron is a superconducting particle accelerator and collider that is four miles in circumference. It accelerates protons and anti-protons up to 980 GeV and collides to produce elemental particles. A sketch of the accelerator complex at Fermilab is shown in Figure 2.1.

Generally a large number of $p\bar{p}$ collisions must occur to observe processes with small production cross section. The parameter that gives the rate of collisions is the luminosity, defined by the relation

$$N = \sigma \mathcal{L} \tag{2.1}$$

where N is the number of events produced per second for some final state, σ is the production cross section for that state and L is the luminosity in units of $cm^{-2}s^{-1}$.

At two points around the Tevatron ("B0" and "D0") the beams are focused by quadrupole magnets to achieve the highest luminosity possible within the detectors: CDF and DØ. The luminosity at the Tevatron can be expressed as:

$$\mathcal{L} = \frac{fBN_pN_{\bar{p}}}{2\pi(\sigma_p^2 + \sigma_{\bar{p}}^2)} \; F\left(\frac{\sigma_l}{\beta^*}\right) \tag{2.2}$$

where f is the revolution frequency at which proton or anti-proton travel around the Tevatron, which is about 70 kHz. B is the number of bunches, which is 36 now. $N_{p/\bar{p}}$ are the numbers of particles in proton and anti-proton bunches, typically about the order of 10^{11} and 10^{10} respectively. $\sigma_{p/\bar{p}}$ are the rms beam size at the interaction point. F is a form factor which depends on the ratio of σ_l, the bunch length, to β^*, the beta function at the interaction point. The beta function is a measure of the beam width, and is proportional to the beam's x and y extent in phase space. Anti-Proton availability is the most limiting factor for attaining high luminosities. The proton and anti-proton beams circulating in the Tevatron are unpolarized, and bunches exhibit a longitudinal density profile such that the resulting distribution of collisions

SUNGKYUNKWAN UNIVERSITY

along the beam axis is Gaussian, with a width of about 30 cm. Table 2.1 shows a comparison of Run I and Run II accelerator parameters.

The beam begins from a Cockcroft-Walton pre-accelerator [32] which accelerates H^- ions to 0.75 MeV. And the Linear accelerator (Linac) takes the H^- ions from 0.75 MeV kinetic energy to 400 MeV.

The Linac has two parts: 116 MeV drift-tube (Alvarez) linac operating at 201.25 MHz and a 400 MeV side-coupled cavity linac operating at 805 MHz [33]. Because of the Linac geometry, the accelerated ions become grouped into bunches.

Then they are injected into the Booster ring (a rapid cycling synchrotron with a diameter of 74.5 m) and two electrons are removed from the H^- ions by a thin carbon foil strips, leaving protons. Successive turns of ions are injected into the same orbit as the circulating protons. The protons are accelerated to 8 GeV in the booster before they are extracted into the Main Injector (MI), which operates at 53 MHz. This is accomplished by a series of electromagnetic kicks applied by RF cavities, about 500 kV per turn.

The Main Injector accepts these protons and continues the acceleration process, increasing their energy to 150 GeV. In addition, the Main Injector accelerates a portion of the protons to 120 GeV for use in anti-proton production. Then the 150 GeV protons from the Main Injector are delivered to the Tevatron in which the magnets have superconducting coils. The Main Injector, a new element of the Run II accelerator complex, is capable of larger proton currents than its predecessor, the Main Ring, enabling a higher rate of anti-proton production.

Anti-Protons are produced by extracting the proton beam from the Main Injector to hit a nickel target, creating a multi-particle spray that contains on average 20 anti-protons per million protons, with a mean kinetic energy of 8 GeV. The anti-protons are then focused by a lithium lens and separated from other particle species by a pulsed magnet.

Then the anti-protons produced in the target are accumulated in the $\bar{p}$ accumulator which actually has two rings. One is for debunching in which a

SUNGKYUNKWAN UNIVERSITY

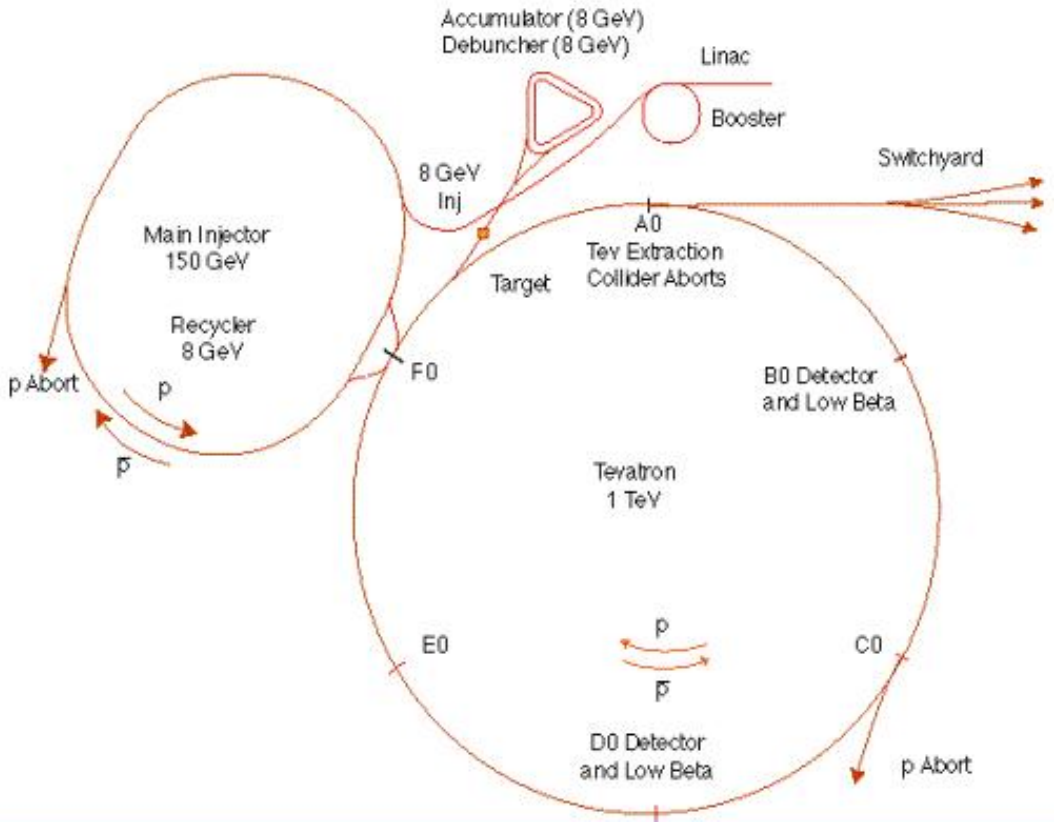

Figure 2.1: Fermilab accelerator complex.

SUNGKYUNKWAN UNIVERSITY

rotation in synchrotron phase space is done to reduce the energy spread at the cost of increasing the time spread of the $\bar{p}$ bunch. After debunching, the $\bar{p}$'s are added to the circulating beam in the accumulator where stochastic cooling takes place to reduce the random motions of the $\bar{p}$'s: horizontal, vertical and in synchrotron phase space [34]. When enough anti-protons are circulating in the accumulator ring, they are transferred back into the MI, and are accelerated.

Over a period of 10 to 20 hours, a stack of anti-protons is built up, in preparation for a new store in the Tevatron. At the start of a store, about once per day, 36 bunches of about 3×10^{11} protons and 36 bunches of roughly 3×10^{10} anti-protons are accelerated to 150 GeV by the Main Injector, transferred to the Tevatron – the final stage of Fermilab's accelerator chain. During most of the 2002–2003 run (Run II), the Tevatron was run with "36×36". This led to an interval between beam crossings of about 396 ns. The 132 ns mode (140×105) is currently under development. The beam collisions continue typically for 8 hours.

In the collider run, protons and anti-protons are injected into Tevatron from opposite directions and accelerated up to 980 GeV. Then they collide with each other. This yields the center-of-mass energy of 1.96 TeV.

SUNGKYUNKWAN UNIVERSITY

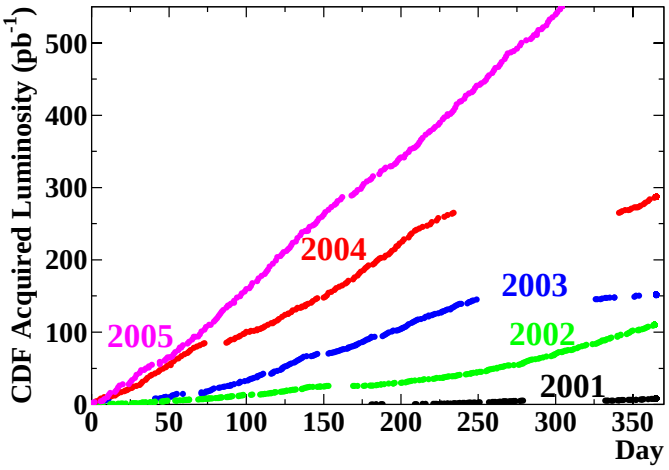

Figure 2.2: CDF acquired luminosity

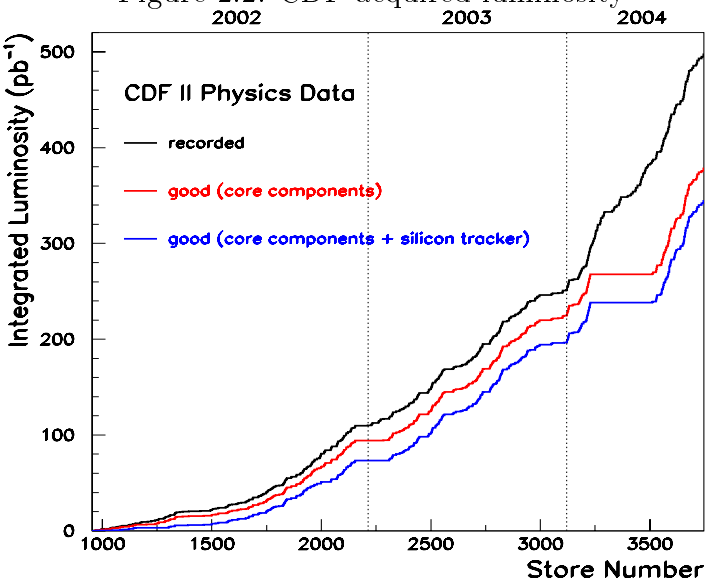

Figure 2.3: The summary of the integrated luminosity recorded at CDF so far, as functions of $p\bar{p}$ stores and time. The upper line shows all recorded, the middle line indicates that core components of CDF detector are good working, and the lower line when core components plus silicon tracker are good working.

SUNGKYUNKWAN UNIVERSITY

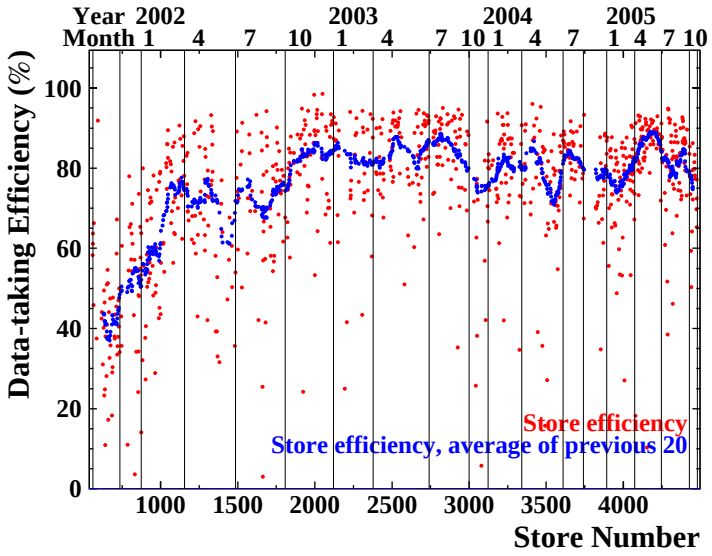

Figure 2.4: Data taking efficiency as functions of $p\bar{p}$ stores and time. It is a level of 80 to 90%. The inefficiency comes from trigger overflow, detector problem, high-voltage reconfiguration and so on.

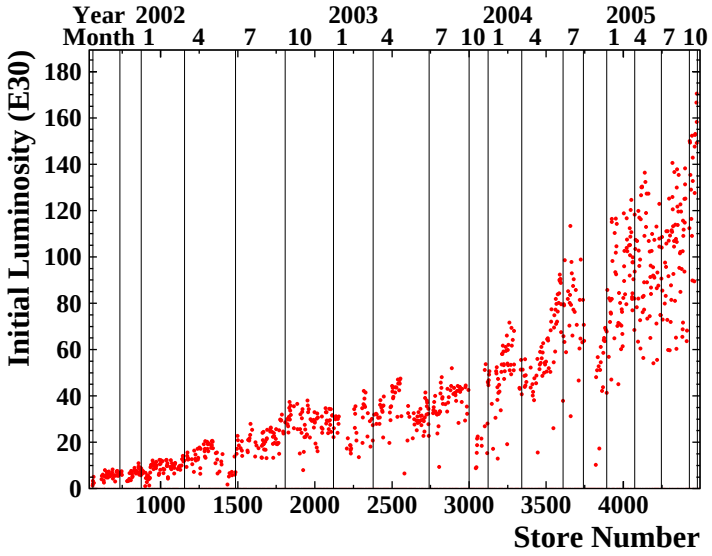

Figure 2.5: The initial instantaneous luminosity as functions of $p\bar{p}$ stores and time. The Tevatron has broken 10^{32} cm^{-2} s^{-1} barrier at June, 2004.

SUNGKYUNKWAN UNIVERSITY

Table 2.1: Parameters describing the accelerator configuration in Run I and II. The Run Ib column shows typical operating parameters during 6 × 6 bunches. The Run IIa column shows projections for 36 × 36 operation.

Run	**Ib**	**IIa**
protons/bunch	2.3×10^{11}	2.7×10^{11}
anti-proton/bunch	5.5×10^{10}	3.0×10^{10}
total anti-protons	3.3×10^{11}	1.1×10^{12}
proton emittance (mm-mrad)	23π	20π
anti-proton emittance (mm-mrad)	13π	15π
β^*	35	35
anti-proton bunches	6	36
bunch length (m)	0.6	0.37
bunch spacing (ns)	3500	396
interactions/crossing	2.5	2.3

2.2 Detector

The CDF detector is an azimuthally and forward-backward symmetric magnetic detector designed to study $p\bar{p}$ collisions at the Tevatron. It is an general purpose solenodial detector which combines percision charted particle tracking with fast projective calorimetry and fine grained muon detection. The major function of this detector is to measure the energy, momentum, and, where possible, the identity of the particles produced during the proton-antiproton collision.

Major differences for Run II include : the replacement of the central tracking system; the replacement of a gas sampling calorimeter in the plug-forward region with a scintillating tile calorimeter; preshower detectors; expansion of the muon coverage, a time-of-flight detector and upgrades of trigger, readout electronics, and data acqusition system.

An elevation view of the CDF Run II is shown in Figure 2.6. Tracking systems are contained in a superconducting solenoid, 1.5 m in raduis and 4.8 m in length, which generates a 1.4 T magnetic field parallel to the beam

SUNGKYUNKWAN UNIVERSITY

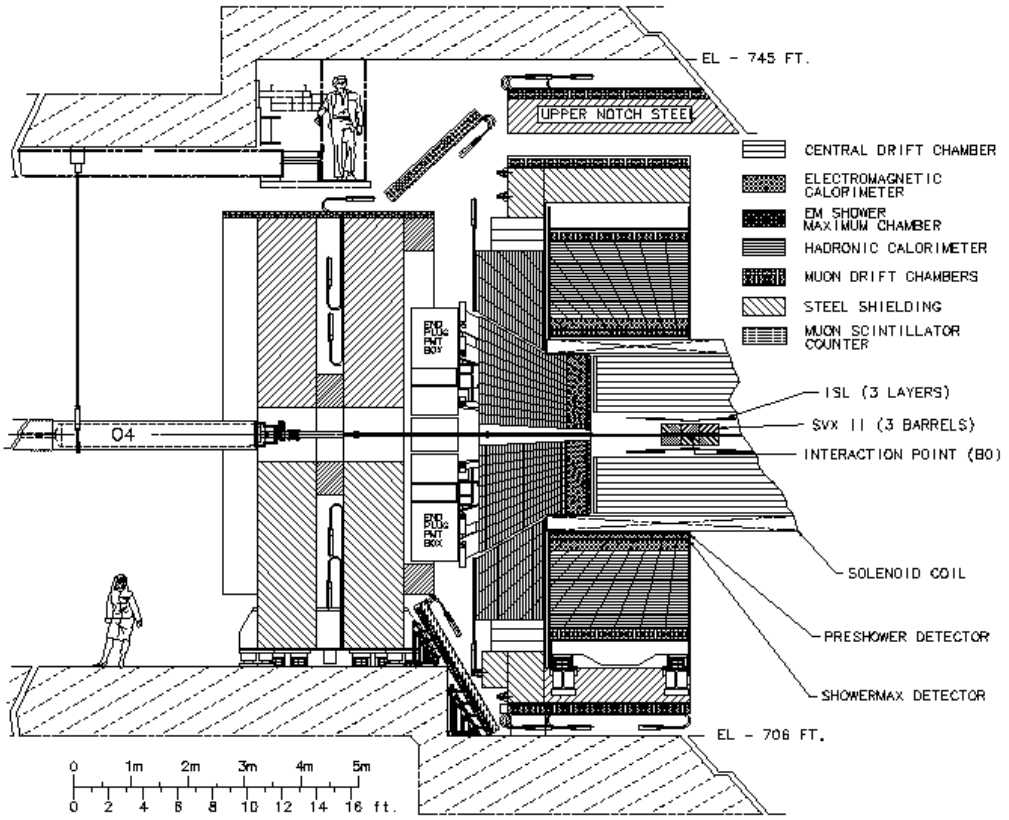

Figure 2.6: Elevation view of one half of the CDF II detector

axis. Calorimetry and muon systems are all outside the solenoid. The detailed description of the individual detector component can be found in various papers [46]. A schematic drawing of the major detector components is also shown in Figure 2.7.

2.2.1 Detector coordinate system

In the detector coordinate system commonly used at CDF, we choose z axis along the proton beam direction (East) with zero at the detector center, y axis upward and x axis towards outside of the Tevatron ring (North). Figure 2.8

SUNGKYUNKWAN UNIVERSITY

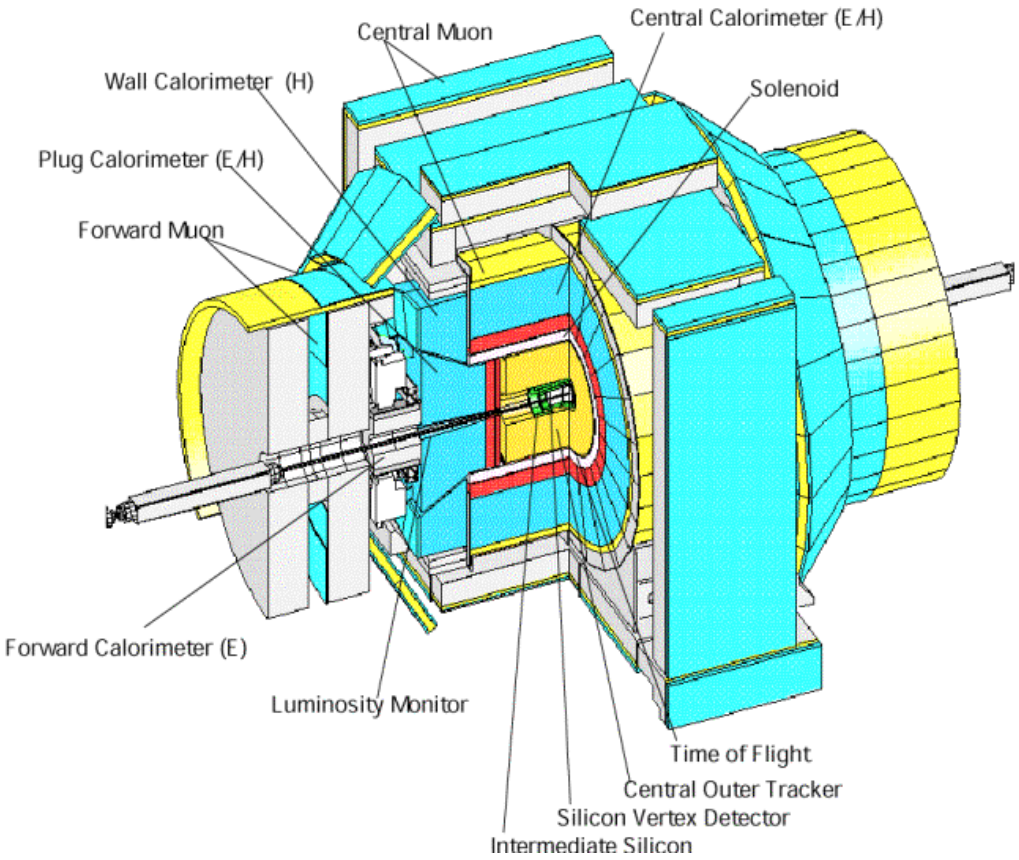

Figure 2.7: A schematic view of the CDF Run II Detector. The solenoid is located between the Central Outer Tracker and the Central Electromagnetic calorimeter. In the central region the existing solenoid and scintillator-based calorimeter were retained from Run I. On each "end" of CDF, the plug and forward ($|\eta| > 1$) calorimeters were replaced with one new end-plug calorimeter.

SUNGKYUNKWAN UNIVERSITY

shows the detector coordinate system. We use R as the distance to the beam line in cylindrical coordinates; ϕ is the azimuthal angle, and θ is the polar angle relative to the positive z-axis in spherical coordinates. Since hadrons are composite objects, daughter particles from a $p\bar{p}$ collision are often produced with significant momentum along the z axis. It is thus useful to define two variables, rapidity and pseudorapidity: The rapidity, which is defined as:

$$y = \frac{1}{2}\ln\left(\frac{\mathrm{E} + \mathrm{p_z}}{\mathrm{E} - \mathrm{p_z}}\right) \tag{2.3}$$

is often used instead of the polar angle θ in the laboratory coordinate frame. The advantage of rapidity is that a change of rapidity is a constant $\delta y = \theta \equiv \tanh^{-1}\beta$ under a boost in z direction with velocity $\beta \equiv v/c$. For the case where $E \gg m$, the rapidity can be approximated by pseudo-rapidity:

$$\eta = \frac{1}{2}\ln\left(\frac{\mathrm{E} + \mathrm{p_z}}{\mathrm{E} - \mathrm{p_z}}\right) = -\ln\left(\tan\frac{\theta}{2}\right) \tag{2.4}$$

The interaction point at CDF is not at the coordinate (0,0,0), however, it is assumed that the reconstructed default track at CDF is from (0,0,0). So the pseudorapidity calculated from default track is called detector pseudorapidity.

$|\eta|$ extends from 0 at the perpendicular to the beampipe to approximately 3.5 at the most forward part of the detector. The central portion of the detector spans $0.0 \lesssim |\eta| \lesssim 1.0$, while the forward (plug) detector is located at $1.0 \lesssim |\eta| \lesssim 3.0$. Sub-detectors are placed radially at varying distances from the collision point. Starting from the beampipe and expanding outward one finds the tracking system, calorimetry systems, and muon systems.

2.2.2 Cerenkov Luminosity Counter

At hadron collider experiments the beam luminosity, traditionally, has been measured using the process of inelastic $p\bar{p}$ scattering. It has a large cross-section, $\sigma_{in} \sim 60$ mb, measured at the Tevatron energy (1.96 TeV) by the CDF, with an uncertainty of $\sim 6\%$. The rate of inelastic $p\bar{p}$ interactions is given by [36]:

$$\mu \cdot f_{BC} = \sigma_{in} \cdot \mathcal{L} \tag{2.5}$$

SUNGKYUNKWAN UNIVERSITY

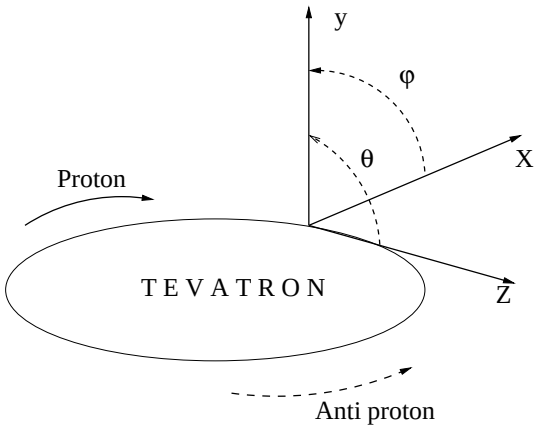

Figure 2.8: The CDF detector coordinate system

where $\mathcal{L}$ is the instantaneous luminosity, f_{BC} is the rate of bunch crossing in the Tevatron, μ is the average number of $p\bar{p}$ interactions per bunch crossing.

To detect inelastic $p\bar{p}$ events[1] efficiently a dedicated detector at small angles, operating at high rate and occupancy, is required. In Run II the Cerenkov Luminosity Counters (CLC) are being used by CDF to measure the Tevatron luminosity. The CLC is designed to measure μ accurately (within a few percent) all the way up to the high luminosity regime $\mathcal{L} \sim 2 \times 10^{32}$ cm^{-2} s^{-1} expected in Run II [46].

There are two CLC modules in the CDF detector, installed at small angles in the proton (East) and anti-proton (West) directions with rapidity coverage between 3.75 and 4.75. Each module consists of 48 thin, long, gas-filled, Cerenkov counters. The counters are arranged around the beam-pipe in three concentric layers, with 16 counters each, and pointing to the center of the interaction region [37]. The Cerenkov counters are not sensitive to beam halo[2], photons or neutrons, nor to soft charged particles which fall under the Cerenkov threshold.

[1] The CLC has zero acceptance for elastic $p\bar{p}$ events.

[2] See Reference [38] for a measure of beam halo and losses using the installed arrays of scintillation counters on both sides of the CDF detector.

SUNGKYUNKWAN UNIVERSITY

2.2.3 Tracking Systems

Detection and tracking of charged particles is the most essential part for B physics analysis. It determins the beam collision point and vertex points of the secondary particles. Generally trackers provide two fundamental kinds of measurement. On one side, they determine the direction and curvature of a particle's path; on the other, they delimit a narrow region where the particle might have been produced. The CDF II tracking system, shown in Figure 2.7, fulfills both kinds of requirements by combining different detector elements.

There are two primary tracking detector systems in the CDF Run II, inner tracking and outside tracking. The inner tracking system of a 90-cm long silicon micro-strip vertex detector, consisting of one single–sided layer and six double–sided layers, with an additional double-sided layer at large η, surrounds the beam pipe [39]. Outside the silicon detector, a 3.1 meter long drift chamber with 96 layers of sense wires, the Central Outer Tracker (COT), is used with the silicon detector to determine the momenta of charged particles and the z position of the $p\bar{p}$ interaction (z_{vertex}) [40].

Charged particle moving in a uniform magnetic field, as inside the CDF tracker, have a helicoidal trajectory. By measuring the radius of curvature of the helix, one obtains the particle's transverse momentum; the longitudinal momentum is related to the helix pitch. This information can be used in several ways: as a requirement in a trigger, during particle identification, in order to calibrate the calorimeters.

To obtain a precise measurement of the helix radius and pitch, it is necessary to sample points of the trajectory which are spread on a long lever arm. Therefore, a good spectrometer requires a large tracking volume. On the other hand, by taking a few, very accurate measurements of the track position near the primary interaction point, it is possible to narrow the region of space in which a given particle was originated. By intersecting such regions, it is possible to determine which (if any) particles were produced in a secondary vertex, trigger on their existence, and measure the mass and lifetime of short-lived particles.

SUNGKYUNKWAN UNIVERSITY

Helix parametrization

Within an axial and almost uniform magnetic field $\vec{B}$, such as the one inside the CDF solenoid, charged particles are subjected to the Lorentz force

$$\vec{F} = qe\vec{v} \times \vec{B} \tag{2.6}$$

and move along helices of radius

$$r = \left| \frac{p_T}{qeB} \right| \tag{2.7}$$

At CDF, such helices are described with the following parameters.

cot θ : cotangent of the ploar angle oat minimum approach

c : curvature of the helix(inverse of diameter), with the same sigin as the particle charge

z_0 : z coordinate at minimum approach

d : minimum distance between the helix and the detector axis, impact parameter

ϕ_0 : azimuthal direction of the track at minimum approach

Figure 2.9 shows the detail of each parameter.

The term "minimum approach" refers to the point of the helix which lies cloest to the detector axis, in the proximity of the origin.

The purpose of the tracking system is to find tracks, and to associate to each track the best estimate of its parameters c,d,ϕ_0,z_0 and cotθ.

Central Outer Tracker

The Central Outer Tracker(COT) is an open-cell drift chamber, which fills the volume between radial coordinates of 40 and 138 cm, up to a $|z|$ of 155 cm.

SUNGKYUNKWAN UNIVERSITY

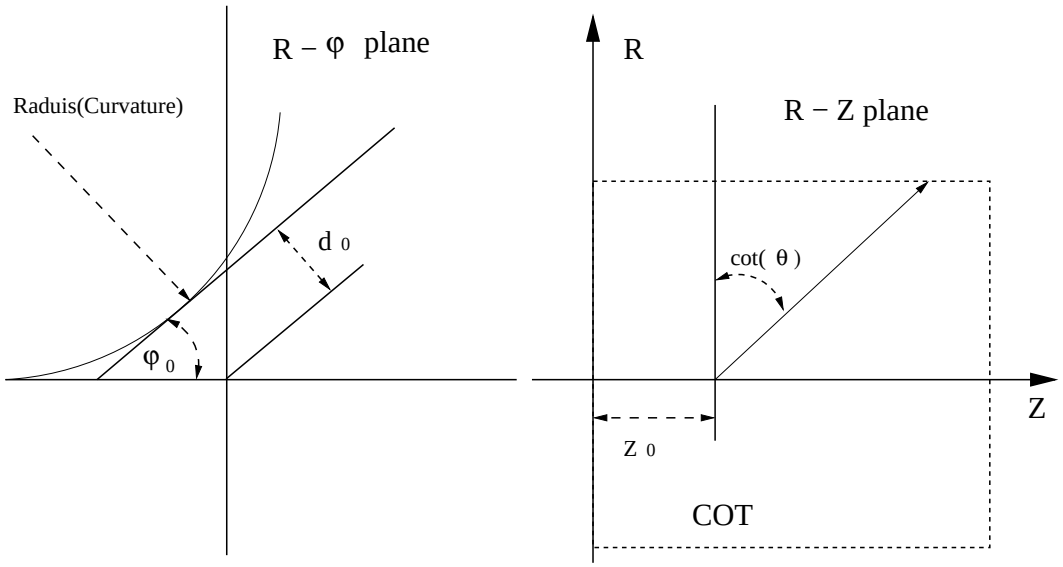

Figure 2.9: The schematic trajectory of a charged particle. It shows the helix parameters to describe track trajectory mathematically.

with its long lever arm, it provides an accurate measurement of track curvature, ϕ_0 and $\cot\theta$. The COT surrounds the silicon detector and mextends to a radius just inside of the Time-of-Flight system. The inner and outer walls of the COT cylinder are made of 0.25 *in* aluminum sheet with the inner radius at 0.4 m. The tracking volume is dividedin eight superlaysers(SL), each containing twelve layers of sense wires. Axial superlaysers, in which wires are paralled to the magnetic field, alternate with superlaysers in which the wires have a 3° stereo angle. Each superlavyer is divided in identical cell and cells are delimited by two field panels, made of gold-coated Mylar, and two shaper panels, which are Mylar with with two field-shaping panels attached. A cell contains twenty five gold-plated copper-beryllium wires with 51μm. They alternate between potential and sense wires. The wire spacing is about 7.5 mm in all SL. COT contains total 30,240 sense wires that run the length(in z) of the chamber between two end plates. Each wire is strung between the two endplates with a tention of 1.3 N, giving a total load on the endplates of 40 tons from all of the wires. At the center of COT,a mylar wire support is epoxied to all of the sense and potential wires to provide additional electrostatic stability.

SUNGKYUNKWAN UNIVERSITY

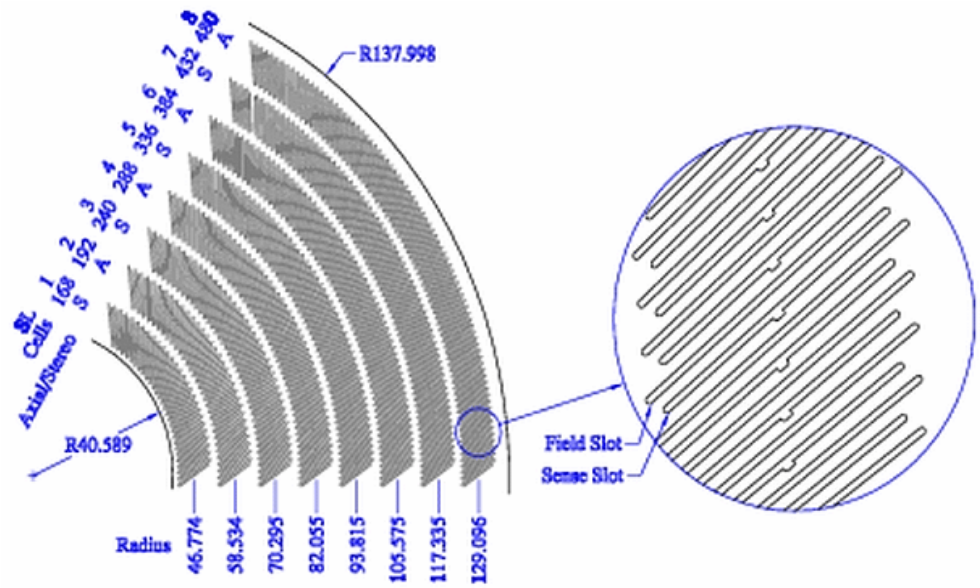

Figure 2.10: Schematic view of COT endplate. Slots for field plates and wire planes alternate.

The spacing between wires and the field sheets is just under 1 cm and varies slightly between SL. In an axial layer,the wires and fieldplanes are parallel to the z axis, and thus provide only $r - \phi$ information. In stereo layers, a given wireplane or field sheet which starts at a slot in one endplate is offset by 6 cells. This generates a stereo angle of 3° which gives z axis information.

The design of three cells from SL2 is shown in Figure 2.102.11 and Table 2.2 summarize the COT geometry. Ar-Ethane gas(60 : 40 mixture) fills the active chamber volume and both provides a source of ionized electrons and defines the drift velocity. When a charged particle passes through , the mixed gas is inonized and produce electrons. The electrons drift towards the same sense wires, resulting in an avalanche at the wire surface, which provides a gain of $\sim 10^4$. The charge of ionized electrons is used in the measurement of dE/dX, for particle identification. Due to the magnetic field, the electrons drift with a Lorentz angle of $\sim 35°$. It is the reason that the cells are tilted with respect to the radial direction with the same Lorentz angle.

The voltage on the wire plane is set in order to insure a maximum drift

SUNGKYUNKWAN UNIVERSITY

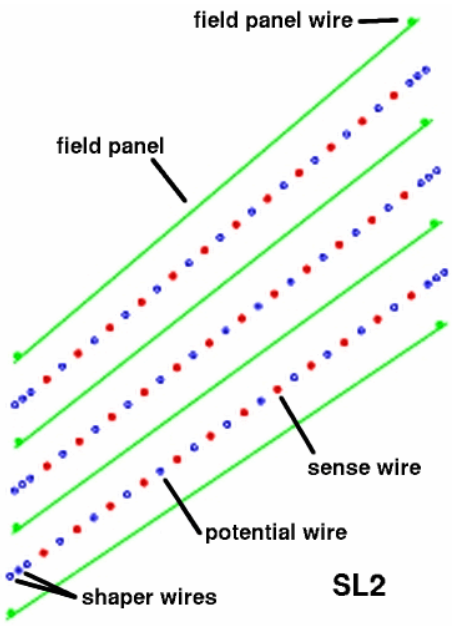

Figure 2.11: Nomial cell layout for SL2. Other superlaysers are similar.

time, about 100 ns which is less than the time between beam crossing time which is currently 396 ns. The drift time resolution is better than 2 ns giving a single hit resolution of 150 μm. This hit resolution combined with the large lever arm, give the COT a momentum resolution of

$$\frac{\sigma_{pT}}{p_T^2} = 0.15\% \;\; GeV/c \tag{2.8}$$

Silicon Tracking System

The CDF Run II silicon tracking system privides a decay position and a trajectory for charged particles with an extremely high precision. It has proven to be an excellent tool for top search and for b physics since the CDF Run I experiment. The primary goal of the silicon tracking system is to reconstruct tracks for use in the pattern recognition of displaced secondary vertices from the beam collision position. Thease secondary vertices are created from the decay of long lived particles and provide a very good background rejection

SUNGKYUNKWAN UNIVERSITY

Superlayer	Average r	Stereo angle	♯ cells	♯ sense wires
1	46 cm	$+3°$	168	2016
2	59 cm	0	192	2304
3	70 cm	$-3°$	240	2880
4	82 cm	0	288	3456
5	94 cm	$+3°$	336	4032
6	106 cm	0	384	4068
7	119 cm	$-3°$	432	5184
8	131 cm	0	480	5760
Axial total			1344	16128
Stereo total			1176	14112
Overal			2520	30240

Table 2.2: Central Outer Tracker geometry

power in the identification of charm and beauty hadrons.

Silicon tracking system consists of eight layers of microstrip silicon detector on waper, placed in a range between 1.135 and 30 cm from the beam axis. It provides accurate, three-dimensional vertexing measurements by measuring the d and z_0 parameters of charged tracks and also extends the tracking coverage of CDF from the COT limit($|\eta| < 1$) to $|\eta| < 2$. The tracker is divided, in three conecntric subsystems : Layer00, SVXII and ISL(intermediate silicon layers).

Microstrip silicon detectors are based on inversely polarized $p-n$ junctions. If a charged particle crosses the detector, electron-hole pairs are released by ionization, and drift towards the surface. By segmenting the surface into p^+ (or n^+) strips, which are capacitively coupled to conductive strips, the position of the ionizing particle can be measured along an axis orthogonal to the segments.

All of the ISL wafers and two of those in SVXII are double-sided, with axial strips on the p side and small-angle stereo (SAS) strips on the n side, which form an angle of $\pm 1.2°$ with the detector axis. Three layers of SVXII consist of double-sided wafer whose n-strip from an angle of $90°$ with the axial direction. Orthogonal strips privide a very accurate measurement of

SUNGKYUNKWAN UNIVERSITY

Table 2.3: Silicon tracker geometry. L00 wafers have different widths in ϕ wedges A and B. ISL geometry is reported for the central(c) region ($|\eta| < 1$), where layer 7 is absent, and forward(f) region. Radii are measured at the center of the wafer.

	Layer	Active width (cm)	Wedge A radius (cm)	Wedge B radius (cm)	Type
Layer00	0	0.64(A) 1.28(B)	1.35	1.62	Axial only
SVX II	1	1.536	2.995	2.545	90°
	2	2.3038	4.57	4.12	90°
	3	3.84	7.02	6.52	Stereo -
	4	4.608	8.72	8.22	90°
	5	5.824	10.645	10.095	Stereo +
ISL	6c	2×5.73	23.1	22.6	Stereo -
	6f	2×5.73	20.2	19.7	Stereo -
	7f	2×5.73	29	28.6	Stereo +

z coordinate. By using both SAS and 90° wafers 3D vertexing resolution is improved dramatically. Lastly, L00, being placed extremely close to the interaction point, is built of radiation-hard, single-sided microstrip wafers.

Silicon wafers in L00 and SVXII are arranged on twelve azimuthal wedges. In the region $1 < |\eta| < 2$, the inner layer of ISL is divided in 24 wedges, while the outer layer forms 36 wedges; 28 wedges forms a single ISL layers in the central region($|\eta| < 1$). Without ISL and L00, SVX II reaches a impact parameter resolution of $\sim 40\mu$m which includes the $25 - 30\mu$m contribution from the transverse size of the beamline. Table 2.3 shows the summary of the CDF Run II silicon tracker geometry.

Track reconstruction

Track reconstruction begins in the outer tracking chamber - the COT. The first step in track reconstruction is to form line segment from hits in each superlayer in the COT. Line segment from the axial layers which are consistent

SUNGKYUNKWAN UNIVERSITY

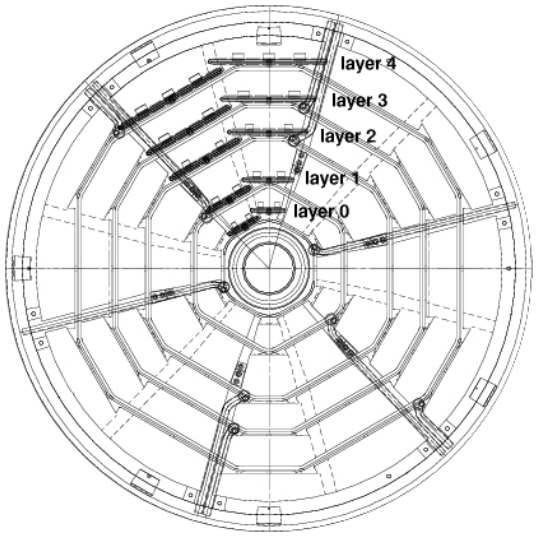

Figure 2.12: SVX bulkhead, end view. it shows two wedges installed.

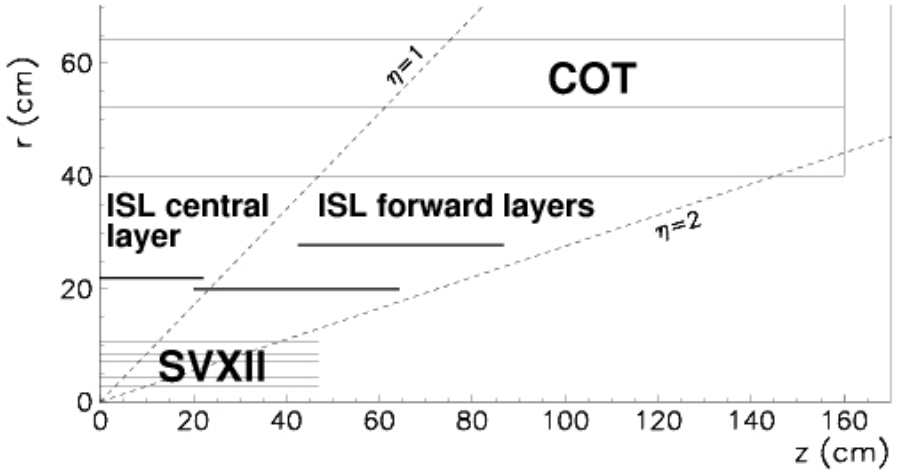

Figure 2.13: Schematic view of CDF tracking system. η coverage of each tracking system is shown.

SUNG KYUN KWAN UNIVERSITY

with lying tangent to a common circle are linked together to form a track. A two dimentional track fit is performed on $R-\phi$ plane. Line segment in stereo layers are then linked to the 2D track, then finally a helix fit is performed.

The next step is to extrapolate the track reconstructed in COT into the silicon tracking system. It starts in the outermost layer of the silicon tracker. A road, or window around the track is established based on the errors on the COT track parameters. If hits lie within the road, thay are added to the track. A new track fit is then performed, resulting in a new error matrix and a new road. This road is then used to add hits from the next silicon layer. This procedure is repeated until there are no layers left. There may be multiple tracks with different combinations of silicon hit associated with one COT track. In this case, the track with the largest number of silicon hits is chosen.

2.2.4 Time-of-Flight Systems

Right outside of tracking systems, there is the Time-Of-Flight (TOF) detector which measures the flight time of particles. The TOF detector newly has been added to the CDF II detector to enhance the particle identification [43]. it is very useful for particle identification in low momentum region. Figure 2.14 shows the separation power as a function of momentum for each particles.

Tmhe time-of-flight of the particle is defined to be difference between the arrival time at the TOF scintillator and the collision time t_0. Similary, the path length L of the particle is calculated in between the scintillator and the beam collision point. Using this information and the momemtum of the particle, the mass of the particle is given in formula below,

$$m = \frac{p}{c}\sqrt{\left(\frac{ct}{L}\right)^2 - 1} \tag{2.9}$$

Figure 2.15 shows the charged particle mass calculated given formula with TOF information.

The primary goal is to provide a 2σ separation between $\pi^{\pm}$ and $K^{\pm}$ for

SUNGKYUNKWAN UNIVERSITY

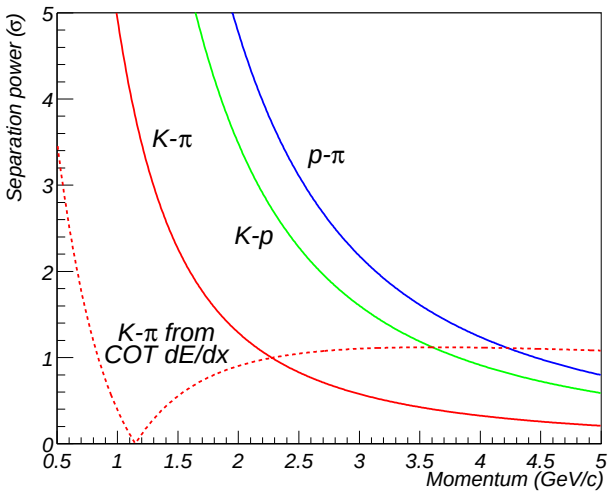

Figure 2.14: The separation power as a function of momemtum between K/π, p/π, and K/p traversing a distance of 140 cm, expressed in separation power aassuming a resolution of 100 ps. The dashed line shows the K/π separation power from the dE/dX measurement in the COT.

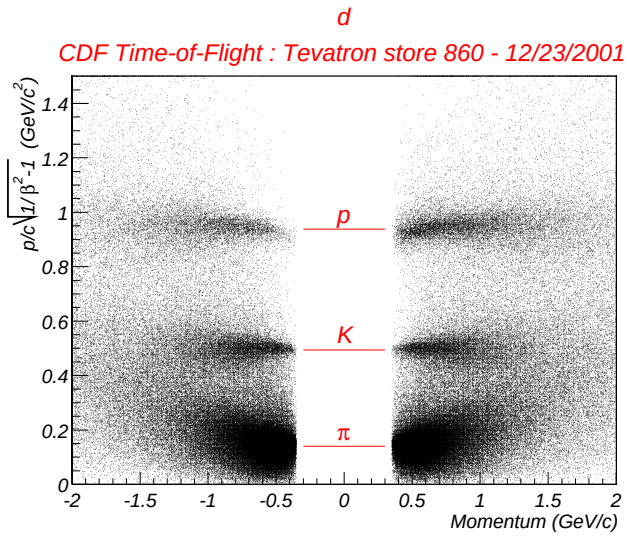

Figure 2.15: The TOF performance plot. the mass of charged particles are calculated with TOF information. Positively charge tracks are on the right, negative tracks are on the left.

SUNGKYUNKWAN UNIVERSITY

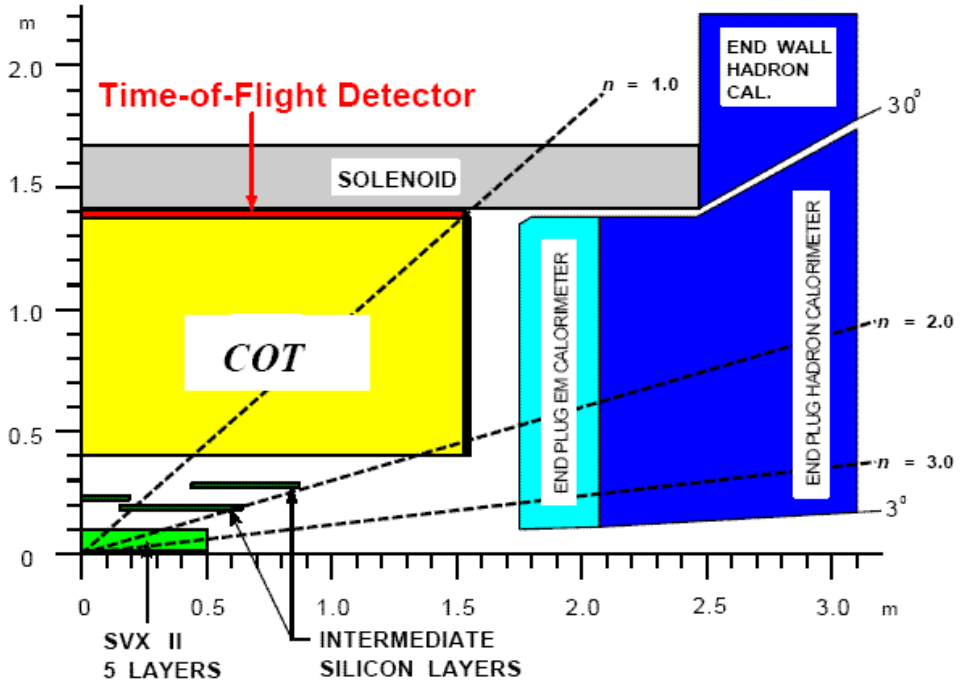

Figure 2.16: Side view of the central region of the CDF II detector (quarter section), showing the Tracking System which is cylindrically symmetric. Layer 00 is missing from the illustration.

momentum $p < 1.6$ GeV/c^2. By combining it with dE/dx it is expected to improve the neutral B meson flavor determination. Another purpose of TOF detector is to search for highly ionizing particle-monopole [44]. Since the mass difference between pion and proton is even bigger than the difference between pion and Kaon, the particle identification ability of selecting proton from pion by combining TOF and dE/dx together is very powerful in b physics.

2.2.5 Superconducting Solenoid Magnet Coil

The superconducting solenoid magnet coil is made of an aluminum-stabilized NbTi/Cu superconductor. It provides a uniform 1.41 T magnetic field along the incident beam direction in the COT region.

The CDF calorimeter systems are located outside the solenoid with two

SUNGKYUNKWAN UNIVERSITY

separated devices of the electromagnetic (EM) and hadronic (HA) calorimeters where hadron, electron, photon deposit most of their energy. This is useful to identify electrons and photons. Unlike hadrons and electrons, muons only deposit minimum ionization energy in the calorimeters, so muon system outside the calorimeter is used to identify muon. In addition, there are the Central Pre-Radiator (CPR) and Central Electromagnetic Strip (CES) chambers. Both CPR and CES are used to discriminate between a signal photon and background from a neutral pion decay to $\gamma\gamma$.

2.2.6 Calorimeters

Calorimetry has played a crucial role in the physics CDF has produced: the top mass discovery, the precision measurement of the W mass, photon and jet measurements over many orders of magnitude, and searches for new phenomena have all exploited the excellent behavior of the calorimeters. In the upgraded detector the existing scintillator-based calorimeter was retained within central region, but its electronics needed to be replaced due to the shorter bunch spacing. On each "end" of CDF, the plug and forward ($|\eta| > 1$) calorimeters were replaced with one new end-plug calorimeter. The system promises an exceptional increase in compactness, hermiticity, radiation hardness, and speed over the present system.

The solenoid and tracking volumes of CDF are surrounded by calorimeters, which cover 2π in azimuth and $|\eta| \leq 3.6$. The central electromagnetic (CEM) calorimeter covers $|\eta| \leq 1.1$ and is followed at a larger radius by the central hadronic calorimeters (CHA and WHA), which cover $|\eta| \leq 1.3$. These calorimeter use scintillator as the active medium. The CEM absorber is lead and the CHA/WHA absorber is iron. The calorimeters are segmented into units of 15 degrees in azimuth and 0.1 pseudorapidity. Two phototubes bracket each tower in ϕ, the average of the energy in the two tubes is used to determine the ϕ position of energy deposited in a tower.

The calorimeter is made up of wedges, or "physical towers", measured in $\eta - \phi$ coordinates. Each tower uses a series of absorber and scintillator layers.

SUNGKYUNKWAN UNIVERSITY

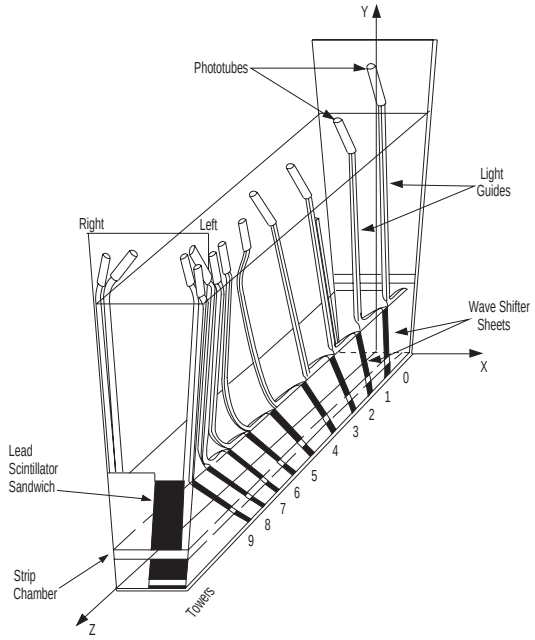

Figure 2.17: Schematic view of the wedge module of the central electromagnetic calorimeter.

Scintillator light is collected by a light pipe and a wavelength shifter that directs the energy into a photomultiplier tube (PMT). An $r-z$ view of the detector shows the calorimeter wedges arranged as if a ϕ cut into slices, with each slice pointing back toward the interaction point. The central portion of the calorimeter has towers that span 15° in ϕ and 0.11 in units of η, while plug calorimeter towers span either 15° or 7.5° in ϕ, and varying ranges in η.

The CEM uses a hybrid design. It consists of the lead and scintillator layers with an embedded strip chamber approximately at the depth of maximum particle multiplicity for electromagnetic showers. The scintillator provides a good energy resolution and the strip chamber provides the position determination and transverse development at the shower maximum. The average energy resolution of the CEM is

$$\frac{\sigma(E)}{E} = \frac{13.5\%}{\sqrt{E_T}} \oplus 2\% \text{ (added in quadrature)}, \tag{2.10}$$

where $E_T = E \cdot \sin\theta$ (E in GeV).

SUNGKYUNKWAN UNIVERSITY

The CHA and WHA are made of steel and scintillator. The interaction length of both the CHA and WHA is 4.5 λ_0. The CHA has 32 layers with 2.5 cm sampling, and the WHA has 15 layers with 5.0 cm sampling. For hadrons, the single-particle resolution depends on angle and varies from roughly $50\%/\sqrt{E}$ plus 3% added in quadrature in the CHA to $75\%/\sqrt{E}$ plus 4% added in quadrature in the WHA.

For Run II, there is new plug calorimeter, with variable tower size, which extends coverage out to $|\eta| = 3.6$. The plug electromagnetic calorimeter (PEM) covers both ends of the superconducting magnet coil. Each of them are made of four quadrants of $\delta\phi = 90°$. And each of the quadrants consists of 34 layers of proportional tube arrays interleaved with 2.7 mm thick lead absorber panel filling about 50 cm in depth. The plug hadronic calorimeter (PHA) has 20 layers of steel and proportional tubes. Each energy resolution of PEM and PHA is about 16% and 80%. The PEM contains an embedded position detector at shower maximum to improve electron identification and π^0/γ separation. In addition, the first layer of the PEM may be read out separately as a pre-shower detector.

2.2.7 The CPR and CES chambers

The central calorimeter is segmented into 48 independent wedge modules. The full central detector is constructed of two rings of 24 wedges each that make contact at $z = 0$. Each wedge subtends 15° in azimuth and approximately one unit in η. Both CPR and CES chambers are segmented into two halves in CDF z coordinates.

A system of proportional wire chambers in front of the central electromagnetic calorimeters (the CPR system) uses the one-radiation-length-thick magnet coil as a 'preradiator' to determine whether showers start before the calorimeter [45]. Wire chambers with cathode strip readout (the CES system), located at shower maximum in the central electromagnetic calorimeter, give 2-dimensional profiles of showers.

The CPR chambers' perpendicular distance to beam line is 168 cm. Inside

SUNGKYUNKWAN UNIVERSITY

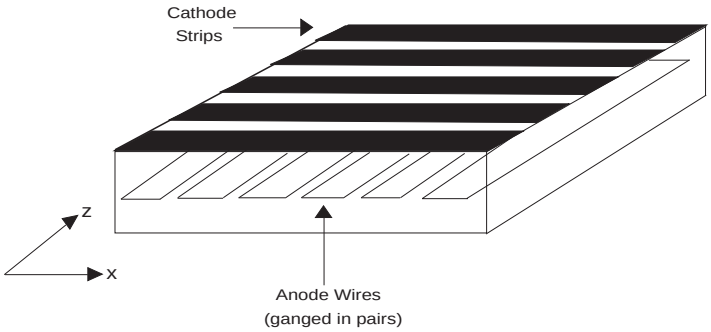

Figure 2.18: Schematic view of CES.

each CPR chamber the wires running along z directions are split about the middle of z. They are 16 wires at low $|z|$ (7.9 $\sim$ 119.7 cm), and 16 at high $|z|$ (123.5 $\sim$ 235.3 cm) for a total of 32 in one wedge.

The CES chambers' perpendicular distance to beam line is 184 cm. The CES anode wires measure ϕ and cathode strips measure η. Inside each chamber the wires running along z directions are split in the middle in z (121.2 cm). They are 32 wires at low $|z|$ (0.2 $\sim$ 121.2 cm), and 32 at high $|z|$ (121.2 $\sim$ 239.6 cm) for a total of 64 in one wedge. The strips are slightly different pitch in low and high $|z|$. There are the 69 z strips at low $|z|$ and 59 at high.

2.2.8 Muon Chambers

The muon detectors are located outside of the calorimeter, at the furthest reaches of the detector. Muons are minimum ionizing particles, which means they are capable of travelling through many interaction lengths before losing their energy and stopping.

CDF uses the steel in the calorimeter, the magnet return yoke, and additional steel shielding to stop all other charged particles from entering the muon detectors. The muon chambers record hits from the path of the muon through the detector. This information, combined with tracks in the COT, results in an excellent muon identification, as well as, rejection of cosmic background.

SUNGKYUNKWAN UNIVERSITY

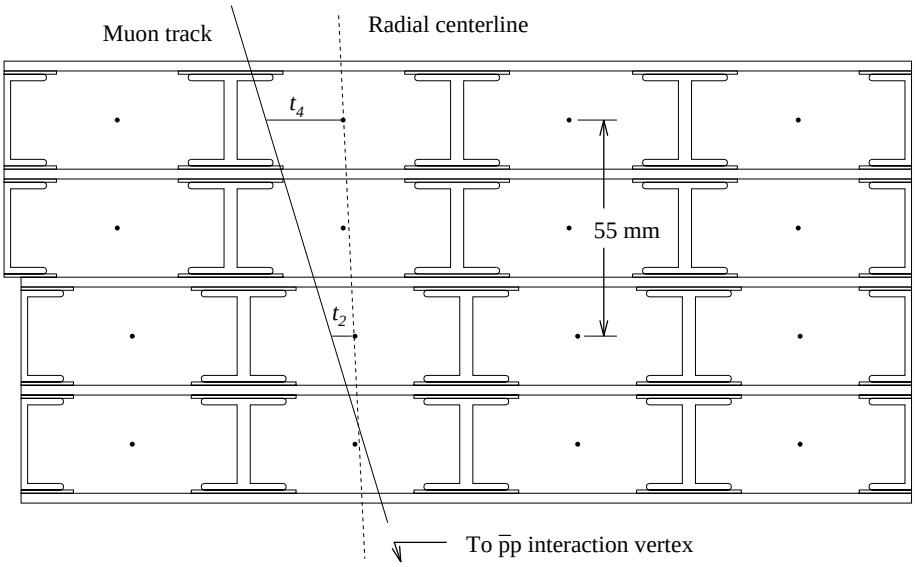

Figure 2.19: Cross section of a CMU module. Each module contains 4 layers of 4 rectangular drift cells.

The muon detectors are four systems of scintillators and proportional wire chambers which extend out to $|\eta| \leq 1.5$. They are, moving outward from the interaction point: central muon (CMU), central muon upgrade (CMP), central muon extensions (CMX/CSX), and barrel muon detector (BMU)detectors. The BMU is newly installed for CDF Run II experiment.

CMU

The CMU is located around the outside of the central hadron calorimeter at a radial distance of 3470 mm from the beam axis. It covers $|\eta|$<0.6 region. The muon detector is segmented in ϕ into 12.6° wedges which fit into the top of each central calorimeter wedge. This leaves a gap in the central muon coverage of 2.4° between each wedge. The three modules are bolted together at each end to from a single unit. This single unit is suspended from the top of the calorimeter wedge. Figure 2.19 shows the location of the central muon chamber. Each of the three modules in a wedge consists of four layers of four rectangular drift cell.

SUNGKYUNKWAN UNIVERSITY

CMP

The CMP covers $|\eta|<0.6$. It provides confirmation for tracks from CMU but with reduced non-muon (hadronic) background. It consists of 4 layers of single-wire drift cells installed outside of 2 feet of additional steel to reduce the non-muon background. The drift cells are rectangular with cross-sectional dimensions of 2.5 cm $\times$ 15 cm.

CMX

The CMX is an extention to the central muon detector to cover $0.6<|\eta|<1.0$. It consists of a conical arrangement of drift tubes and scintillation counters, which are used to reject background based on timing information. The drift cell differ from those of the CMP only in length. They are arranged in azimuthal sections with 15° azimuthal angle. Each wedge has 8 layers of rectangular tubes in radial direction and 6 cells neighbor in each other in ϕ .The 8 layers are grouped in pairs to form 4 continuous layers, each of which is half-staggered with respect to each other.

BMU

The barrel muon detector is newly installed for the CDF Run II. It covers $1.0<|\eta|<1.5$. Three-quarters of the azimuth is instrumented. The chambers are 11.9 feet long, 1 inch deep, and 3.3 inches wide, with each chamber covering 1.25° in azimuth. The chambers are stacked four high radially, with the second and fourth stacks staggered azimuthally by a half-cell relative to the first and third.

The rapidity coverage of the muon detectors are summarized as following:

- The CMU and CMP extend out to $|\eta|$ of 0.6.
- The CMX spans a range of $0.6<|\eta|<1.0$.
- The BMU finalizes the coverage from $1.0<|\eta|<1.5$.

SUNGKYUNKWAN UNIVERSITY

These are also shown in Figure 2.20 also.

2.3 Trigger and data acquisition systems

The trigger system is the important component for detector at hadron collider. It is impossible to record all events produced during the $p\bar{p}$ collisions. A typical event size is 250 kB. At the 2.5 MHz beam crossing rate, the system would have to be capable of recording 625 GB/s. This is assuming that there is an interaction every beam crossing, which is not unreasonable, described as an average of 2.3 interactions per crossing in Table 2.1.

We are interested in events containing particles with large transverse energy. This reflects hard scattering of quarks in the protons and anti-protons. The uninteresting inelastic events, called "minimum bias", occur ten orders of magnitude more frequently than $t\bar{t}$ events, and four order of magnitude more often than events with b's. Currently, the maximum event rate to disk is $\approx$ 70 Hz. If events were selected randomly, we would have no chance of acquiring interesting data samples large enough to make precise measurements or to approach new physics.

The complex system of digital electronics called the trigger allows the experiment to decide, in a very short amount of time, whether an event is interesting enough to record or not. It is of the utmost importance that the decision is fast, so that collisions are not missed while the trigger is thinking about its decision.

There are three trigger paths at CDF trigger system so that a data acquisition system (DAQ) efficiently consumes the collision events within a 132 ns bunch-crossing rate. [3] Since all the events cannot be stored, only the interesting events are selected by triggers. In each trigger step, the data size is reduced according to that triggering ability: 40 kHz acceptable rate at Level-1, 300 Hz for Level-2, and 30-50 Hz at Level-3 trigger stage.

[3] In the period of data taking considered in this analysis, the accelerator was operating in 35 bunches mode (beam crossing interval of 396 ns) and the trigger was clocked every 132 ns with the two intermediate clock cycles automatically rejected.

SUNGKYUNKWAN UNIVERSITY

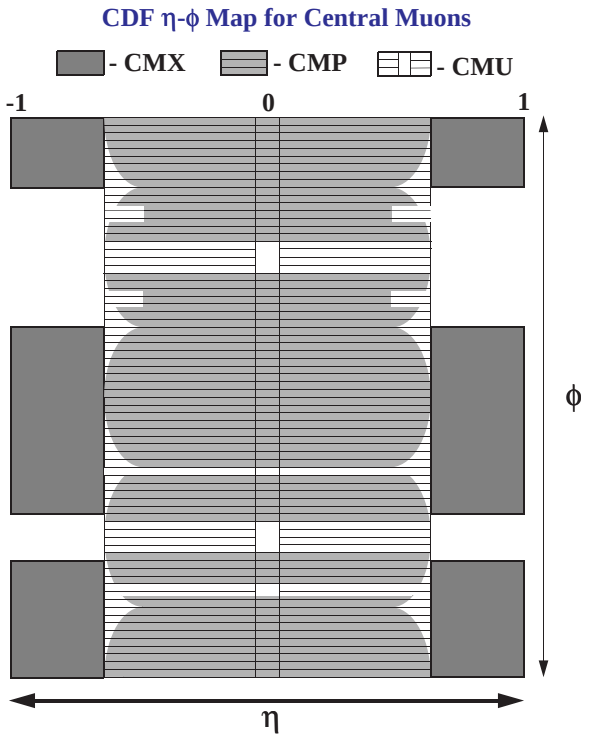

Figure 2.20: The coverage of muon system. CMU, CMP and CMX coverage are hatched.

SUNGKYUNKWAN UNIVERSITY

Figure 2.21 shows the functional block diagram of the readout electronics. To accommodate a 132 ns bunch-crossing time and a 4 μs decision time for the first trigger level, all front-end electronics are fully pipelined, with on-board buffering for 42 beam crossings. Data from the calorimeters, the central tracking chamber, and the muon detectors are sent to the Level-1 trigger system, which determines whether a $p\bar{p}$ collision is sufficiently interesting to hold the data for the Level-2 trigger hardware. See Figure 2.22 for details. The Level-1 trigger is a synchronous system with a decision reaching each front-end card at the end of 42-crossing pipeline. Upon a Level-1 trigger accept, the data on each front-end card are transferred to one of four local Level-2 buffers. The second trigger level is an asynchronous system with an average decision time of 20 μs. A Level-2 trigger accept flags an event for readout. Data are collected in DAQ buffers and then transferred via a network switch to a Level-3 CPU node, where the complete event is assembled, analysed, and, if accepted, written out to permanent storage. These events can also be viewed by online monitoring programs running on other workstations.

All events accepted by Level-2 trigger are collected in the Event Builder (EVB), and then the EVB assembles those event fragments into one data block and delivers it to the Level-3 trigger system. The Level-3 trigger system is a farm of parallel processors which operate on a Linux PC, where a full event reconstruction is implemented in software. After passing through the Level-3 trigger, the Data Logger system delivers events to the tape device or online monitoring processes. The Level-3 reconstruction program is written in C++ with object-oriented techniques. The same reconstruction program is used in the offline event analysis.

SUNGKYUNKWAN UNIVERSITY

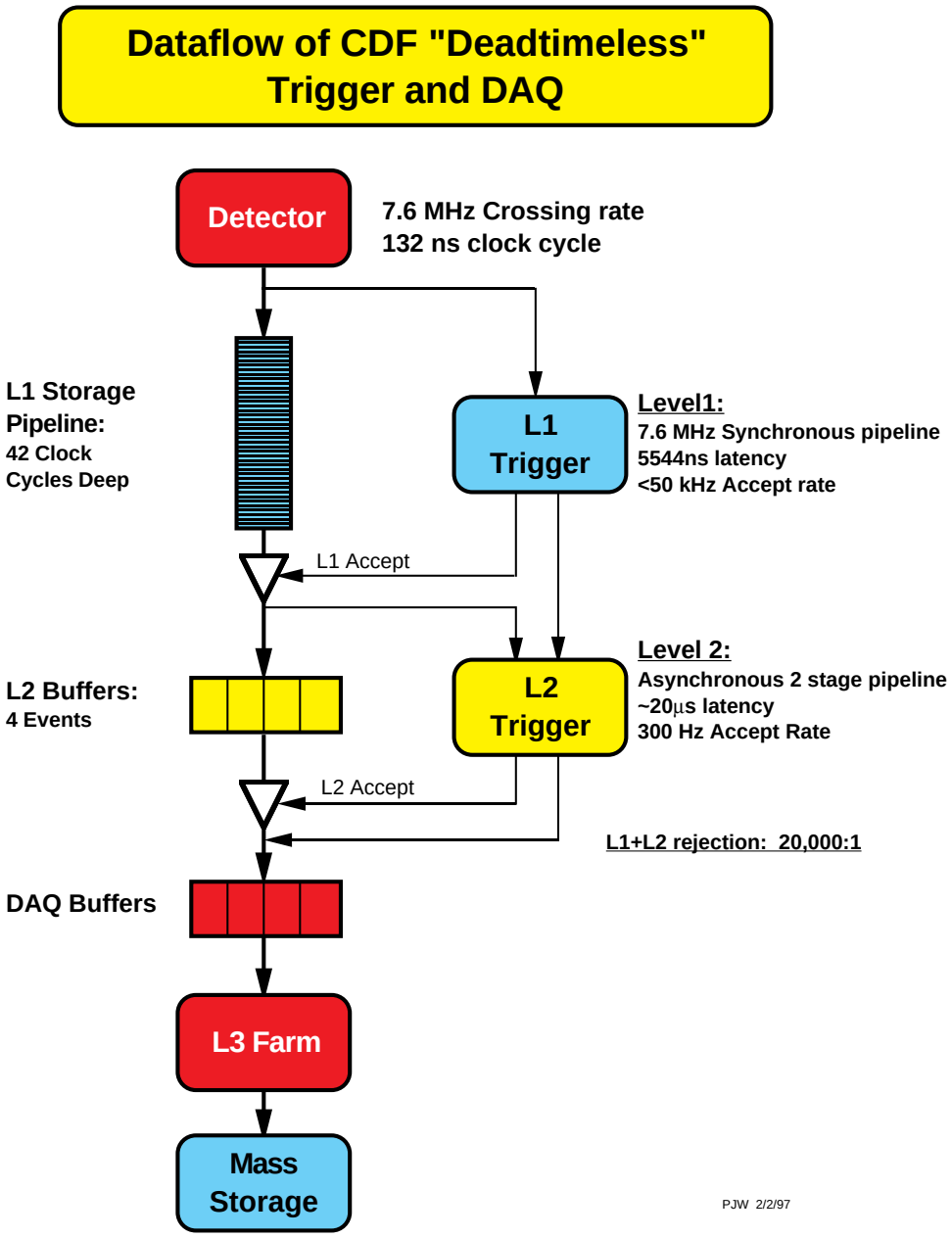

Figure 2.21: Trigger System Flowchart for CDF. This diagram shows the maximum rate which the trigger system was designed to handle. We are currently running at a 2.5 MHz input rate into Level-1, and a 20 kHz output rate from Level-1.

SUNG KYUN KWAN UNIVERSITY

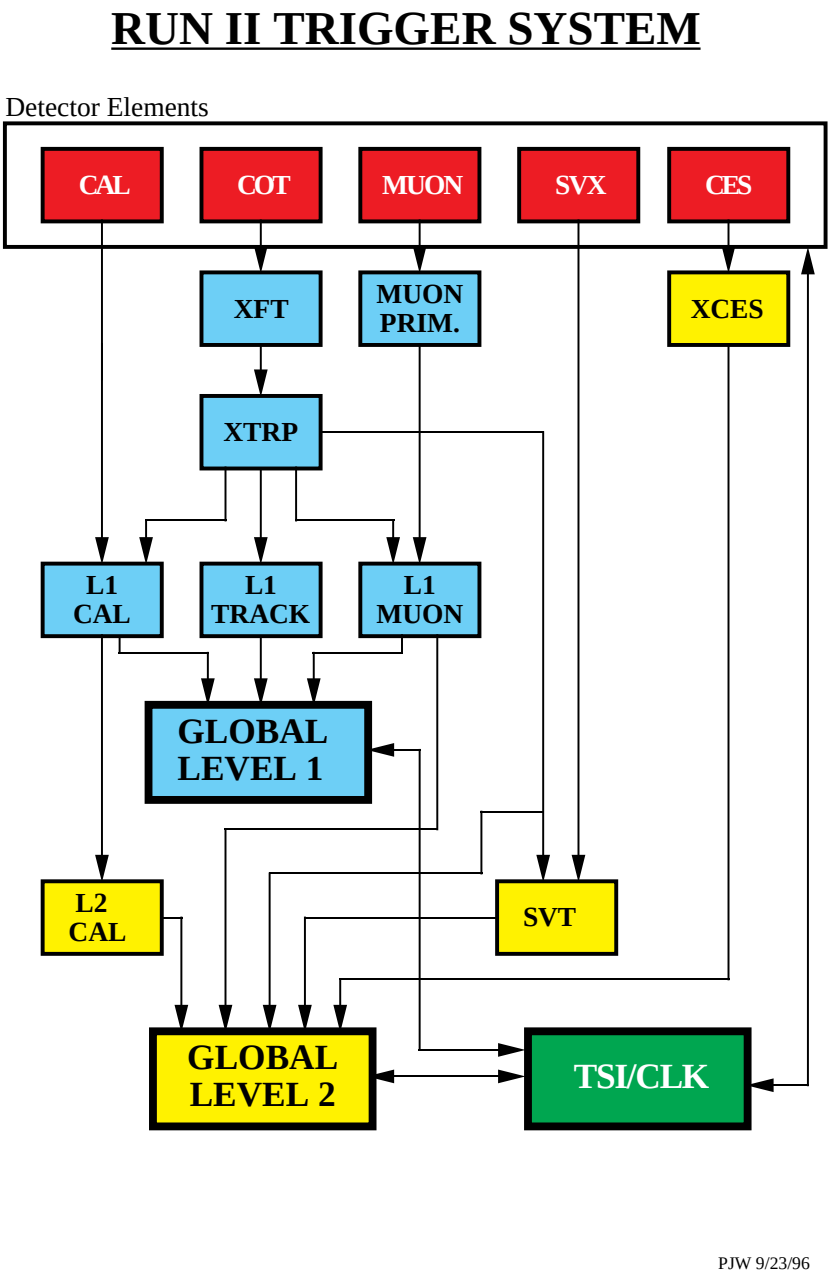

Figure 2.22: Block diagram of the Run II trigger system at CDF.

SUNGKYUNKWAN UNIVERSITY

Chapter 3

Data selection

In this chapter we disscuss the data selection criteria for the B_c analysis. We begin with the new di-muon trigger scheme and basic track treatment. Low energy electron is introduced as the second step. Then, we give the hadron faking probablity as an electron in the CDF detector.

3.1 J/ψ trigger

The J/ψ trigger consists of the several di-muon trggers at each the Level-1, the Level-2 and Level-3 trigger. Both muons from the CMU detector or the combination of two muons that one muon from the CMU and the other muon from the CMX is the first requirement at the Level-1 . The p_T of 1.5 and 2.2 GeVis required for each CMU and CMX muon to fire the trigger. The data from Level-1 undergo the Level-2 pass. The opening angle between two muon legs are inspected. Also the opposited charege of two muon is required in Level-2. At the Level-3 low level analysis is performed to find J/ψ candidates. The invariant mass windows of J/ψ is directly applied in this level. Di-muon trigger names are summarized in Table 3.1

SUNGKYUNKWAN UNIVERSITY

Level-1 Trigger
L1_TWO_CMU_PT1.5
L1_CMU1.5_PT1.5_&_CMX1.5_PT2_CSX
Level-2 Trigger
L2_TWO_CMU1.5_PT1.5_DPHI120_OPPQ_DPS
L2_CMU1.5_PT1.5_&_CMX1.5_PT2_DPHI120_OPPQ
Level-3 Trigger
L3_JPSI_CMUCMU
L3_JPSI_CMUCMX

Table 3.1: J/ψ trigger table.

3.2 Data sample

The total amount of 360 pb^{-1} of data was collected from the CDF detector and was used for the reconstruction of $B_c \to J/\psi e\nu$ and $B^+ \to J/\psi K^+$. This data sample passed di-muon trigger. In specific, events from "good runs" of 138809 to 186598 in dataset processed using 5.3.1 offline production, xpmm0d, were used. The "good run" definition follows the recommendation of the B-group [48]. For this time, COT "compromised runs" (179056 - 182843) and "recovery-runs" (184062-184208) were not used. Offline version 5.3.3 and the calibration table *PROD_PHYSICS_CDF* with *PASS13A* were used to make ntuples before further Root analysis.

3.3 Track treatment

The track selection starts with the defalut track collection in an event. Additional criteria is applied to choose better measured tracks. The track is required to have at least 20 COT axial and 16 COT stereo hits, and have $r-\phi$ hits from at least 3 Silicon hits to ensure good vertex resolution. The COT covariance matrix scaling and magnetic filed calibration were made following prescription in reference [49]. The energy loss correction procedure follows the prescription from reference [49] using C^{++} method *TrackRefitter*. Silicon

SUNGKYUNKWAN UNIVERSITY

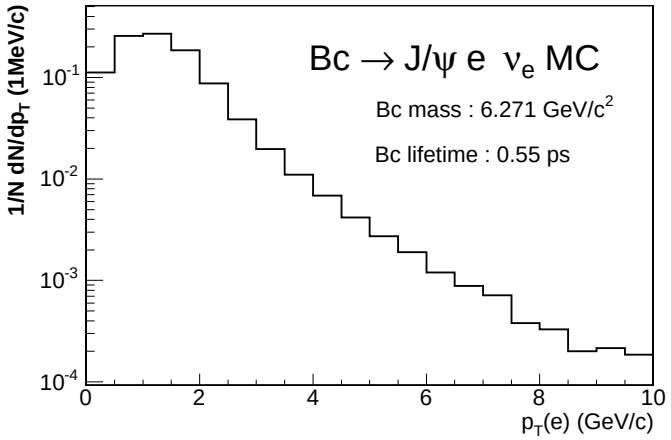

Figure 3.1: Electron p_T distribution from $B_c \to J/\psi e\nu$ monte caro simulation. We assume the mass of B_c is 6.271 GeV/c^2

hits from ISL are included when available but the hits from L00 are dropped before perfrom the track refit. The COT specific ionization dE/dX value for the track is obtained following scheme described in reference [50]. Tracks used in all decay channels used in this analysis were required to pass these selection criteria.

3.4 Electron identification

The electrons produced by B_c semileptonic decay have the soft p_T distribution. Figure 3.1 shows electron pT distribution from $B_c \to J/\psi e\nu$ monte caro at generator level. For low energy electron identification studies, we also reconstructed $\gamma \to e^+e^-$ from the 8 GeV single electron-triggered sample and $D^0 \to K\pi$ and $\Lambda^0 \to p\pi$ from the 2-track trigger sample. The "good runs" range as that for J/ψ sample were also used for photon conversion, D^0 and Λ^0 reconstruction.

SUNGKYUNKWAN UNIVERSITY

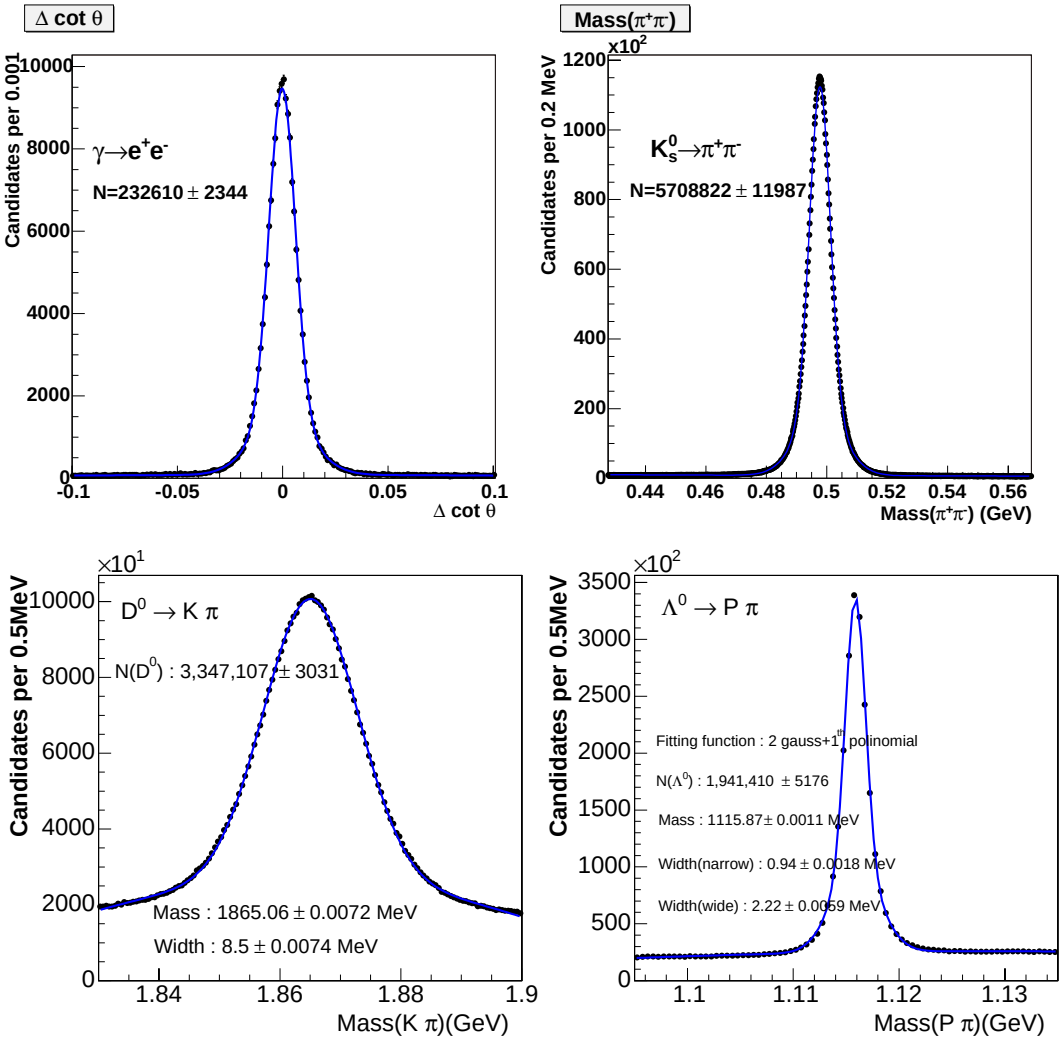

Figure 3.2: Distributions of $\Delta\cot\Theta$ of di-electron in photon conversion (top left), di-pion invariant mass from $K_s \to \pi^+\pi^-$ (top right). $K-\pi$ invariant mass from $D^0 \to K^-\pi^+$ (bottom left), and $p-\pi$ invariant mass from $\Lambda^0 \to p\pi^-$ (bottom right). Electron candidates are selected by requiring $|\Delta\cot\Theta| < 0.05$ and -0.3 cm< d_{xy} <0.5 cm in photon conversion sample. Pion, kaon and proton are selected from invariant mass within 3σ of the PDG values of K_s,D^0 and Λ^0 masses.

SUNGKYUNKWAN UNIVERSITY

3.4.1 Low electron identification algorithm and the variables from the algorithm

The electron identification process starts with "the soft electron objects" reconstructed by a C^{++} Module *SoftElectronMods* using a track-based electron-reconstruction algorithm [52, 53]. The algorithm takes a good quality track with a minimal transverse momentum (p_T) of 1 GeV/c and extrapolates it to the Central Strip chamber (CES) and the Central Preradiator (CPR). The track is extrapolated as a helix up to the solenoid where CPR is located behind and then as a straight line further to CES. Along the projected trajectory, Central ElectroMagenetic calorimeter (CEM) towers, CES clusters, CPR clusters are sorted and matched to the trajectory to form the electron objects. The CPR and CES clustering algorithms are described in references [54, 55]. The match to the CEM tower is done using η and ϕ positions and a hit tower is required to have a minimal energy of 50 MeV/c^2. A 2-tower cluster is formed using the nearest tower in Z to the hit tower and the total electromagnetic (EM) energy and hadronic (HAD) energy are calculated from these two towers.

The CES fiducial coverage requires that the track hit position within 21 cm in X_{CES} and in between 9 cm - 230 cm in Z_{CES} on the tower center, where X_{CES} and Z_{CES} are the local coordinates of the calorimeter tower in $r-\phi$ and Z views. The CPR fiducial coverage requires that the track hit position within 16 cm in X_{CPR} and in between 8.4 cm - 118 cm and 125 cm - 200 cm in Z_{CPR}. The fiducial coverage is about 85% for CES and 70% for CPR. Electron candidates are required to be in the fiducial coverage of CES but not necessarily in the CPR fiducial. All the CES/CEM related selection cuts will apply to electron candidate but the CPR related selection cuts will apply only if the electron candidate is determined in the CPR fiducial. Below is the list of the variables for the soft electron object reconstructed from *SoftElectronMods* module.

- E_{had}/E_{em}

  This is the ratio of the energy measured in the hadronic calorimeters of the Central Hadronic Calorimeter (CHA) and the endWall Hadronic

SUNGKYUNKWAN UNIVERSITY

Calorimeter (WHA) to that from the CEM for the two-tower cluster. An real electron has a smaller E_{had}/E_{em} value.

- E/P

  This is the ratio of the transverse energy in the EM cluster to the associated track's transverse momentum measured in COT. An real electron is to deposit most of its energy in the CEM calorimeter and has the ratio around 1.

- Pull of $Q \cdot \Delta X_{CES}$

  ΔX_{CES} is the distance in the $r-\phi$ plane between the extrapolated track position and the best-matching CES cluster position. Q is the charge of the track. The measurement error of $Q \cdot \Delta X_{CES}$ is studied using pure electron in the conversion sample and parameterized as function of p_T. The pull distribution, $Q \cdot \Delta X_{CES}/\sigma_{Q\cdot\Delta X_{CES}}$, is expected to be between ± 3 for real electrons.

- Pull of ΔZ_{CES}

  ΔZ_{CES} is the distance in the $r-Z$ plane between the extrapolated track position and the best-matching CES cluster position. The ΔZ_{CES} distribution does not have a charge asymmetry. The measurement error of ΔZ_{CES} was studied using pure electron in the conversion sample and parameterized as function of p_T. The pull distribution $\Delta Z_{CES}/\sigma_{\Delta Z_{CES}}$ is expected to be within ± 3 for electrons.

- CES shower profile comparison χ^2_{strip}

  This is the χ^2 comparison of the CES shower profile in the $r-Z$ view (by the scintillator strip) with the same profile extracted from test beam electrons. Real electrons are expected to have smaller χ^2_{strip} values.

- CES shower profile comparison χ^2_{wire}

  This is the χ^2 comparison of the CES shower profile in the $r-\phi$ view (by the wire chamber) with the same profile extracted from test beam electrons. Electrons are expected to have smaller value of χ^2_{wire}.

SUNGKYUNKWAN UNIVERSITY

- CES pulse height E_{CES}/p^*

  This is the shower energy measured from the 7-wire cluster's pulse height in the unit of GeV scaled by the $p^* = 10 \cdot (p/10)^\alpha$ with $\alpha = 0.85 + 0.15 \cdot e^{-p/15} - p/1000$ where p is the track momentum. The value of E_{CES}/p^* for an electron is expected to be approaching 1.

- CES pulse height ratio E_{strip}/E_{wire}

  This is ratio of the pulse heights between the $r - Z$ measurement of scintillator strip and $r - \phi$ measurement of wire chamber. The electrons tend to have larger value of the ratio while hadrons tend to have smaller ratio.

- CPR cluster energy E_{CPR}

  The preradiator energy is determined by summing the charges of the 3 CPR wires in the associated CPR cluster. A parameterized correction [52] is done to reduce momentum dependence. The value of E_{CPR} tends to be larger for electron than for hadron since electron loses more energy in the CPR.

- ΔX_{CPR}

  This is the distance in the $r - \phi$ plane between the extrapolated track position and the best-matching CPR cluster position. A smaller value of ΔX_{CPR} indicates a good matching.

- dE/dx

  For low momentum electrons, the specific ionization in COT dE/dx is also a very powerful variable to reject hadron fakes. We will discuss the use of dE/dx for electron identification in later section.

- Conversion electron removal

  In most of the B semileptonic decay reconstructions, it is desirable to remove the electrons from photon conversion $\gamma \to e^+e^-$ generated from interaction in the detector material. Electron pair from the photon conversion is identified by using variables of $\Delta \cot\Theta$ and d_{XY}, where $\Delta \cot\Theta$

SUNGKYUNKWAN UNIVERSITY

is simply the difference of track parameter $\cot\Theta$ of the two tracks and the d_{XY} is found by first collapsing the helices of the two tracks into two circles on the $r-\phi$ plane and then take the distance at the point where the two circles are parallel to each other. In this analysis, electron candidates were to be rejected if a partner track with $p_T > 400$ MeV/c found which satisfies the conversion criteria $|\Delta\cot\Theta| < 0.05$ and $-0.3\ cm < d_{XY} < 0.5\ cm$.

- Isolation The isolation variable for an electron is defined as the ratio between the scalar sum of p_T for tracks projected into the same EM tower as the the electron track and in a cone of $\Delta R = \sqrt{(\Delta\eta)^2 + (\Delta\phi)^2} < 0.7$ surrounding the electron track to the p_T of the electron track, $I = \sum p_T(i)/p_T(e)$. Electron reconstruction efficiency and fake rate are found to be a function of the isolation variable.

We studied these variables using pure electrons reconstructed from photon conversion, $\gamma \rightarrow e^+e^-$, and hadrons from $K_s \rightarrow \pi^+\pi^-$, $D^0 \rightarrow K^-\pi^+$ and $\Lambda^0 \rightarrow p\pi^-$. Details on the data sample and selection criteria for these events are in Appendix . In Figire. 3.2, the signals for these decays are shown.

The distributions of the E_{had}/E_{em}, E/P, pulls of $Q\cdot\Delta X_{CES}$ and ΔZ_{CES}, CES shower profiles χ^2_{strip} and χ^2_{wire}, CES pulse height E_{CES}/p^*, CES pulse height ratio E_{strip}/E_{wire}, and CPR cluster energy E_{CPR} and position ΔX_{CPR} for electrons and hadrons are shown in Figires. 3.3. For all these plots, sideband subtraction technique was employed to improve purity of electron and hadron samples.

SUNGKYUNKWAN UNIVERSITY

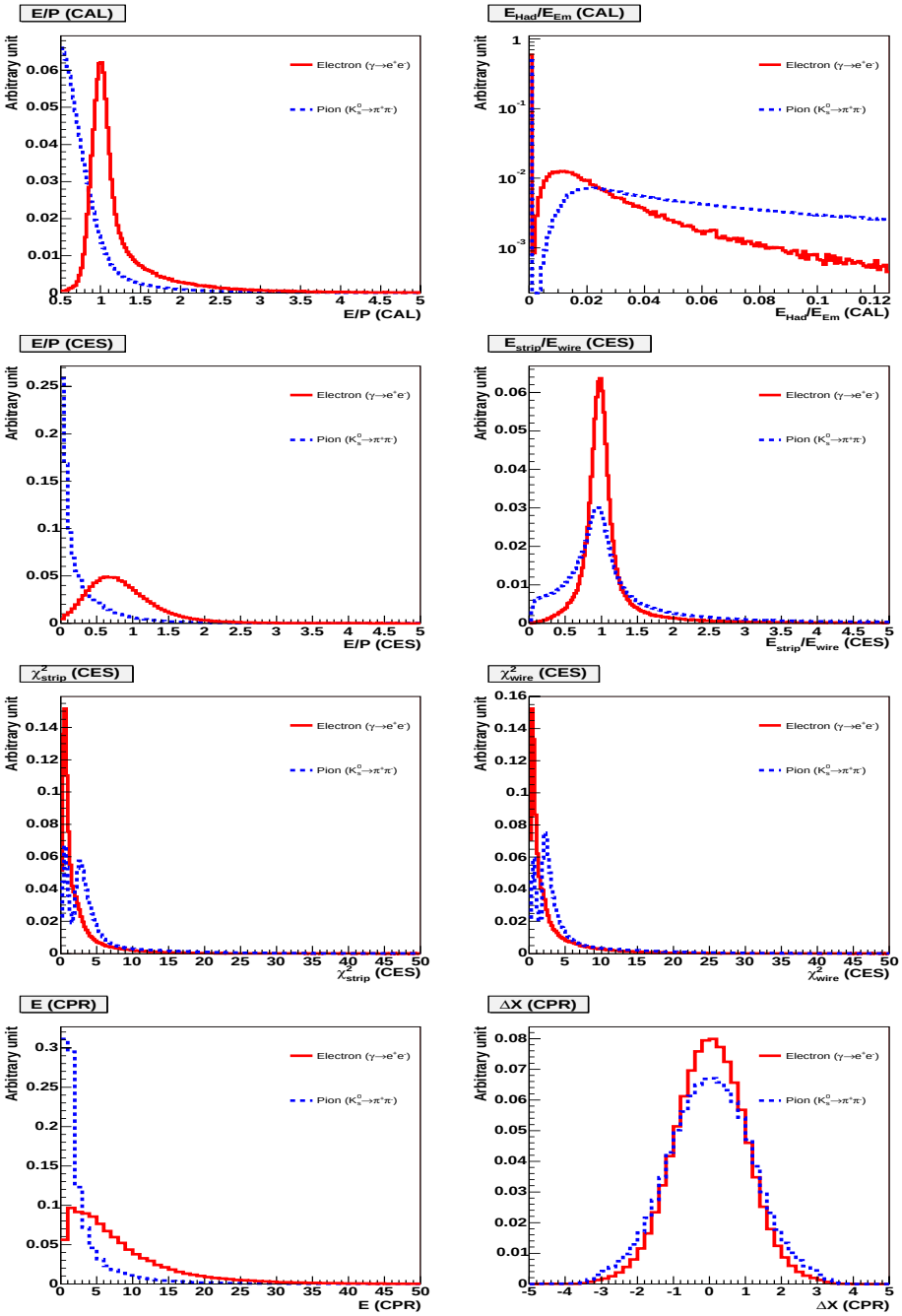

Figure 3.3: Distributions of the electron identification variables for electrons (red, solid lines) and pions (blue, dashed lines).

SUNG KYUN KWAN UNIVERSITY

Table 3.2: Electron selection variables and their efficiencies (%).

	"Loose"		"Standard"		"Tight"	
Variable	cut	efficiency	cut	efficiency	cut	efficiency
E_{had}/E_{em}	0.1	92.7	0.05	87.0	0.1	83.5
E/P	0.4	93.1	0.7	92.6	0.8	89.3
$\mid \Delta X_{CES} \mid$	3	97.4	3 cm	97.4	2	94.2
$\mid \Delta Z_{CES} / \mid$	3	95.4	3 cm	95.4	2	92.1
χ^2_{strip}	30	99.5	20	98.8	5	84.5
χ^2_{wire}	30	99.8	20	99.6	5	87.3
E_{CES}/p^*	0.1	96.5	0.2	93.6	0.4	83.1
E_{strip}/E_{wire}	0.3	99.2	0.65	93.7	0.9	72.4
E_{CPR}	0.7	96.9	1.5	87.1	3	72.9
ΔX_{CPR}	3	99.7	3 cm	99.7	3	99.7

3.4.2 Cuts for electron identification

We determined cuts by comparing distributions of the electron identification variables between electrons and hadrons. we selected three sets of selection as listed in Table 3.2. The "standard cut" is chosen by requiring each of the variables having efficiency around 90%. The efficiency curves for each variables for electron and hadrons are displayed in Figire. 3.4. the overal electron identification efficiency for the "standard set cuts" is measured using the electrons from photon conversion decay $\gamma \to e^+e^-$, as shown in Figire. 3.5 and tabulated in Table 3.3.

The hadron faking electron probabilities are measured by applying the electron selection cuts to the hadron tracks identified by physics signatures of $D^0 \to K^-\pi^+$ and $\Lambda^0 \to p\pi^-$. In Figire 3.6, Figire 3.7 and Figire 3.8, the D^0 and Λ^0 invariant mass distributions are shown for pion, kaon and proton tracks in the CES fiducial before and after applying the electron selection cuts. The D^0 mass fitting follows the technique described in reference [56] where the fitting function consists of a narrow Gaussian describing the signal with correct K/π mass assignment, another Gaussian with the same mean as

SUNGKYUNKWAN UNIVERSITY

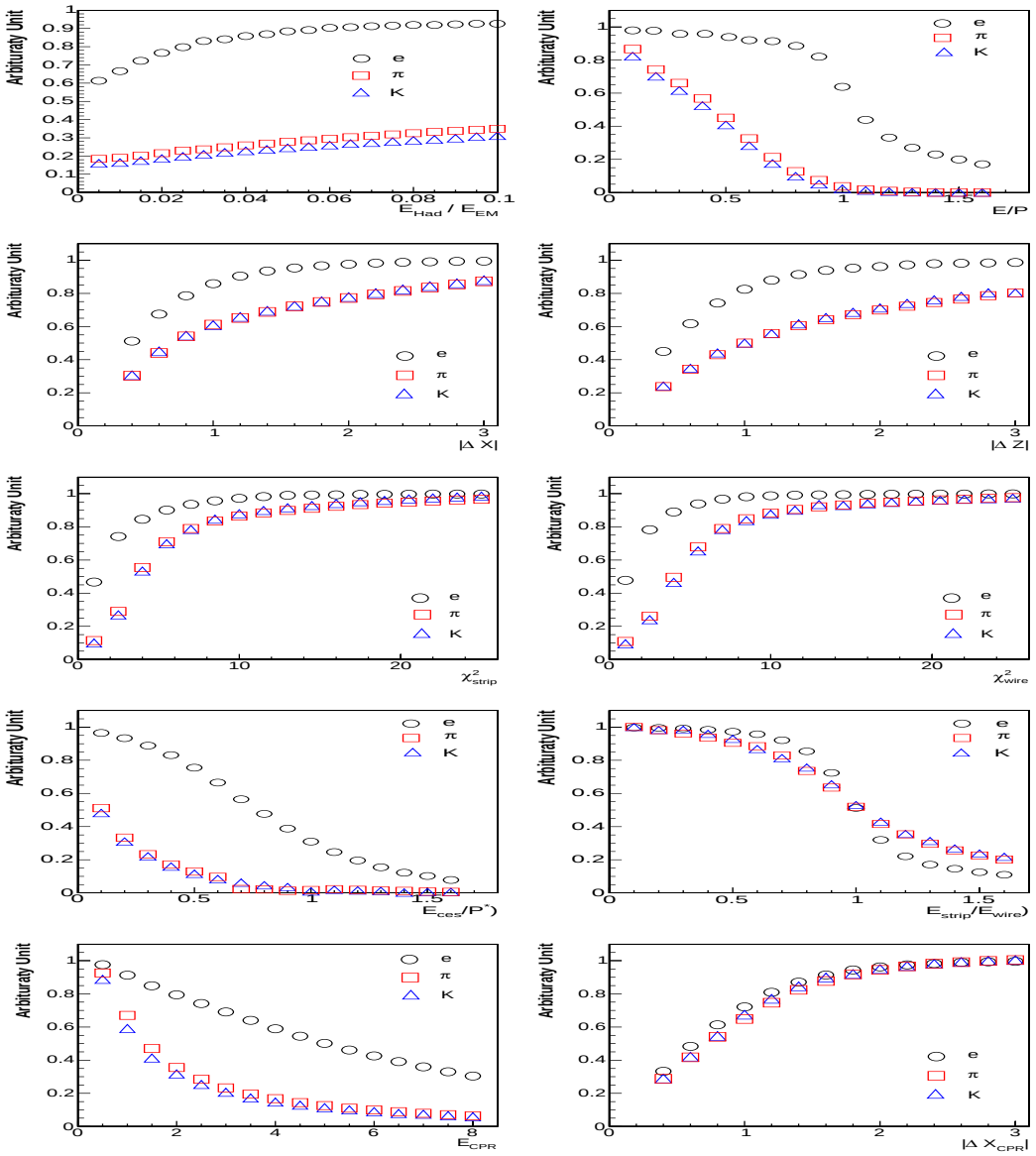

Figure 3.4: Cut efficiency curves of electron (circles), pion (squares) and kaon (triangles) tracks for the 10 electron identification variables.

SUNGKYUNKWAN UNIVERSITY

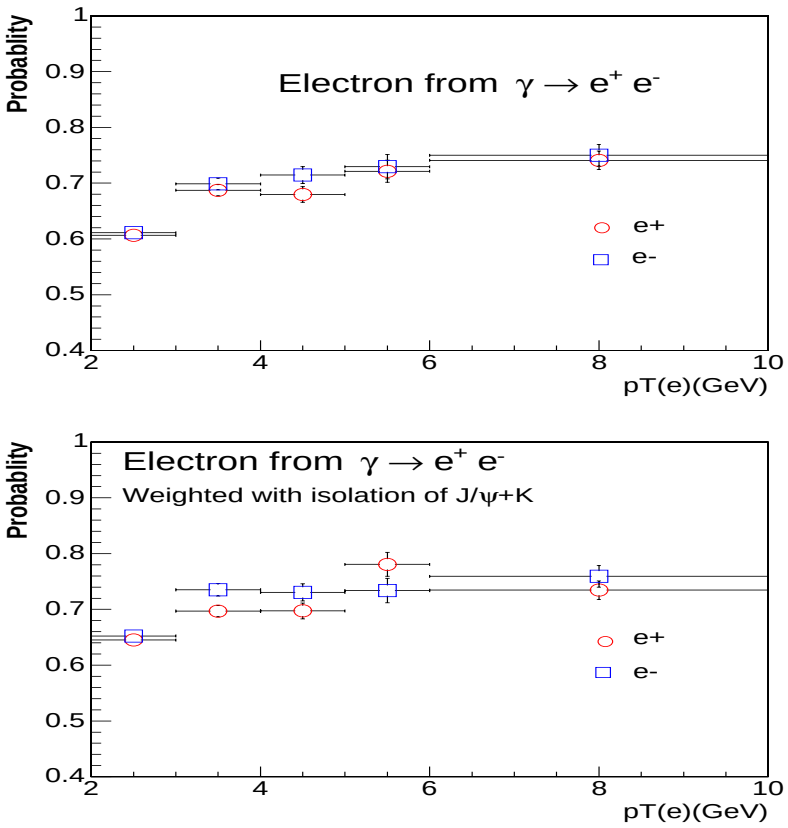

Figure 3.5: Electron identification efficiency with selection cuts listed in Table 3.3. The efficiencies are measured using electrons from $\gamma \to e^+e^-$. Red dots are for positively charged electrons and blue dots are for negative charged electrons. The top plot is the result directly from using $\gamma \to e^+e^-$ sample. The bottom plot is the result after re-weighting the events to make the isolation distribution the same as the ones from $B^+ \to J/\psi K^+$ sample.

SUNGKYUNKWAN UNIVERSITY

Table 3.3: Efficiency of electron selections.

	Before weighting		After weighting	
p_T (GeV/c)	$\epsilon(e^+)(\%)$	$\epsilon(e^-)(\%)$	$\epsilon(e^+)(\%)$	$\epsilon(e^-)(\%)$
2-3	60.64 ± 0.61	61.10 ± 0.63	64.5 ± 0.65	65.23 ± 0.67
3-4	68.73 ± 1.02	69.86 ± 1.06	69.69 ± 1.03	73.52 ± 1.12
4-5	67.96 ± 1.39	71.45 ± 1.51	69.73 ± 1.43	73.05 ± 1.54
5-6	72.13 ± 1.97	72.94 ± 2.19	78.07 ± 2.14	73.39 ± 2.20
> 6	74.09 ± 1.66	74.99 ± 1.91	73.46 ± 1.65	75.93 ± 1.94

the narrow Gaussian but a much wider width describing the reflection from the wrong K/π mass assignment, and a first order polynomial for the combinatorial background. The fake rate is simply defined as the ratio of fitted D^0 or Λ^0 events before and after passing the stanard electron cuts. The fake rate were also obtained this way for different track p_T bins, as shown in Figire 3.10 to Figire. 3.11 and tabulated in Table 3.4 , 3.5 and 3.6. Muon track from $J/\psi \to \mu^+\mu^-$ is also used to measure its ability to fake electron. The probability is found to be very small for muon to fake electron and we will ignore the muon track contribution in the electron fake rate calculation from now on.

Isolation distribution for photon conversion, D^0, and Λ^0 samples are similar to that of the $J/\psi \to \mu\mu$ sample but small differences do exist as shown in Figire. 3.12. To take into account the effect from isolation difference, the events used for the calculation were re-weighted to force them have similar isolation distributions to $B^+ \to J/\psi K^+$ events during efficiency calculation and to J/ψ+track events during fake rate calculation.

3.4.3 dE/dx for electron identification

The specific ionization dE/dx in COT is a powerful variable to separate electron tracks from hadron tracks. The dE/dx calibration procedures were described in references [50, 57]. We use the logarithm ratio between the measured dE/dx value and expected value for electron tracks, called Z_e, to help the

SUNGKYUNKWAN UNIVERSITY

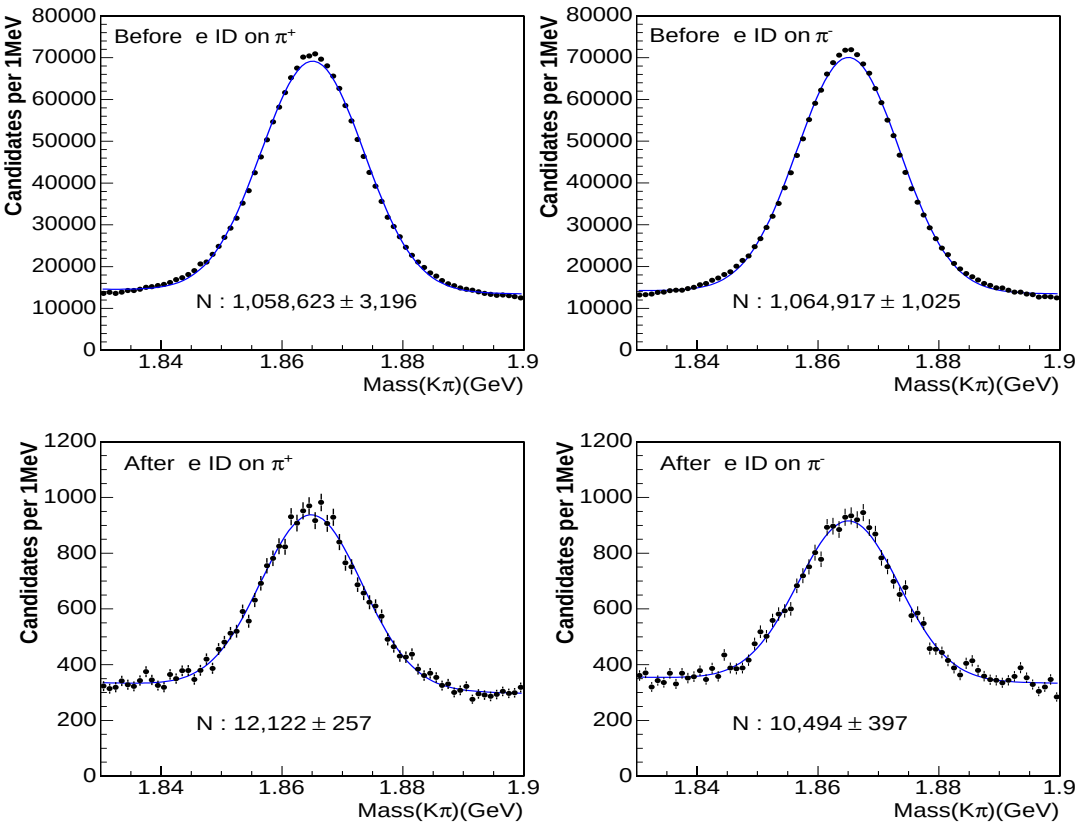

Figure 3.6: D^0 mass distributions for pion tracks in the CES fiducial before (top) and after (bottom) applying the standard electron selection cut. Positively charged tracks are on the left and negatively charged tracks on the right.

SUNGKYUNKWAN UNIVERSITY

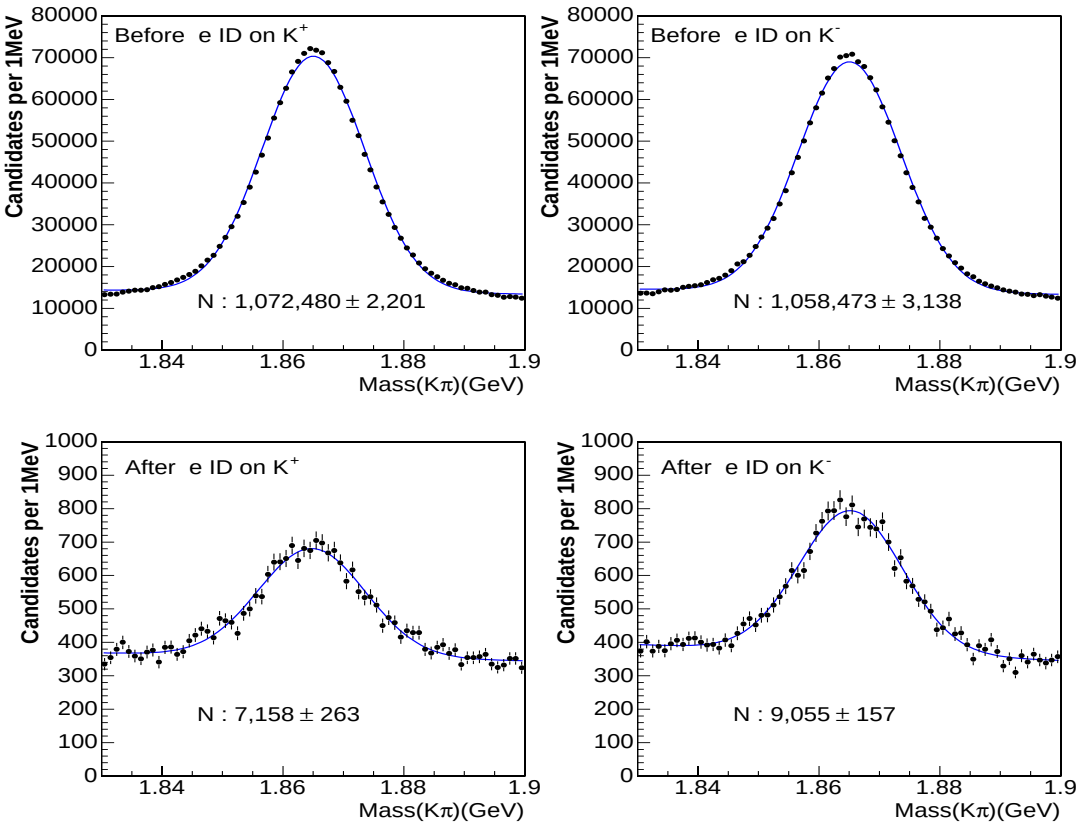

Figure 3.7: D^0 mass distributions for kaon tracks in the CES fiducial before (top) and after (bottom) applying the standard electron selection cut. Positively charged tracks are on the left and negatively charged tracks on the right.

SUNGKYUNKWAN UNIVERSITY

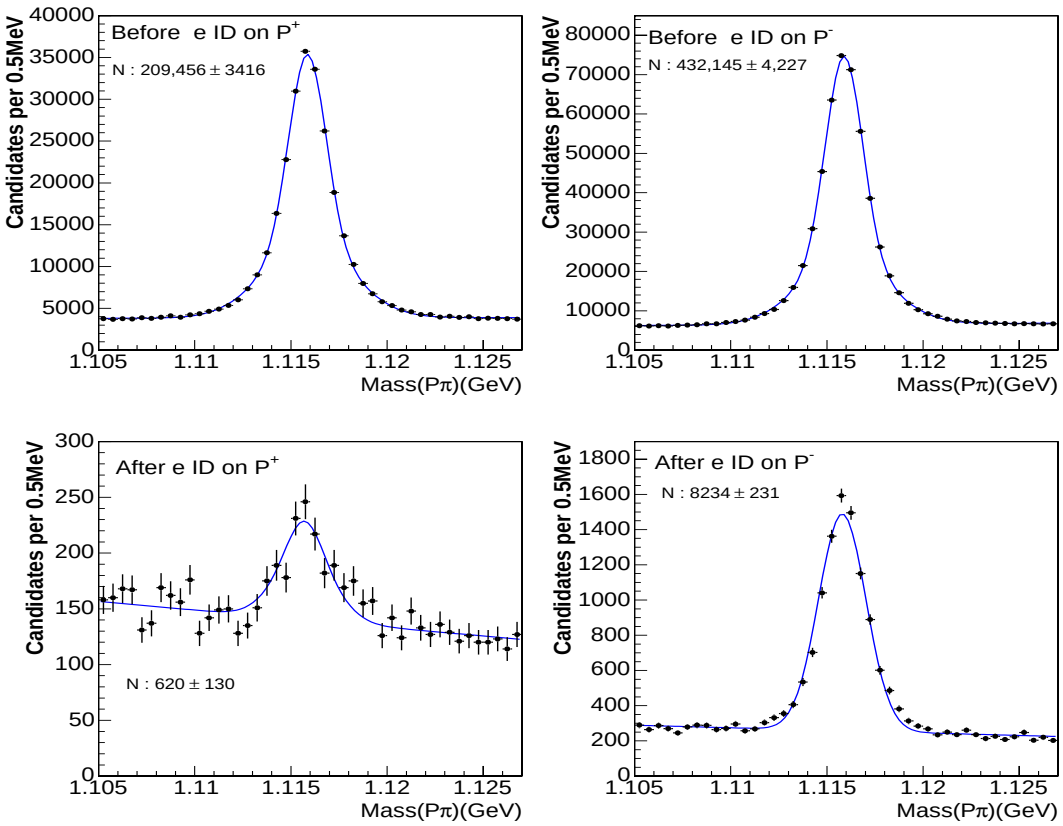

Figure 3.8: Λ^0 mass distributions for proton tracks in the CES fiducial before (top) and after (bottom) applying the standard electron selection cut. Positively charged tracks are on the left and negatively charged tracks on the right.

SUNGKYUNKWAN UNIVERSITY

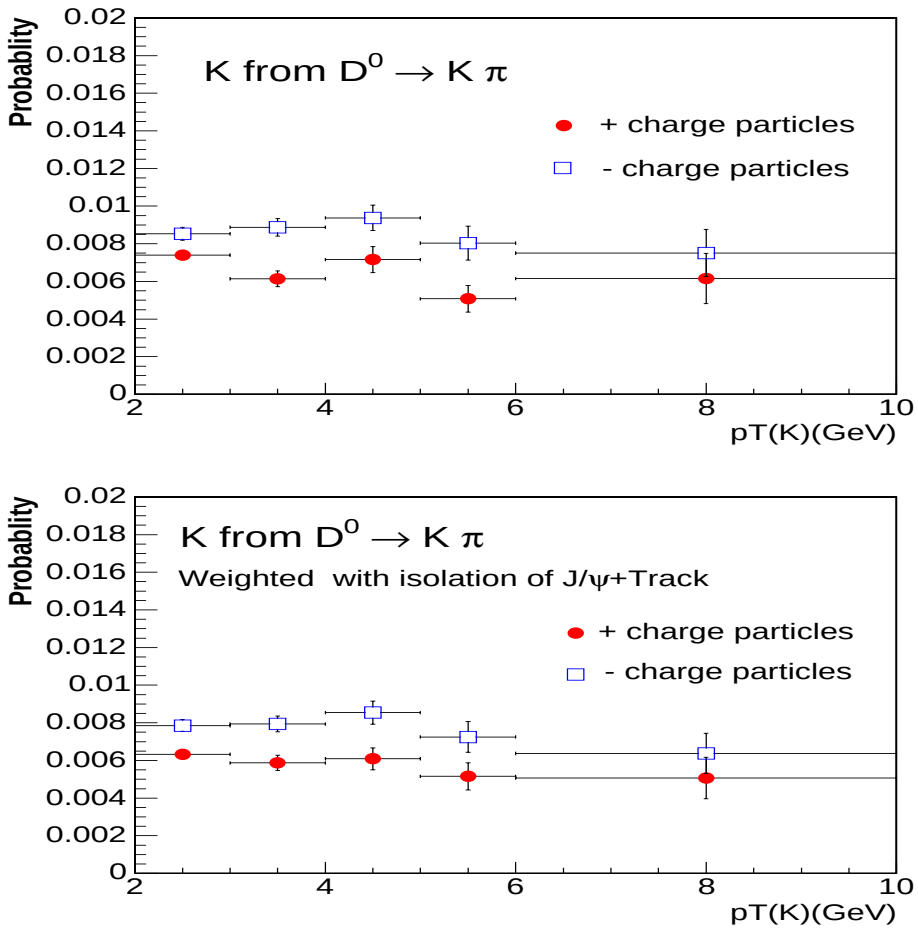

Figure 3.9: Kaon faking electron probabilities as function of tracking p_T. Kaons are selected from decay $D^0 \rightarrow K\pi$. Mass fitting at each track p_T bins are used to obtain the number of tracks passing and failing the electron selection. Top plot is the result directly from $D^0 \rightarrow K\pi$ sample and bottom plot is the one where each event is re-weighted to force them have same isolation distribution as in J/ψ+track sample.

SUNGKYUNKWAN UNIVERSITY

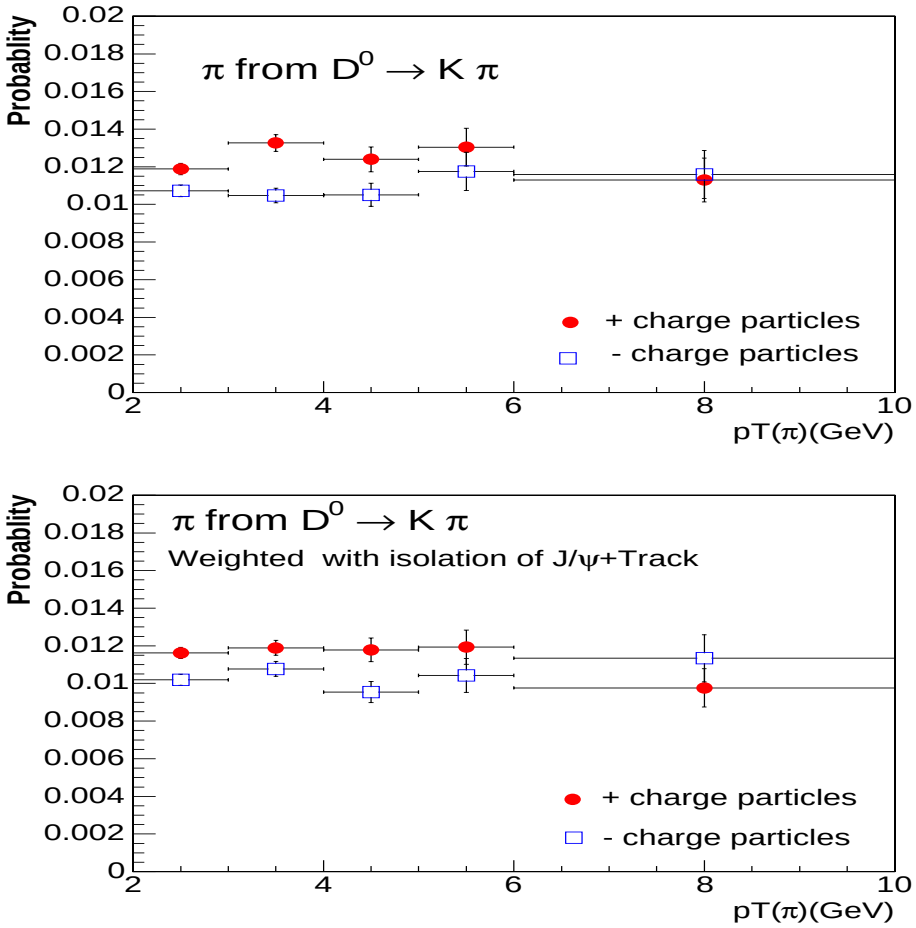

Figure 3.10: Pion faking electron probabilities as function of tracking p_T. Pions are selected from decay $D^0 \to K\pi$. Mass fitting at each track p_T bins are used to obtain the number of tracks passing and failing the electron selection. Top plot is the result directly from $D^0 \to K\pi$ sample and bottom plot is the one where each event is re-weighted to force them have same isolation distribution as in J/ψ+track sample.

SUNGKYUNKWAN UNIVERSITY

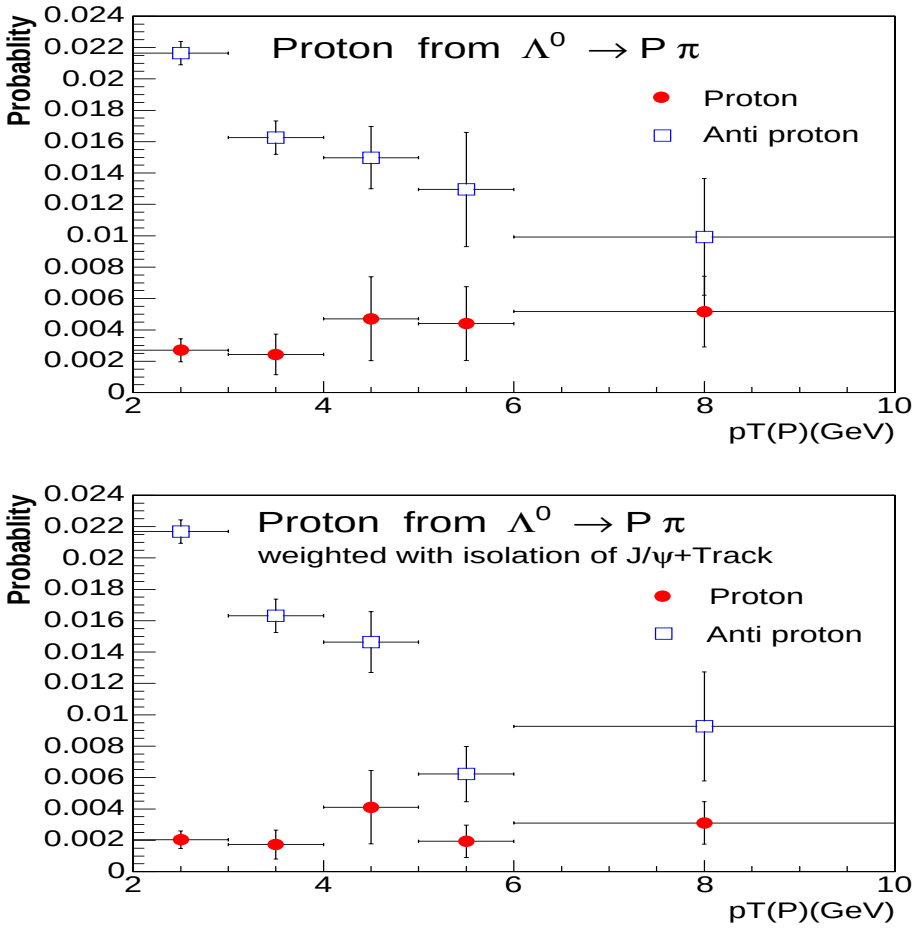

Figure 3.11: Proton faking electron probabilities as function of track p_T. Protons are selected from decay $\Lambda^0 \rightarrow p\pi$. Mass fitting at each track p_T bins are used to obtain the number of tracks passing and failing the electron selection. Top plot is the result directly from $D^0 \rightarrow K\pi$ sample and bottom plot is the one where each event is re-weighted to force them have same isolation distribution as in J/ψ+track sample.

SUNGKYUNKWAN UNIVERSITY

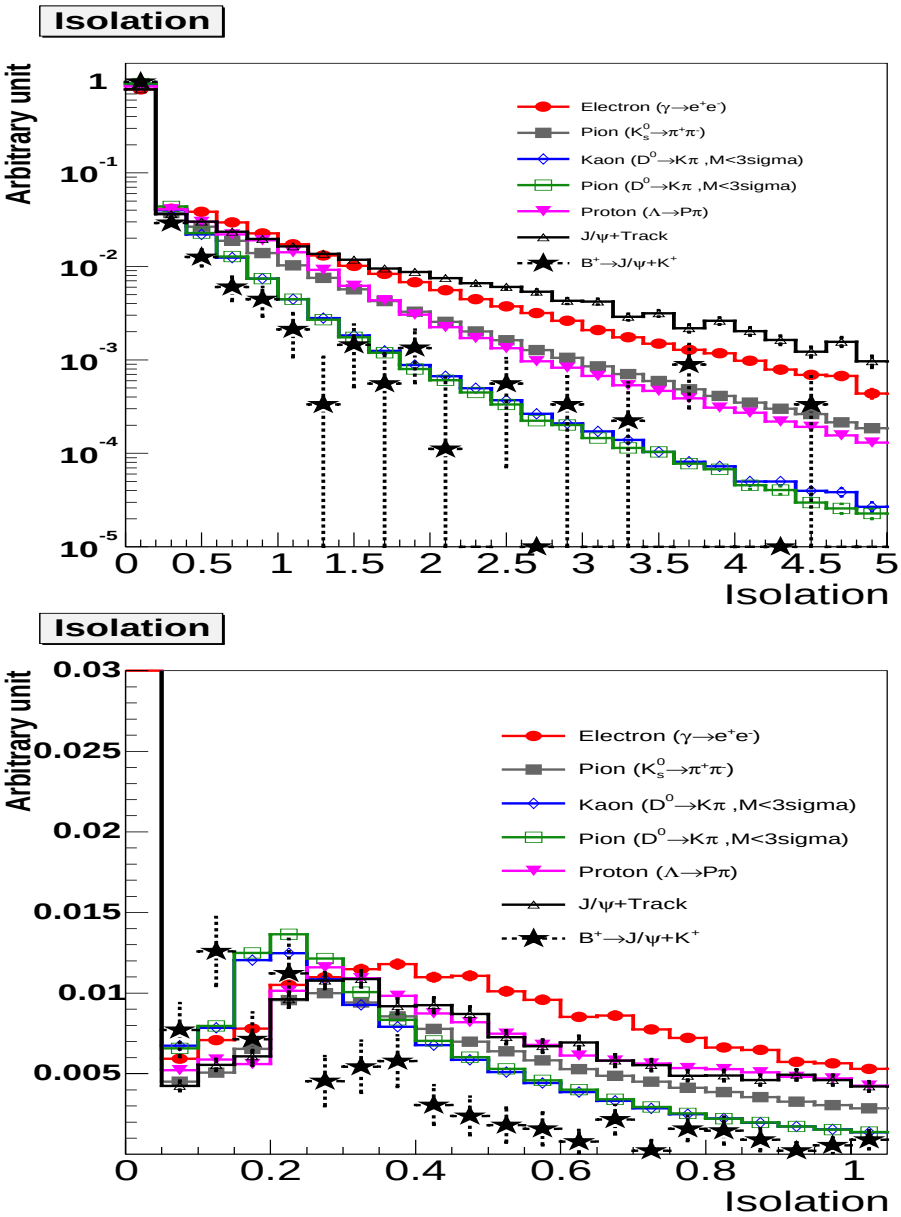

Figure 3.12: Distributions of the isolation variables for different samples used for the electron identification studies. The bottom plot is a zoom-in of the top one.

SUNGKYUNKWAN UNIVERSITY

Table 3.4: Kaon faking electron probabilities (%) as function of track p_T. Right two columns are weighted to force them have the same isolation distribution as that in J/ψ+track sample.

p_T (GeV/c)	K^+	K^-	K^+	K^-
2-3	0.740 ± 0.012	0.853 ± 0.035	0.632 ± 0.010	0.785 ± 0.032
3-4	0.614 ± 0.042	0.888 ± 0.047	0.59 ± 0.04	0.79 ± 0.04
4-5	0.715 ± 0.069	0.937 ± 0.067	0.61 ± 0.06	0.85 ± 0.06
5-6	1.304 ± 0.099	1.18 ± 0.10	0.52 ± 0.07	0.72 ± 0.08
> 6	0.62 ± 0.13	0.75 ± 0.13	0.51 ± 0.11	0.64 ± 0.11

Table 3.5: Paon faking electron probabilities (%) as function of track p_T. Right two columns are weighted to force them have the same isolation distribution as that in J/ψ+track sample.

p_T (GeV/c)	π^+	π^-	π^+	π^-
2-3	1.188 ± 0.031	1.072 ± 0.031	1.16 ± 0.03	1.02 ± 0.03
3-4	1.326 ± 0.044	1.047 ± 0.038	1.19 ± 0.04	1.08 ± 0.04
4-5	1.239 ± 0.066	1.051 ± 0.062	1.18 ± 0.06	0.95 ± 0.06
5-6	0.707 ± 0.070	0.803 ± 0.090	1.19 ± 0.09	1.04 ± 0.09
> 6	1.13 ± 0.12	1.16 ± 0.13	0.98 ± 0.10	1.13 ± 0.13

Table 3.6: Proton faking electron probabilities (%) as function of track p_T. Right two columns are weighted to force them have the same isolation distribution as that in J/ψ+track sample.

p_T (GeV/c)	P^+	P^-	p^+	p^-
2-3	0.169 ± 0.011	1.847 ± 0.025	0.204 ± 0.056	2.17 ± 0.07
3-4	0.105 ± 0.020	0.729 ± 0.031	0.173 ± 0.092	1.63 ± 0.11
4-5	0.115 ± 0.043	0.396 ± 0.056	0.41 ± 0.23	1.46 ± 0.19
5-6	0.081 ± 0.087	0.317 ± 0.097	0.19 ± 0.10	0.62 ± 0.18
> 6	0.013 ± 0.079	0.135 ± 0.088	0.31 ± 0.14	0.93 ± 0.35

SUNG KYUN KWAN UNIVERSITY

electron identification in addition to other variables described in the previous sections.

$$Z_e = log[(dE/dx)_{measurement}/(dE/dx)_{predict}] \tag{3.1}$$

In our case, the pull distribution defined as Z_e/σ_Z is used as the separation variable. The distributions of the mean value of Z_e/σ_Z and its width obtained for electrons from photon conversion sample and hadrons ($K/\pi/p/\mu$) using $D^0 \to K^-\pi^+$, $\Lambda^0 \to p\pi$ and $J/\psi \to \mu^-\mu^+$ decays, are shown in Figire. 3.13 and Figire. 3.14.

The pull distribution Z_e/σ_Z for electrons and hadrons for track momentum around 2 GeV are shown in Figire. 3.15. From the plot, one can see a cut of $Z_e/\sigma_Z > -1.3$ has a high efficiency for electrons while rejecting large fraction of the hadronic tracks. The efficiency of this cut as function of the track momentum is shown in Figire. 3.16. The efficiencies for positive and negative charged tracks are found to be consistent with each other so we will use the combined efficiencies for the B_c search. The numeric values of the efficiencies are listed in Table 3.7.

Table 3.7: The efficiency (%) of the dE/dx $Z_e/\sigma > -1.3$ cut as a function of track momentum for electron and hadron tracks. The measurement for positively and negatively charged tracks are found to be consistent and thus are combined.

p (GeV/c)	electron	kaon	proton	pion
2-3	91.30 ± 0.14	2.086 ± 0.088	3.380 ± 0.031	16.369 ± 0.075
3-4	91.39 ± 0.15	2.353 ± 0.071	2.138 ± 0.035	23.754 ± 0.098
4-5	90.66 ± 0.21	3.288 ± 0.087	2.537 ± 0.070	31.96 ± 0.12
5-6	90.52 ± 0.28	4.36 ± 0.12	3.03 ± 0.14	38.95 ± 0.15
> 6	89.54 ± 0.20	9.46 ± 0.15	4.91 ± 0.22	49.38 ± 0.16

SUNGKYUNKWAN UNIVERSITY

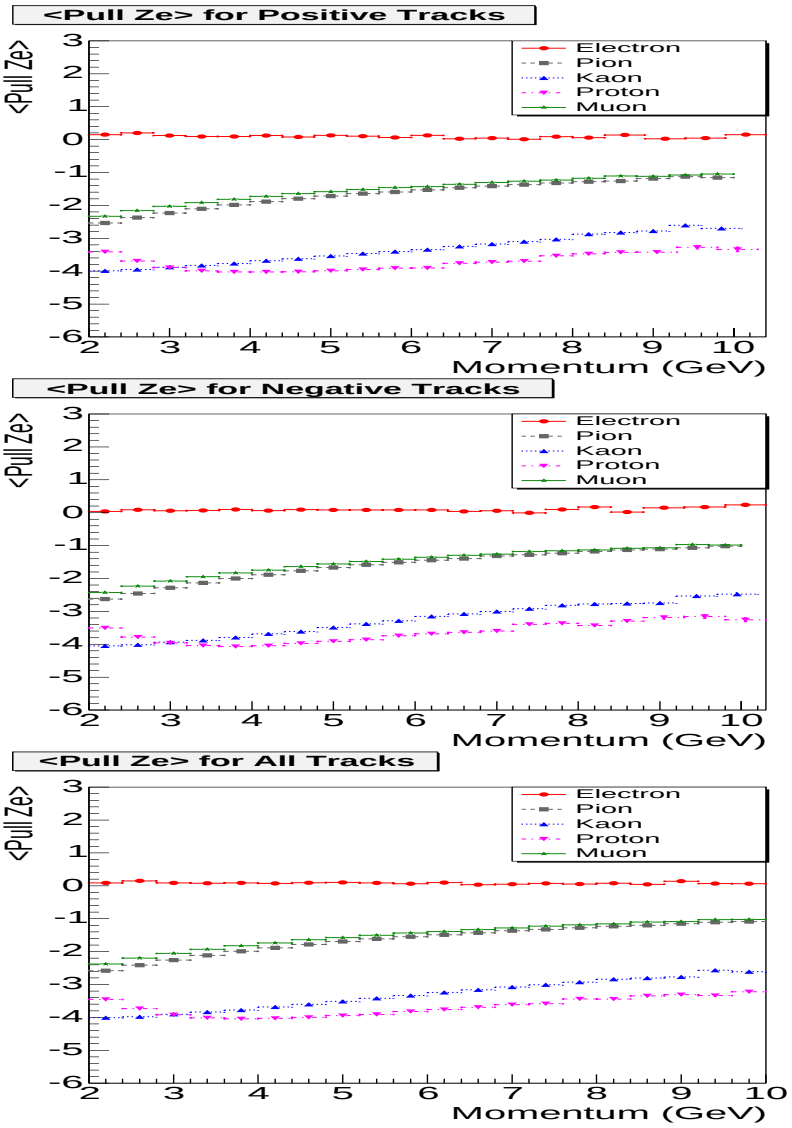

Figure 3.13: Distributions of the mean value of Z_e/σ_Z as function of the track momentum for positive charged tracks (top), negative charged tracks (middle) and all charged tracks (bottom). Electrons are selected from photon conversion decay, kaons and pions are from $D^0 \to K^-\pi^+$, protons are from $\Lambda^0 \to p\pi$ and muons are from $J/\psi \to \mu^-\mu^+$ decays. Sideband subtractions were used to purify the track selections.

SUNGKYUNKWAN UNIVERSITY

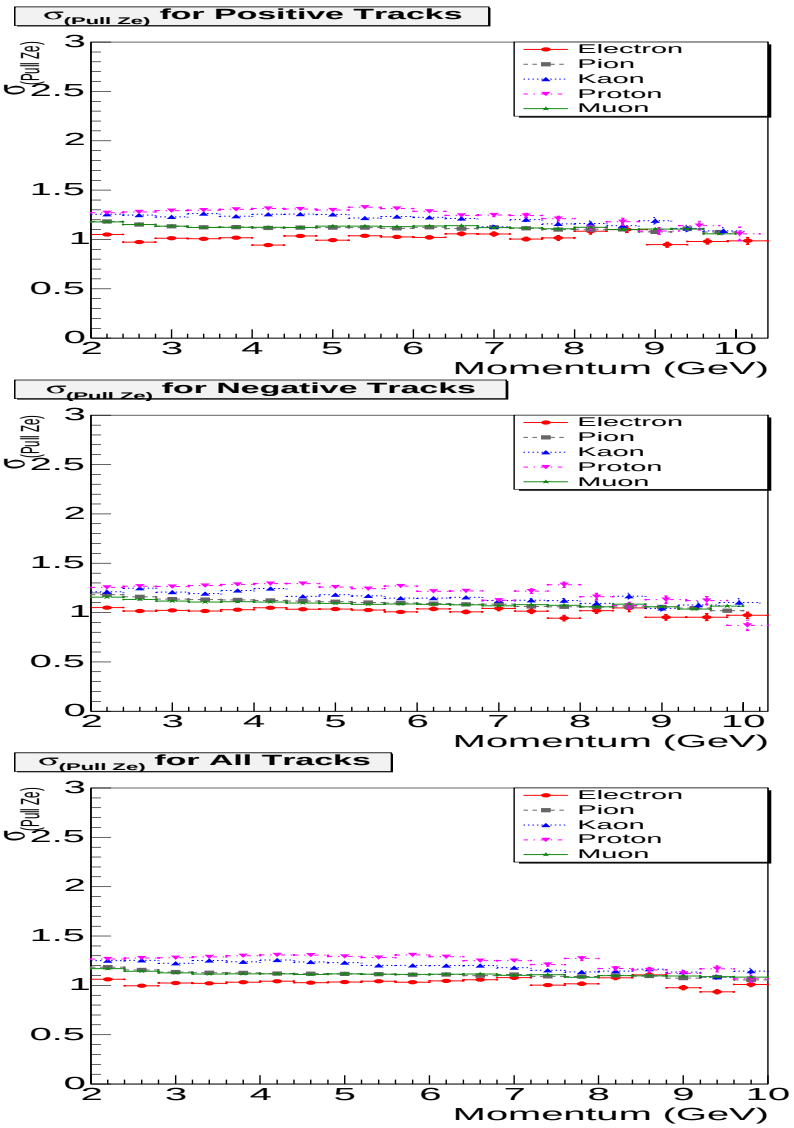

Figure 3.14: Distributions of the width of Z_e/σ_Z as function of track momentum for positive charged tracks (top), negative charged tracks (middle) and all charged tracks (bottom). Electrons are selected from photon conversion decay, kaons and pions are from $D^0 \to K^-\pi^+$, protons are from $\Lambda^0 \to p\pi$ and muons are from $J/\psi \to \mu^-\mu^+$ decays. Sideband subtractions were used to purify the track selections.

SUNGKYUNKWAN UNIVERSITY

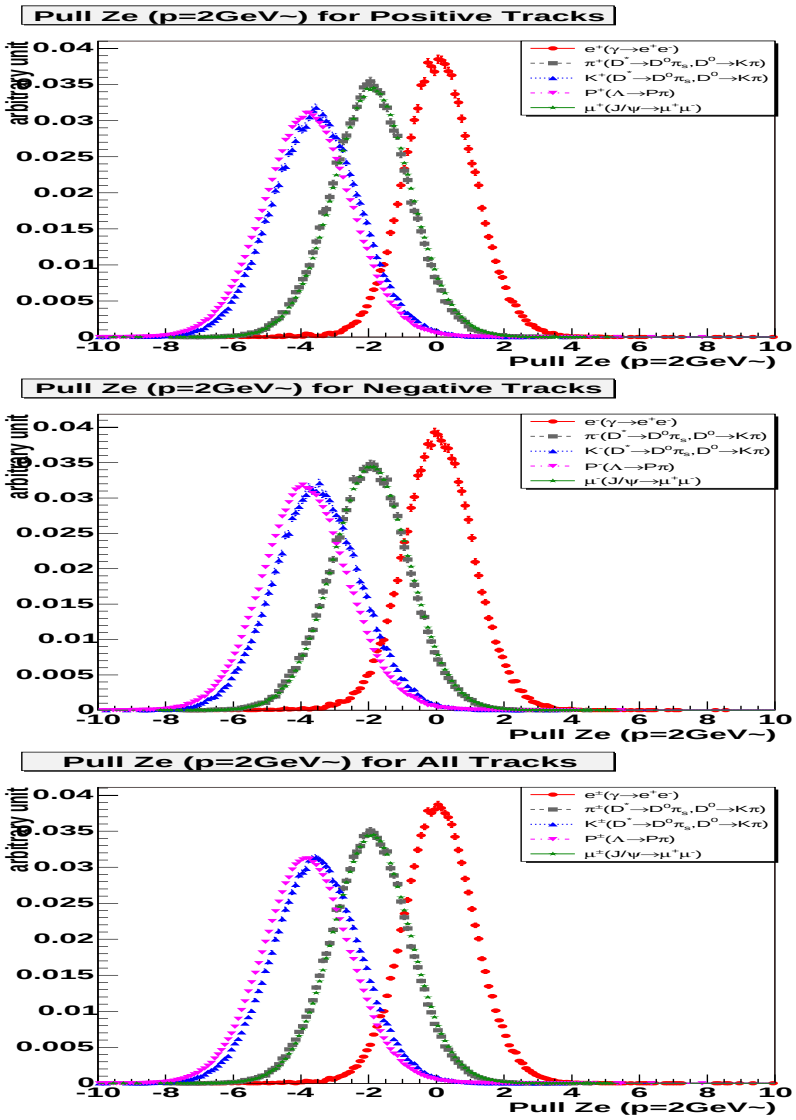

Figure 3.15: Distributions of the Z_e pull for positive charged tracks (top), negative charged tracks (middle) and all charged tracks (bottom).

SUNG KYUN KWAN UNIVERSITY

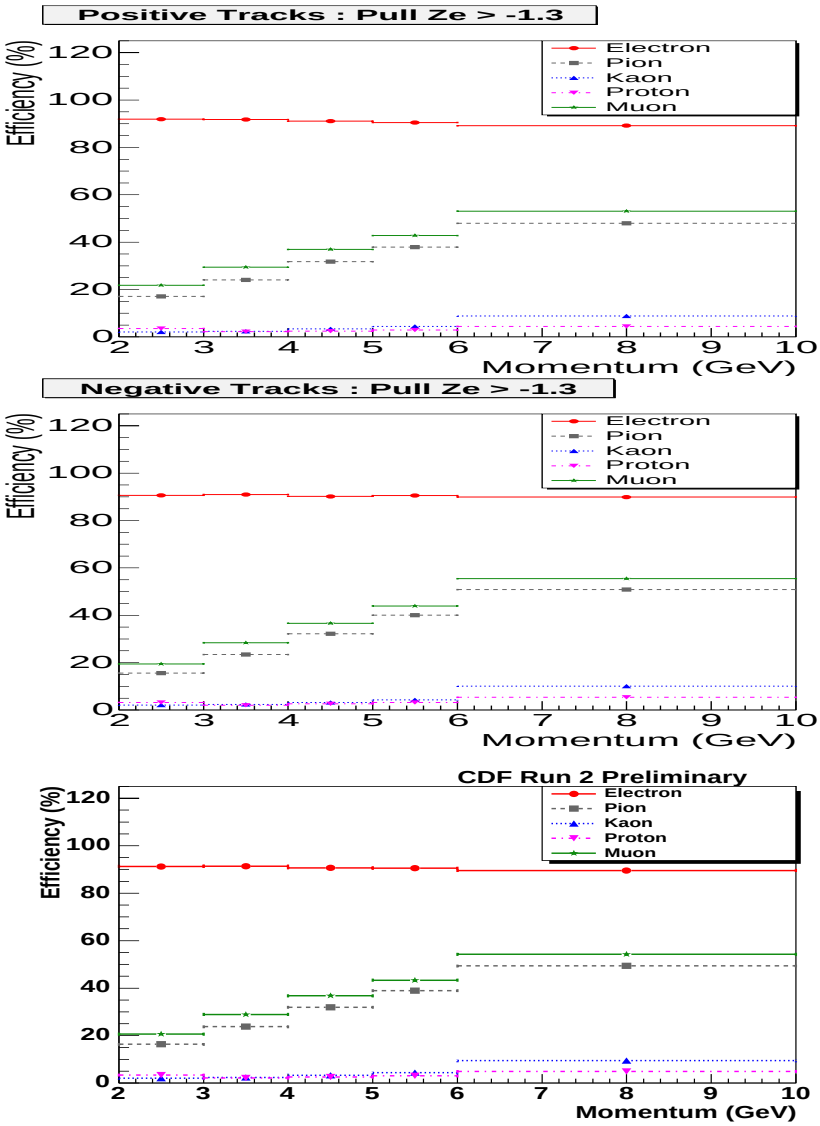

Figure 3.16: Efficiency of $Z_e/\sigma > -1.3$ cut as a function of track momentum for positive charged tracks (top), negative charged tracks (middle) and all charged tracks (bottom).

SUNGKYUNKWAN UNIVERSITY

3.5 J/ψ Reconstruction and Selection

J/ψ is reconstructed using decay $J/\psi \rightarrow \mu^+\mu^-$. In addition to the default reconstruction criteria for a "CdfMuon" collection [51], both muons are required to be CMU or CMX muons with a track-stub matching quality of $\chi^2(\Delta\phi) < 9$ between the positions measured using the muon chamber hits and that projected from the associated COT track. The minimum p_T requirement is 1.5 GeV for CMU muon and 2.0 GeV for CMX muon. To follow the J/ψ trigger path, we required that at least one of the muon in the pair as a CMU muon. The muons are required to satisfy the track selection criteria described earlier. To further reduce background, muons are also required to have at least 0.1 GeV energy deposited in hadronic calorimeter. This cut reduces about 16% background while keeping more than 97% good J/ψ.

The J/ψ vertex is formed from the intersection of the two muon tracks using the vertex fitting package *CTVMFT* with a C^{++} wrapper *VertexFit*. The χ^2 of the 3D vertex fitting is required to be less than 15. The momentum of the muon track is adjusted assuming its production point as in J/ψ vertex instead of the primary vertex. The combined p_T of the di-muon pair is required to be greater than 3 GeV/c. The invariant mass of the two muons is then calculated, as shown in Figire. 3.17, and the pairs with a mass within 50 MeV/c^2 of the PDG value 3.0969 GeV/c^2 are taken as the J/ψ candidates. The 50 MeV/c^2 window is about a 3σ wide. The RMS error σ is about 15 MeV/c^2 obtained from a simple Gaussian fit to the invariant mass. Di-muons within two 50 MeV/c^2 windows starting at 10σ away from the peak are used to estimate fake J/ψ background.

SUNGKYUNKWAN UNIVERSITY

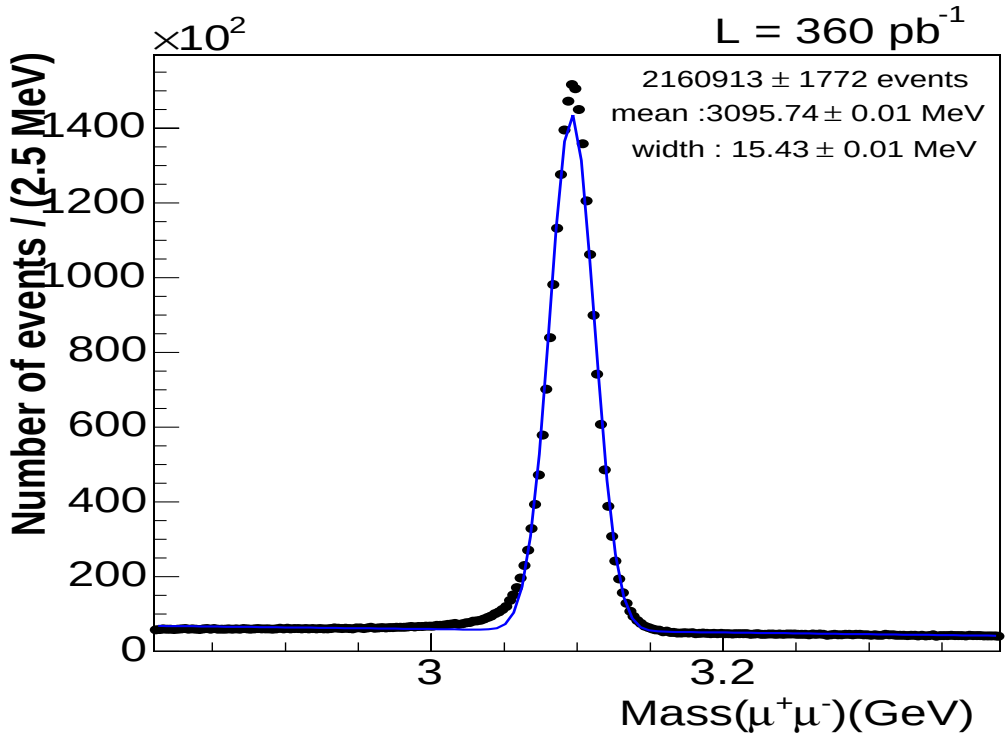

Figure 3.17: Distributions of di-muon invariant mass reconstructed from J/ψ sample. A simple Gaussian fit gives a mean of 3095.74 ± 0.01 MeV/c^2 with a width of 15.43 ± 0.01 MeV/c^2.

SUNGKYUNKWAN UNIVERSITY

3.6 Event selection for $J/\psi - e$ pair

The signature of $B_c \rightarrow J/\psi e\nu$ in CDF is the high p_T J/ψ-e pairs with a displaced decay vertex and with an invariant mass in the kinematic limits of $m_{J/\psi} < M_{J/\psi e} < m_{B_c}$. A Monte Carlo sample of $B_c \rightarrow J/\psi e\nu$ decay was produced using the "Bgenerator" package in the offline version 5.3.3. The B_c momentum spectrum in "Bgenerator" is from a theoretical calculation [29, 58]. The mass and lifetime of B_c in the generator are chosen to be 6.271 GeV/c and 0.55 ps. The p_T and the transverse opening angle $\Delta\phi$ (also called "azimuthal angle") distributions of J/ψ-e pair from B_c decay in the generator level before and after kinematic cuts on decay products, $p_T(\mu) > 1.5\ GeV/c$, $\mid \eta(\mu) \mid < 1.0$, $p_T(e) > 2.0\ GeV/c$ and $\mid \eta(e) \mid < 1.0$, are shown in Figire. 3.18 and Figire. 3.19. A cut of $p_T(J/\psi + e) > 5\ GeV/c$ is quite efficient to signal. For most of the pairs, the opening angle is less than 90 degree which will be served as an initial cut to reduce $b\bar{b}$ background, see section 4.3. The invariant mass $M_{J/\psi e}$ distribution with kinematic cut on muons, J/ψ and electrons are shown in Figire. 3.19. Most of events will be in the range of $4 < M_{J/\psi e} < 6$ which is defined as our search range for B_c signal. The increased lower bound from the 3 GeV kinematic limit on the invariant mass window is to reduce sensitivity to fake electron backgrounds from hadron and conversion decays and to other higher mass state feeding-downs.

Other selection criteria for J/ψ-e pair is developed based on the experiences of the topologically similar $B^+ \rightarrow J/\psi K^+$ reconstruction and generic B semileptonic decay reconstructions. The cuts are listed in Table 3.8. Events in a wider window (0-12GeV/c) of $J/\psi - e$ invariant mass window to study the shapes of background events and any mis-counting of additional backgrounds. Unlike fully reconstructed B events where mass resolution is a key to reduce background, the J/ψ mass constraint is not used for $B_c \rightarrow J/\psi e\nu$ event reconstruction. The mass constraint here does not contribute greatly to the improvement of J/ψ-e invariant mass resolution and we also need the sideband events on the di-muon pair to estimate fake J/ψ background. To reduce combinatorial background, we require a higher B vertex fitting quality. The

SUNGKYUNKWAN UNIVERSITY

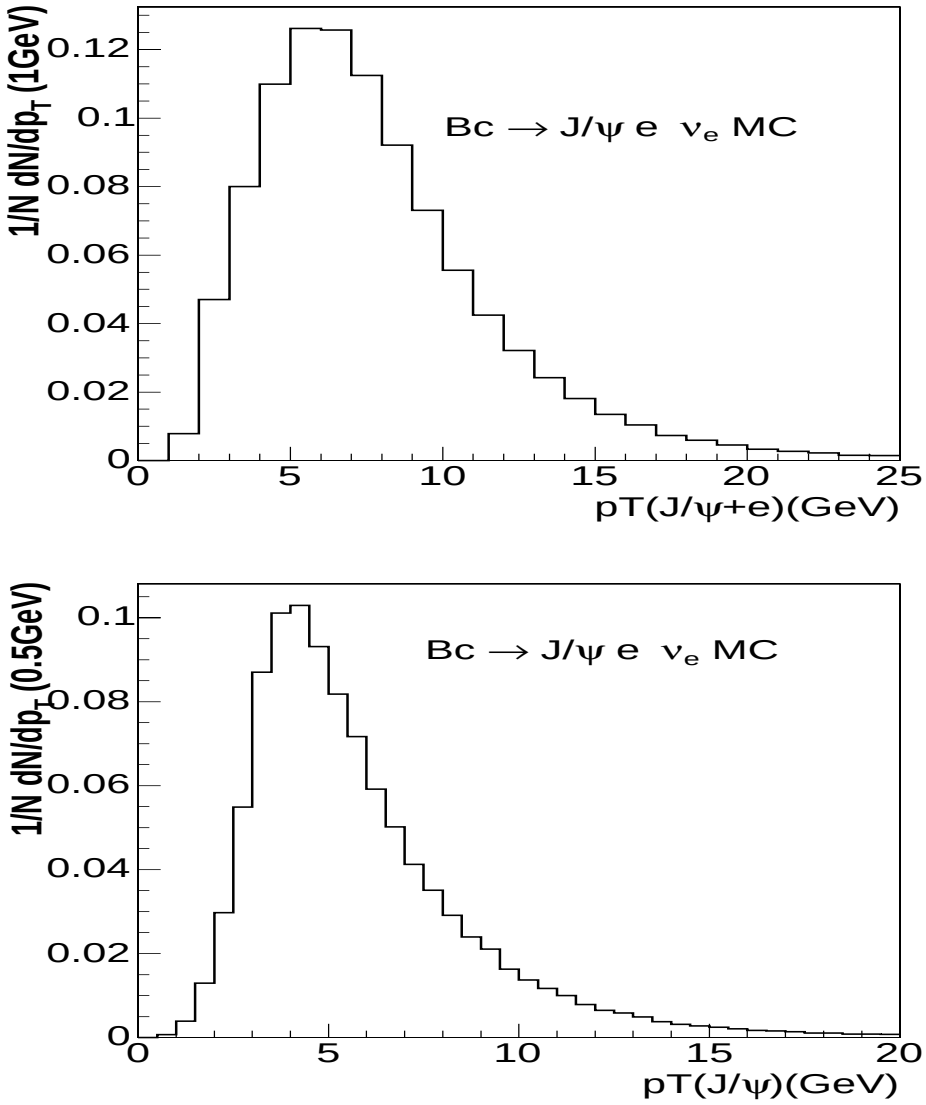

Figure 3.18: Generator level $p_T(J/\psi+e)$ (top) and $p_T(J/\psi)$ (bottom) distributions for events from $B_c \to J/\psi e\nu$ decay after application of kinematic cuts on the decay products of B_c, $p_T(\mu) > 1.5\,GeV/c$, $\mid \eta(\mu) \mid < 1.0$, $p_T(e) > 2.0\,GeV/c$ and $\mid \eta(e) \mid < 1.0$.

SUNGKYUNKWAN UNIVERSITY

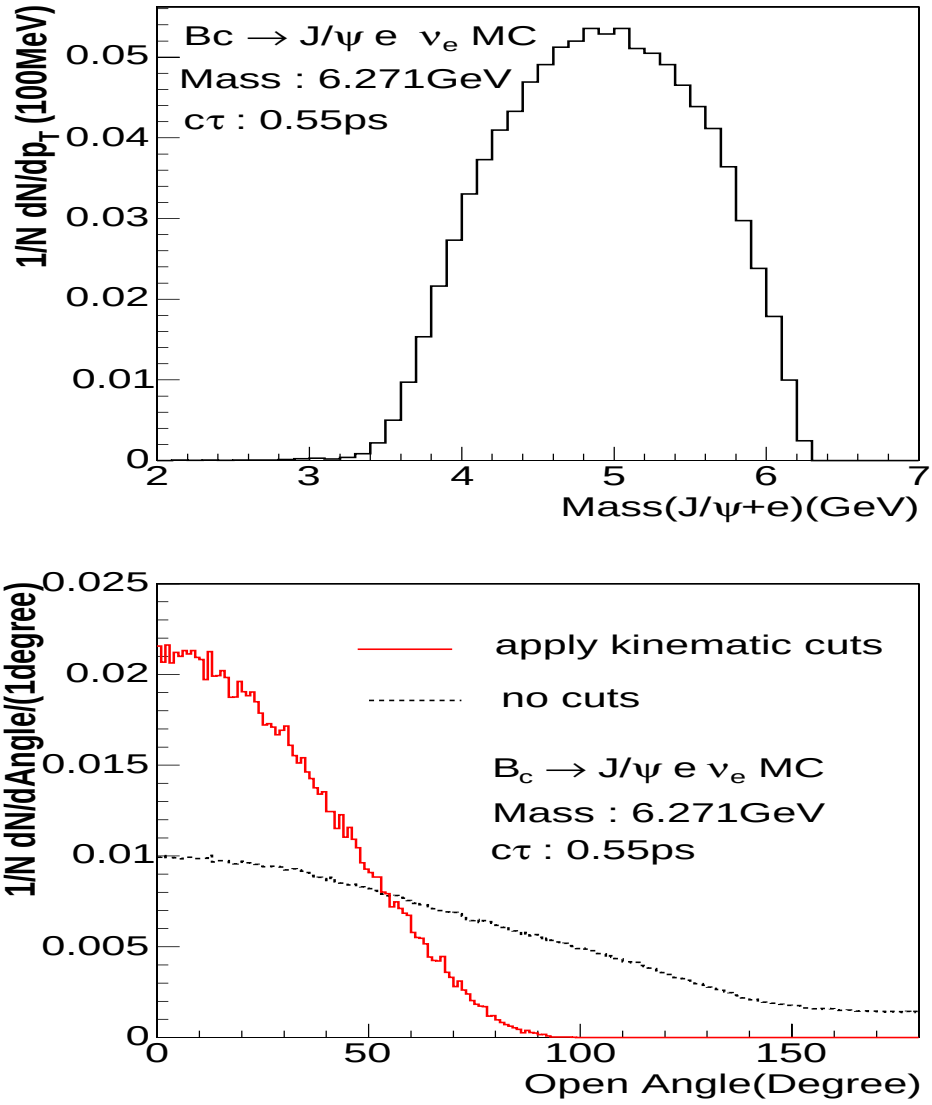

Figure 3.19: Generator level distributions of invariant mass and opening angle of the J/ψ-e pairs for events from $B_c \rightarrow J/\psi e\nu$ decay after application of kinematic cuts on the decay products of B_c,$p_T(\mu) > 1.5\ GeV/c$, $\mid \eta(\mu) \mid < 1.0$, $p_T(e) > 2.0\ GeV/c$ and $\mid \eta(e) \mid < 1.0$.

SUNGKYUNKWAN UNIVERSITY

B_c candidates is required to have a displaced vertex which is 3σ away from primary vertex to reduce background from prompt J/ψ.

Table 3.8: Event selections for $B_c \to J/\psi eX$ events.

Cut description	Value
CMU track-stub match	$\chi^2(r\phi) < 9$
CMX track-stub match	$\chi^2(r\phi) < 9$
Hadron energy for muons	$E_{had} > 0.1$ GeV
Di-muon vertex fitting	$\chi^2(3D) < 15$
Di-muon mass window for J/ψ peak	$\mid M(\mu\mu) - 3.09687\ GeV \mid < 50\ MeV$
Di-muon mass window for J/ψ sidebands	$\mid M(\mu\mu) - 3.09687 \pm 10 * 0.015\ GeV \mid < 50\ MeV$
p_T of J/ψ	$p_T(J/\psi) > 3$ GeV
p_T of electron	$p_T(e) > 2$ GeV
electron fiducial	$\mid \eta \mid < 1.0$
dE/dx hits numbers	nhits ≥ 43
dE/dx	$Z_e/\sigma > -1.3$
Likelihood-based eID	$P_e < 0.7$
p_T of J/ψ and e	$p_T(J/\psi + e) > 5$ GeV
$B^+ \to J/\psi K^+$ veto	$\mid M(J\psi + K) - 5.2789\ GeV \mid > 50 MeV$
B vertex quality	$prob(\chi^2_{3d}/1.5, dof) > 0.1\%$
B lifetime	$L_{xy}/\sigma_{L_{xy}} > 3$

3.7 Selection of $B^+ \to J/\psi K^+$ events

We follow closely the B lifetime measurement analysis [59] to select $B^+ \to J/\psi K^+$ as our normalization channel for cross section analysis. The selection cuts are listed in Table 3.9. As a normalization mode to the $B_c \to J/\psi e\nu$, we add the requirement that the kaon track to be in the CEM fiducial. B vertex and lifetime cuts were also modified to be in line to that of B_c selection.

We found 2850 ± 60 signal events using cuts listed in Table 3.9, as shown in Figire. 3.20. To compare yield with other analysis, we release the CEM

SUNG KYUN KWAN UNIVERSITY

Table 3.9: Event selections for $B^+ \to J/\psi K^+$ events.

Cut description	Value
CMU track-stub match	$\chi^2(r\phi) < 9$
CMX track-stub match	$\chi^2(r\phi) < 9$
Hadron energy for muons	$E_{had} > 0.1$ GeV
Di-muon vertex fitting	$\chi^2(3D) < 15$
Di-muon mass window	$\mid M(\mu\mu) - 3.09687\ GeV \mid < 50\ MeV$
J/ψ mass constraint to PDG value	3.09687 GeV
p_T of J/ψ	$p_T(J/\psi) > 3$ GeV
p_T of kaon	$p_T(K) > 2$ GeV
Kaon fiducial	in CEM
p_T of B	$p_T(B^+) > 5$ GeV
B vertex quality	$prob(\chi^2_{3d}/1.5, dof) > 0.1\%$
B lifetime	$L_{xy}/\sigma_{L_{xy}} > 3$

fiducial requirement for kaon and found 3581 ± 66 signal events as shown in Figire. 3.20. To check any effect on B^+ yield from J/ψ mass constraint, we also released the J/ψ mass constraint during reconstruction and found a consistent yield of 3554 ± 65.

SUNG KYUN KWAN UNIVERSITY

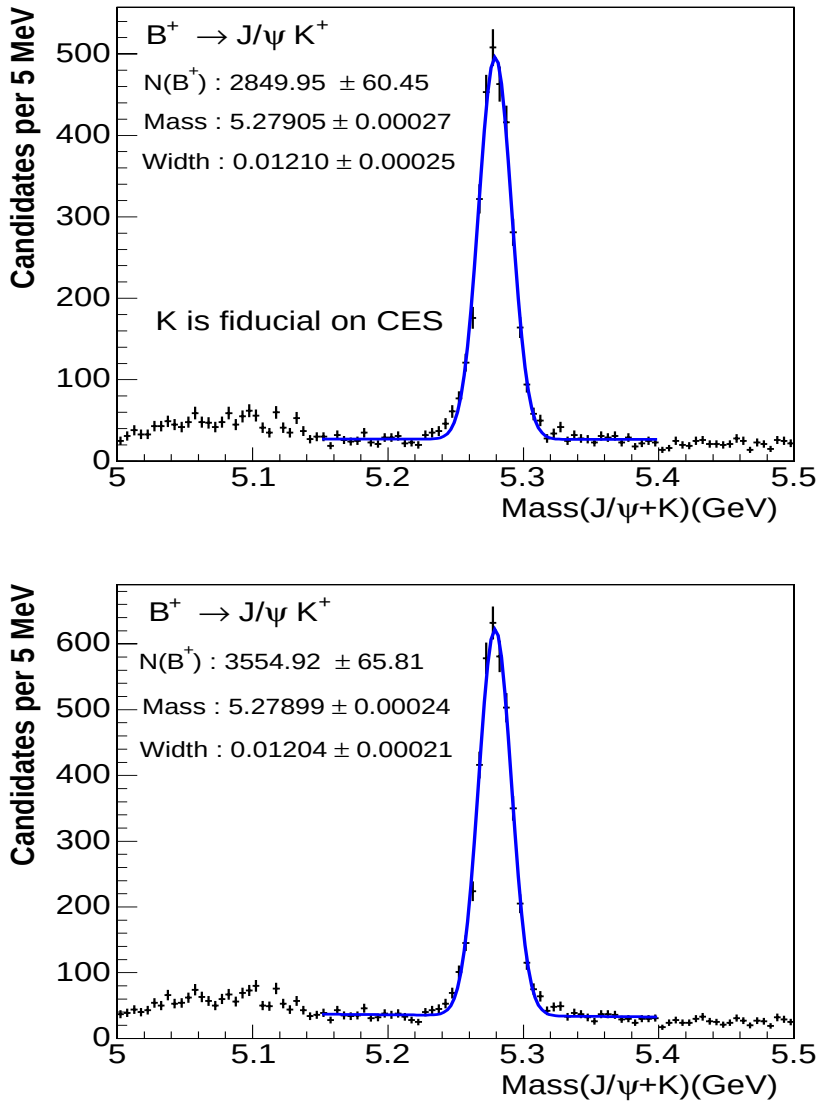

Figure 3.20: B^+ invariant mass distribution. Top plot is produced using cuts in Table 3.9. 3554 ± 65 signals is found from a fit to the distribution. Bottom plot is produced using cut in Table 3.9 but without CEM fiducial requirement for the kaons. 2845 ± 60 events from fits to the distributions.

SUNG KYUN KWAN UNIVERSITY

Chapter 4

Background determination

In this chapter we discuss all possible source of backgrounds and its contamination to B_c signal.

4.1 Fake electron background

The fake electron background is estimated using the $J/\psi + track$ data sample. The event selections are similar to that for $J/\psi + e$ but there is no requirement for the track to be identified as an electron. The J/ψ-track invariant mass distribution is shown in Fig 4.1.

As discussed in early section that the hadron faking electron rate is different for pion, kaon and proton particles. To properly estimate the fake electron background, we calculate the averaged fake rate after taking into account the probabilities for a track to be from a pion, kaon or proton particle. We obtained this information using Pythia Monte Carlo. A generic J/ψ sample from B decays were produced using the Pythia setting "msel=1" with "tunning-A" for underline events . We analyzed the Monte Carlo sample in the same way as for the $J/\psi + track$ data to find the track candidates around the J/ψ. The track's particle-type were found by matching the reconstructed with the Monte Carlo truth information in generator level. Distributions of particle-type being kaon, pion and proton were then calculated. The dE/dx cut was

SUNGKYUNKWAN UNIVERSITY

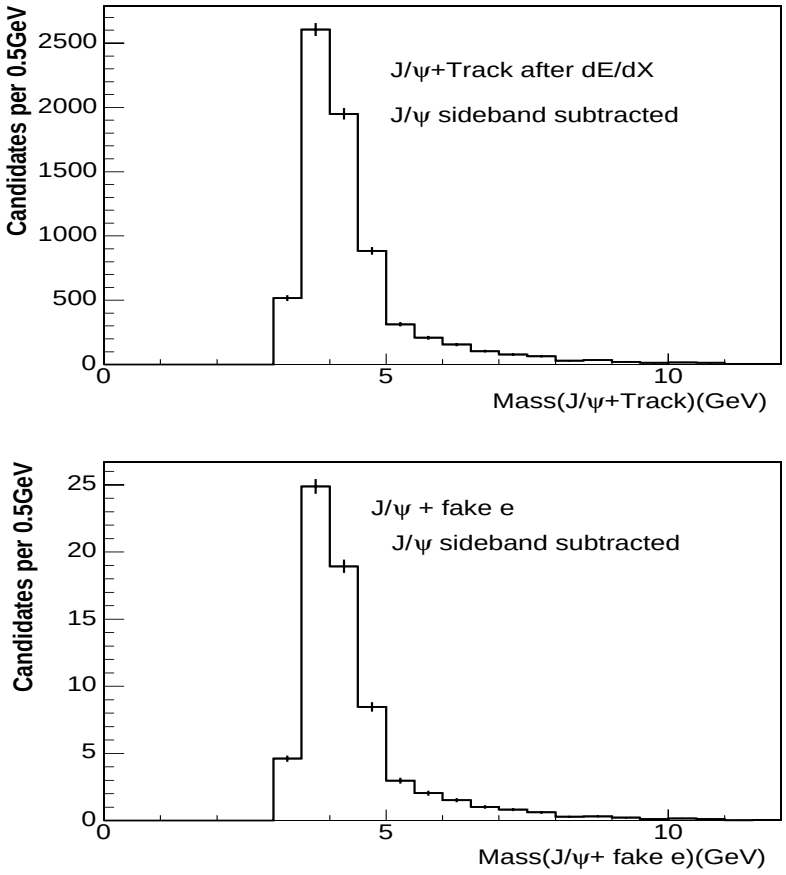

Figure 4.1: Invariant mass distribution of J/ψ-track pair. Top plot is for events passed all selection listed in Table 3.8 including dE/dx $Z_e/\sigma > -1.3$ but without the electron identification. Bottom plot is after an event-by-event correction of electron fake rate for the standard electron identification. Fake J/ψ contributions for both plots are excluded with mass sideband subtractions.

not used for Monte Carlo track and dE/dx efficiencies listed in Table 3.7 were used to corrected the original particle-type distribution. In Table 4.1 and 4.2 the fractions of particle-type for a track with different p_T are listed.

With the particle-type fractions in Table 4.2, the fake rate results for the kaon, pion and proton as listed in Table 3.4,3.5 and 3.6 were re-weighted to get the average hadron faking electron rates for a track around J/ψ for the electron

SUNGKYUNKWAN UNIVERSITY

Table 4.1: Fraction of particle-type for tracks around J/ψ before dE/dx cut.

p_T GeV/c	kaon	pion	proton
2-3	0.393 ± 0.002	0.559 ± 0.003	0.0477 ± 0.0007
3-4	0.478 ± 0.004	0.491 ± 0.004	0.0312 ± 0.0009
4-5	0.533 ± 0.007	0.445 ± 0.006	0.0218 ± 0.0011
5-6	0.570 ± 0.011	0.412 ± 0.008	0.0176 ± 0.0015
> 6	0.653 ± 0.011	0.361 ± 0.008	0.0157 ± 0.0014

Table 4.2: Fraction of particle-type for tracks around J/ψ after dE/dx cut.

p_T GeV/c	kaon	pion	proton
2-3	0.081 ± 0.003	0.903 ± 0.012	0.0159 ± 0.0012
3-4	0.088 ± 0.004	0.907 ± 0.018	0.0052 ± 0.0010
4-5	0.109 ± 0.007	0.887 ± 0.024	0.0035 ± 0.0011
5-6	0.134 ± 0.010	0.864 ± 0.033	0.0029 ± 0.0014
> 6	0.248 ± 0.013	0.749 ± 0.026	0.0032 ± 0.0013

SUNGKYUNKWAN UNIVERSITY

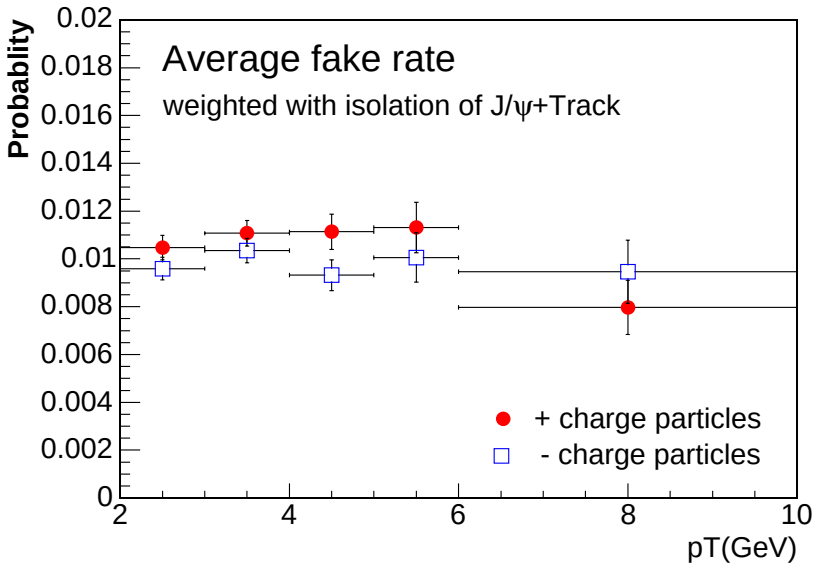

Figure 4.2: The averaged hadron faking electron probabilities as function of track p_T.

identifications are calculated and shown in Fig 4.2. The numeric values are listed in Table 4.3.

Table 4.3: Averaged hadron faking electron probabilities (%) as function of track p_T. There is no isolation correction on fake rates for pions, kaons and protons during the averaging process. This table will be used for systematic error studies.

p_T (GeV/c)	No isolation weighting		With isolation weighting	
	+ charge	- charged	+ charged	- charged
2-3	1.048 ± 0.051	0.959 ± 0.047	1.16 ± 0.03	1.02 ± 0.03
3-4	1.108 ± 0.053	1.035 ± 0.051	1.19 ± 0.04	1.08 ± 0.04
4-5	1.114 ± 0.074	0.932 ± 0.064	1.18 ± 0.06	0.95 ± 0.06
5-6	1.131 ± 0.105	1.006 ± 0.103	1.19 ± 0.09	1.04 ± 0.09
> 6	0.797 ± 0.114	0.946 ± 0.131	0.98 ± 0.10	1.13 ± 0.13

The $J/\psi + track$ candidates are multiplied by the averaged hadron faking

SUNGKYUNKWAN UNIVERSITY

electron probabilities to obtain the contributions of a fake electron combined with a real J/ψ. The invariant mass distribution for this background is shown in Fig. 4.1 and the numerical values are tabulated in Table 5.3. Systematic error on the fake electron background estimation comes from several sources, fake rate dependence on the electron's isolation environment, uncertainty from track's particle type, and SVT-track bias.

We found the $D^0 \to K\pi$ events selected using 2-track trigger tends to have a more isolated tracks comparing to the J/ψ events as shown in Fig. 3.12. We corrected the difference by making the isolation distribution in $D^0 \to K\pi$ similar to that as in J/ψ using an event-by-event weighting method during the fake rate calculation. The differences on fake rates before and after re-weighting was found to be about 15% for the likelihood-based electron reconstruction, as shown in Table 4.3. We used the weighted fake rate during our estimation of background contribution but took the differences of using the non-weighted fake rate as systematic errors. We found the change on number of fake electron background in the signal window of $4 < M(J/\psi + e) < 6$ GeV is 1.96 events.

Another source of systematic uncertainty on the fake rate is the potential bias from trigger difference. The D^0 sample used for the fake rate measurement is from 2-track SVT triggered sample which has a much tighter requirement on the silicon hits requirement than the tracks around J/ψ. The SVT track requires at least 4 silicon hits attached to it. The distributions of number of silicon hits attached to the tracks in the J/ψ events and from $D^0 \to K\pi$ are shown in Fig. 4.3. As one can see, the fraction of tracks with less than 4 hits in the J/ψ sample is much bigger than that from $D^0 \to K\pi$ sample. We first look the fake rate difference for tracks with less than 4 hits and the ones with at least 4 hits. The $K_s \to \pi^+\pi^-$ decay reconstructed in the J/ψ sample was used for this study. Due to limited statistics, the fake rate for tracks with different number of silicon hits were calculated only as p_T integrated result. The calculated fake rate for positively and negatively charged pion tracks with different number of silicon hits attached are listed in Table 4.4. Using silicon hits in J/ψ+track sample as the weighting factors, the new averaged fake rates were calculated and found to be different from that obtained directly from 2-

SUNG KYUN KWAN UNIVERSITY

track triggered sample by about 7%. We took these variation and assign the systematic error on background from fake electron due to SVT bias as 1.11 events.

The electron fake rates from pion, kaon and protons are very different. We need the fractions of tracks being pion, kaon and proton in order to properly calculate the averaged fake rate. We compared these fractions predicted from Monte Carlo and obtained from fitting data using COT dE/dx values. The COT dE/dx distribution for kaon and proton particles are similar thus we were only able to separate pions from kaon and protons. So we fitted the track used in the J/ψ+track sample to obtain the pion fraction. First we compare the dE/dx Z_e/σ_Z distributions obtained directly from data in J/ψ+track and to the weight-averaged distribution using predicted particle-type fraction in Table 4.2 and dE/dx shapes for pion, kaon and proton tracks obtained in the dE/dx calibration process. These distributions of the measured and predicted are in good agreement, as shown in Fig. 4.4. Then we obtain the pion fraction from data as shown in Fig. 4.5. The shape of the Z_e/σ_Z for pion and kaon are assumed to be a Gaussian function. We also combine the contribution of proton to the kaon since it has very similar distribution as kaon. We simply calculate the pion fraction. We found the pion fraction from the fitting is within 3% of that predicted from Monte Carlo, as shown in Fig. 4.6 and tabulated in Table 4.5. We took the difference and re-calculated the averaged fake rate and fake background contribution. We found a systematic error of 0.53 events.

We also checked the fake electron prediction by comparing it to that from a dE/dx fitting on the J/ψ+e sample. The electron track's dE/dx distribution was fitted using expected shapes for electrons, pion, kaon and protons and the fraction of electron and hadrons were extracted for events in $3 < M(J/\psi+e) <$ 12 GeV/c^2 and in $4 < M(J/\psi + e) < 6$ GeV/c^2, as shown in Fig. 4.7. The electron and hadron contributions obtained are 281 ± 9 (electron) and 31 ± 5 (hadron) for all mass window and 167 ± 7 (electron), 9 ± 3 (hadron) which in good agreement with the prediction from fake rate as listed in Table 5.3. No systematic error is to be assigned from this study.

The total systematic error on the fake electron background in the $4 <$

SUNGKYUNKWAN UNIVERSITY

$M(J/\psi + e) < 6$ GeV window is found to be 3.00 events.

Table 4.4: Fake rate (%) for track with $p_T > 2$ GeV/c with different silicon hit requirements. The weighted averages were done using silicon distributions in J/ψ sample. $K_s \to \pi^+\pi^-$ events from J/ψ sample were used for this study.

Type	nSiHits = 3	nSiHits ≥ 4	Weight average	From TTT
π^+	1.006 ± 0.063	1.149 ± 0.031	1.133 ± 0.028	1.135 ± 0.030
π^-	1.013 ± 0.056	1.099 ± 0.0026	1.089 ± 0.024	1.066 ± 0.025

Table 4.5: Pion fraction from dE/dx fitting and from Pythia MC prediction

p_T (GeV)	dE/dx fitting	MC prediction
2.0 - 3.0	0.5762 ± 0.0075	0.5591 ± 0.0028
3.0 - 4.0	0.537 ± 0.012	0.4905 ± 0.0042
4.0 – 5.0	0.502 ± 0.019	0.4449 ± 0.0061
5.0 – 6.0	0.483 ± 0.027	0.4125 ± 0.0085
> 6.0	0.441 ± 0.033	0.3612 ± 0.0078

SUNGKYUNKWAN UNIVERSITY

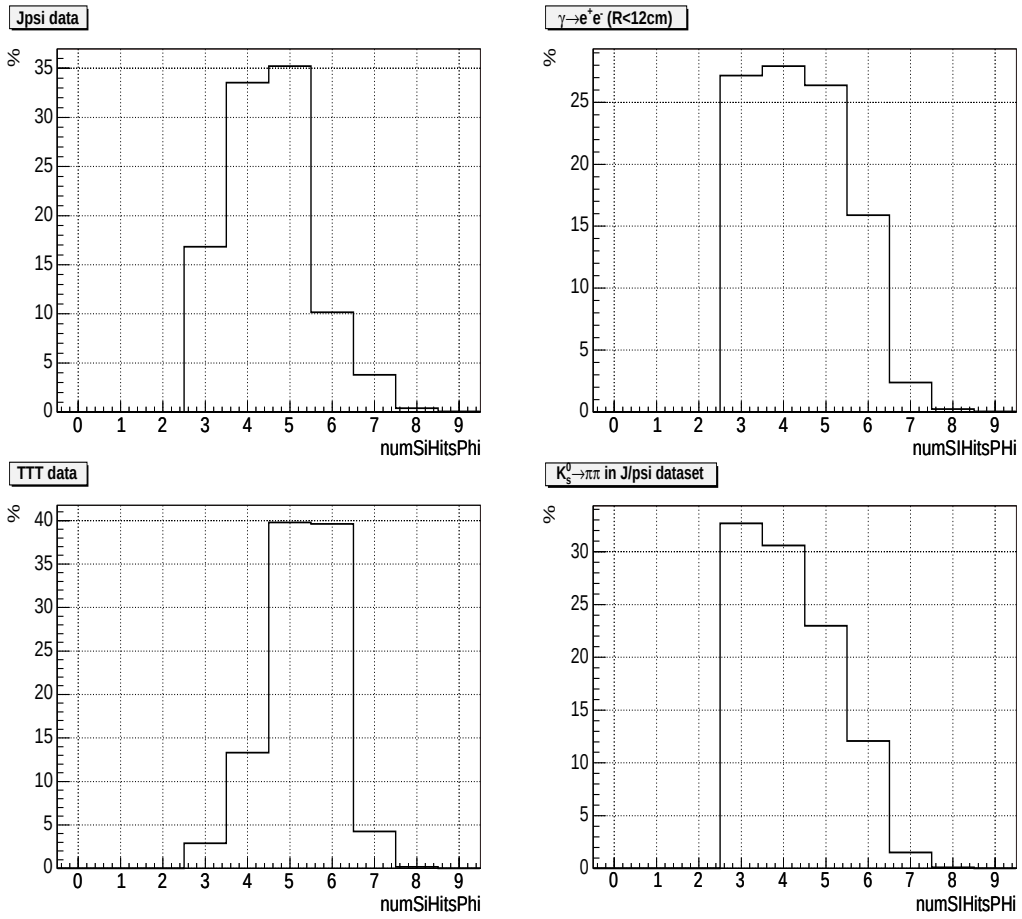

Figure 4.3: Distribution of number of silicon hits for tracks from J/ψ+track sample, electrons from photon conversion sample, from D^0 from two-track-trigger sample and from K_s reconstructed in J/ψ sample.

SUNG KYUN KWAN UNIVERSITY

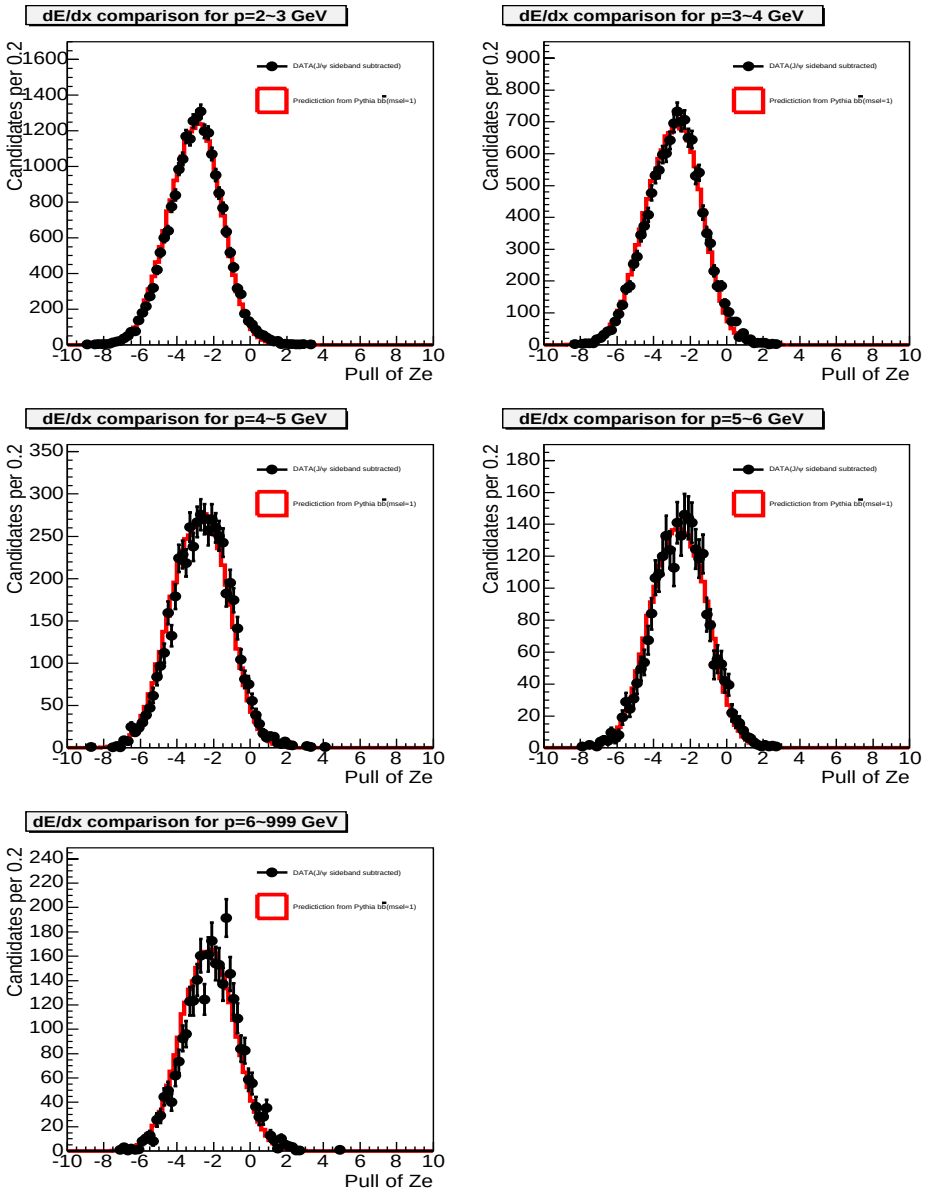

Figure 4.4: dE/dx comparisons between direct measurements from J/ψ+track events and the combined distributions using individual shapes of pion,kaon and proton tracks weight-averaged using particle-type fractions predicted from Pythia Monte Carlo.

SUNGKYUNKWAN UNIVERSITY

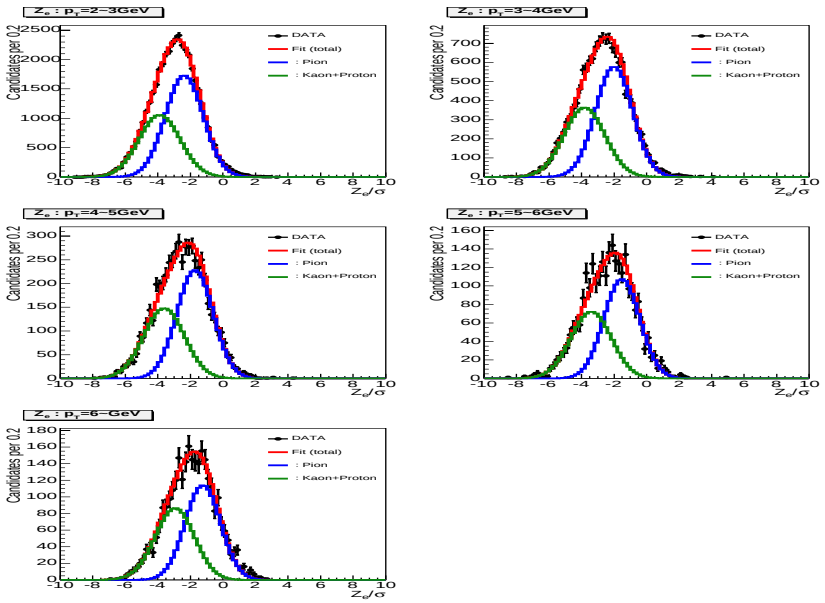

Figure 4.5: Pion fractions for the tracks in the J/ψ+track sample. Black dots are from data and red histograms are from dE/dx fitting result. Blue and green histograms are pion and kaon+proton components of the fitting result.

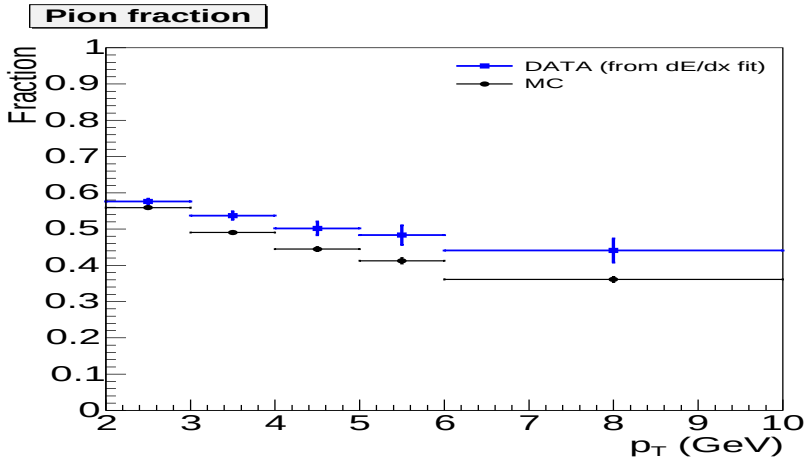

Figure 4.6: Comparison of pion fraction results for the tracks in the J/ψ+track sample. Blue squares are from dE/dx fitting result and black dots are from MC prediction.

SUNGKYUNKWAN UNIVERSITY

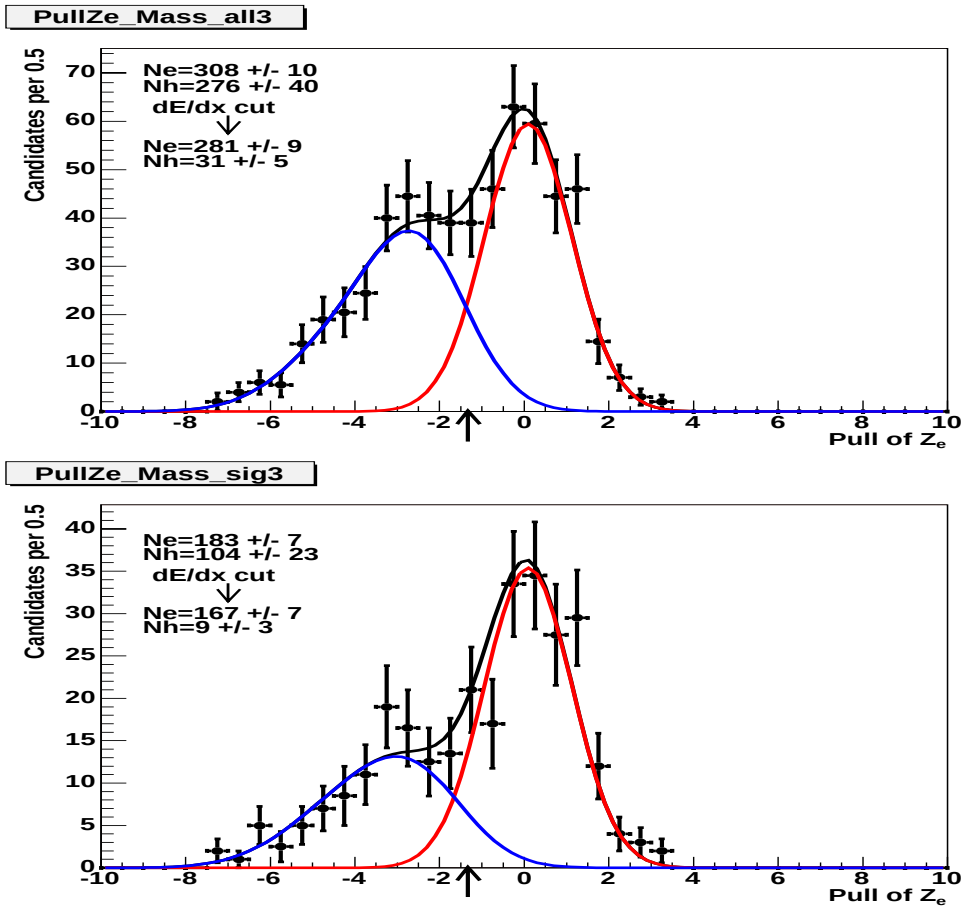

Figure 4.7: The dE/dx fitting results of electron and hadron contributions in the J/ψ+e sample for all events in $3 < M(J/\psi + e) < 12$ GeV/c^2 (top) and $4 < M(J/\psi + e) < 6$ GeV/c^2 window. Number of events before and after cuts $Z_e/\sigma_Z > -1.3$ were given. Fake J/ψ contributions were removed using standard sideband subtraction methods.

SUNGKYUNKWAN UNIVERSITY

4.2 Residual conversion electron background

During the selection J/ψ+e sample, electrons identified as from photon conversion is excluded. The photon conversion process starts with combining the identified electron with a partner track with an opposite charge to form a common vertex using algorithm described in reference [60]. The conversion electron is identified as these satisfying $|\Delta \cot \Theta| < 0.05$ and $-0.3cm < d_{XY} < 0.5\ cm$ after combining it with a partner track which has a minimum p_T of 400 MeV/c. We calculated the efficiency of the conversion finding using Monte Carlo simulation and estimated the contribution from residual conversion electron to the B_c events from data together with the conversion finding efficiency.

The conversion finding efficiency used here is defined as the probability to find a partner track satisfying the conversion selection for the identified electrons. The partner track is not required to be identified as an electron using CDF detector. We estimated this efficiency using Monte Carlo samples. Two set of events are generated for the studies. The primary method is to follow the p_T spectrum of $B^0 \to J/\psi K^+$ to generate a decay chain $B^0 \to J/\psi\pi^0$, $\pi^0 \to \gamma\gamma$ (98%) with one leg decaying to a electron pair $\gamma \to e^+e^-$, or $\pi^0 \to \gamma e^+e^-$ (2%). The 2nd method is to force the π^0 particle have a p_T spectrum the same as that for the track found in the J/ψ+track sample. The π^0 then decays as method one. The 2nd method generates a conversion electron sample with a softer p_T spectrum thus a lower reconstruction efficiency. The conversion-finding efficiencies as function of electron p_T estimated are plotted in Fig.4.8 and tabulated in Table 4.6. The residual conversion rate relative to the identified one is simply

$$N_{resid} = N_{conv} \times \frac{1 - \epsilon_{conv}}{\epsilon_{conv}}, \tag{4.1}$$

where N_{resid} is the number of residual electron from photon conversion (photon conversion electron not found due to kinematic coverage), N_{conv} is the number of conversion electron identified, and ϵ_{conv} is the conversion electron finding efficiency.

We analyzed the J/ψ data using the cut as listed in Table 3.8 and identify the J/ψ - conversion electron pairs with variables of $|\Delta \cot \Theta| < 0.05$ and

SUNGKYUNKWAN UNIVERSITY

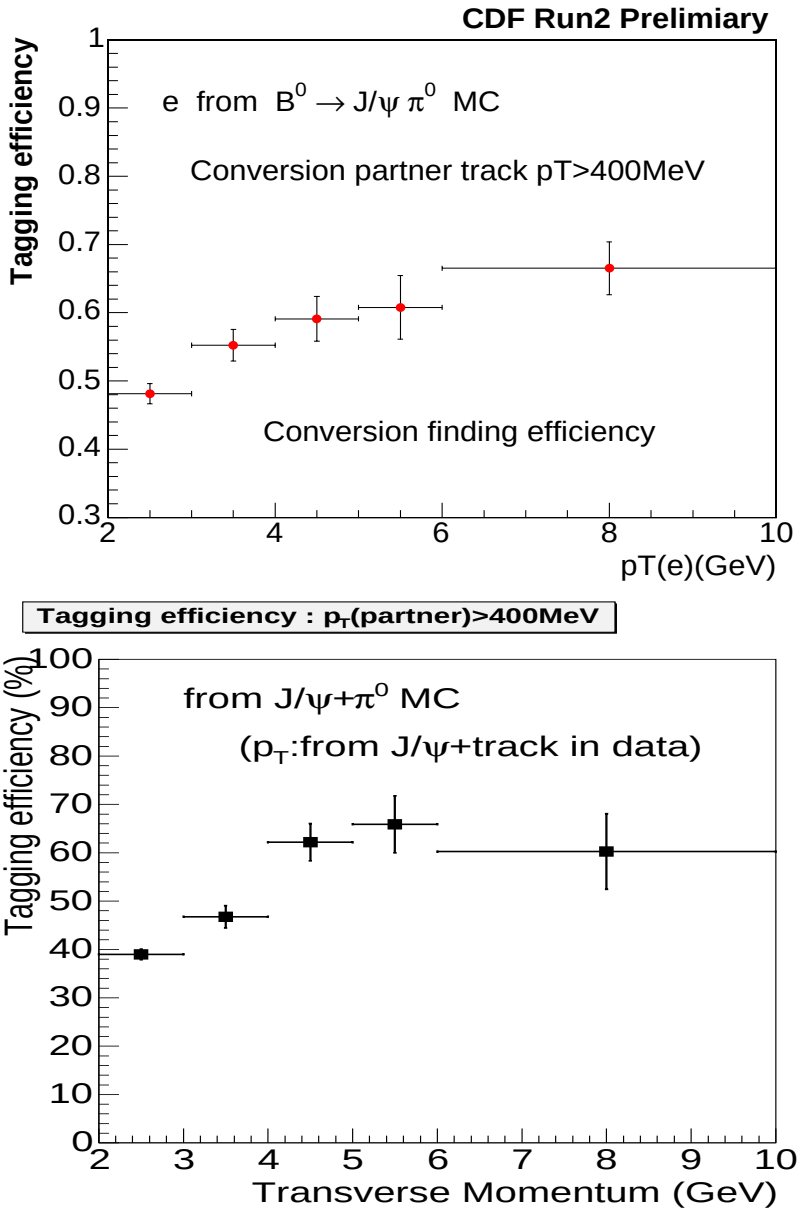

Figure 4.8: Conversion finding efficiency estimated using Monte Carlo samples. Top plot shows the result using decay chain $B^0 \to J/\psi\pi^0, \pi^0 \to \gamma\gamma$ and $\gamma \to e^+e^-$. The bottom plot shows the result using π^0 with same p_T spectrum as in J/ψ+track data sample.

SUNGKYUNKWAN UNIVERSITY

Table 4.6: Residual find efficiency (%) estimated using MC sample generated with decay chain $B^0 \to J/\psi\pi^0, \pi^0 \to \gamma\gamma$ with $\gamma \to e^+e^-$ (98%) and $\pi^0 \to \gamma e^+e^-$ (2%) (Method 1) and MC sample of π^0 with same p_T spectrum as in J/ψ+track data (Method 2).

p_T (GeV/c)	Method 1	Method 2
2-3	49.8 ± 1.4	39.0 ± 1.1
3-4	55.0 ± 2.2	46.8 ± 2.3
4-5	56.5 ± 3.3	62.2 ± 3.8
5-6	61.5 ± 4.5	65.9 ± 5.9
> 6	69.2 ± 3.4	60.3 ± 7.8

$-0.3cm < d_{XY} < 0.5cm$. We then made an event-by-event correction using equation 4.1 to obtain the invariant mass distribution of the J/ψ-residual conversion electron pairs shown in Fig.4.9 and tabulated in Table 5.3.

Following sources of systematic error on residual electron background were studied. The p_T spectrum of the electron and its partner track have big impact on the efficiency estimation. We estimated the effect by comparing the conversion-finding efficiency between using $B^0 \to J/\psi\pi^0$ Monte Carlo sample to that from forcing π^0 p_T spectrum as that of the track in the J/ψ+track sample. As shown in Table 4.6, the efficiencies different by about 13% to 22% in the p_T bins which translates to a difference of 4.88 events.

Another source of systematic error considered is the make-up of the residual conversion of pure conversion from $\pi^0 \to \gamma\gamma$ with $\gamma \to e^+e^-$ and the Dalitz decay of $\pi^0 \to \gamma e^+e^-$. The dalitz-electron finding efficiency is found to be 5% lower than that of pure conversion electron. The fraction of electrons from these two sources changed after the detector simulation from 98%:2% to about 87%:13%. We take the change as an 100% uncertainty and vary the fractions from 97%:3% to 77%:23%. The change of averaged conversion-finding efficiency is found differ by about 1% which translates to the number of residual events of 0.15 events.

We also checked the efficiency dependence on the lifetime of the origin

SUNGKYUNKWAN UNIVERSITY

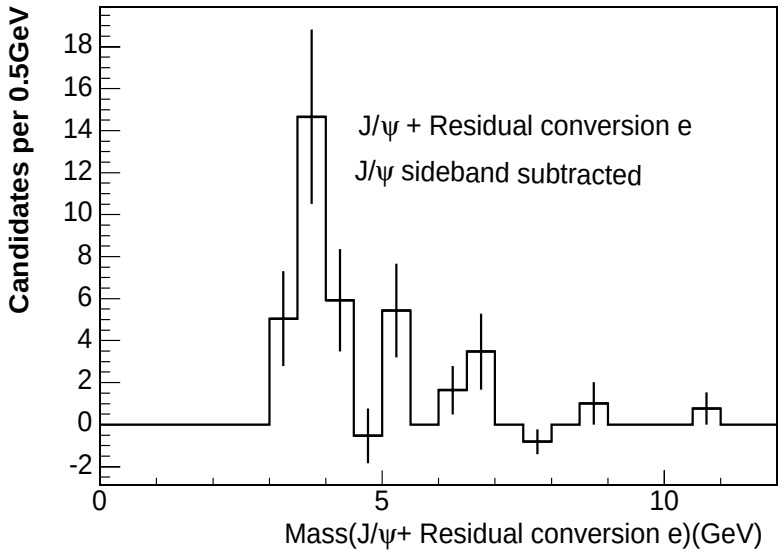

Figure 4.9: Invariant mass distribution of J/ψ-residual conversion electron pair for the likelihood-based electron identification.

where the conversion electron is produced. We reset the lifetime of B^0 to be zero for the Monte Carlo simulation and calculate the efficiency using this sample. We found the efficiency differences to be less than 1% which translates to the background events of 0.39 events.

Finally, we re-did the efficiency and background estimation using different p_T threshold cut as 300MeV and 500MeV instead of the default value of 400MeV for the partner track. The efficiency for different partner p_T threshold is listed in Table 4.7 and the number of background events estimated are tabulated in Table 4.8. We found consistent results from these estimations and assign no systematic uncertainty for this.

In summary, the total systematic error on the residual conversion background in the $4 < M(J/\psi + e) < 6$ GeV window is found to be 5.26 events.

SUNG KYUN KWAN UNIVERSITY

Table 4.7: Residual find efficiency (%) for different partner p_T threshold estimated using MC sample generated with decay chain $B^0 \to J/\psi\pi^0, \pi^0 \to \gamma\gamma$ with $\gamma \to e^+e^-$ (98%) and $\pi^0 \to \gamma e^+e^-$ (2%).

p_T (GeV/c)	p_T>300MeV	p_T>400MeV	p_Ty>500MeV
2-3	54.0 ± 1.3	49.8 ± 1.4	45.7 ± 1.4
3-4	59.0 ± 2.1	55.0 ± 2.2	50.7 ± 2.3
4-5	59.9 ± 3.1	56.5 ± 3.3	52.8 ± 3.4
5-6	64.6 ± 4.3	61.5 ± 4.5	57.8 ± 4.7
> 6	75.4 ± 3.0	69.2 ± 3.4	67.5 ± 3.5

Table 4.8: Residual conversion background estimated using different p_T threshold on the partner track.

$M(J/\psi + e)$ GeV	3-4	4-6	6-7	7-12	total
p_T>300MeV	18.19 ± 4.14	11.48 ± 3.47	5.12 ± 1.99	0.82 ± 1.19	35.62 ± 5.88
p_T>400MeV	19.71 ± 4.73	10.81 ± 3.56	5.11 ± 2.14	0.96 ± 1.4	36.61 ± 6.45
p_T>500MeV	18.48 ± 5.03	9.59 ± 3.61	5.02 ± 2.33	1.12 ± 1.64	34.21 ± 6.82

SUNGKYUNKWAN UNIVERSITY

4.3 $b\bar{b}$ background

The $b\bar{b}$ is another major source of background to the B_c signal. The particular process we are concerned about is that one b decays in to a J/ψ and its associated $\bar{b}$ produces an electron either in the direct semileptonic decays or through the so-called sequential decays, $\bar{b} \to c \to e$. It is possible that the electron projects through the J/ψ vertex and the invariant mass of the two falls into the B_c search window, thus the events may not be distinguishable from a B_c decay. We estimated the size of this background using realistic Monte Carlo simulation using offline version 5.3.3.

The Pythia 6.216 is chosen for the generation of the concerned decay chains of the $b\bar{b}$ events. To avoid double counting, the b-hadron is forced to decay to a J/ψ while the $\bar{b}$-hadron is allowed to decay through the default decay table. Details of the Monte Carlo generation and detector simulations are available in Appendix and also in references [61] and [62]. The J/ψ p_T spectrum from this Pythia Monte Carlo were compared to that measured by CDF, as shown in Fig.4.10. The agreement between them is good but some fine tunning could be used to further improve the simulation. Comparing to other uncertainties involving with $b\bar{b}$ background, this tunning is not needed here and the Pythia Monte Carlo is good enough.

There are several parameters most relevant to the estimation of amount of background to B_c: the parton distribution function (PDF), the amount of initial state radiations (ISR) determined by the Pythia parameter PARP(67), and the relative contributions of the three leading sources for $b\bar{b}$ production. The three leading sources are classified as Flavor Creation (FC), Flavor Excitation (FE) and Gluon Splitting (GS). As pointed out by R. Field [63] and confirmed by the Run-I analysis as in the PRD paper [64], there are sizable contributions from the next to leading order process of flavor excitation and gluon splitting in addition to the leading order process of flavor creation. The Run-I analysis done by Kevin Lannon *et al.* [64] used a simultaneous fitting to the lifetime distribution of J/ψ and impact parameter distribution of lepton in two opening angle ($\Delta\phi$) regions between the lepton and J/ψ. This analysis

SUNGKYUNKWAN UNIVERSITY

concluded that the CDF data is in general consistence with the predictions from Pythia after tunning by Rick Filed [63], as shown in Table 4.9. It also indicates the CDF data favors a setting of CTEQ5L for PDF, PARP(67)=4 for ISR and the default fractions FC/FE/GS from the Pythia. We will use events generated using this default setting to estimate the $b\bar{b}$ background in B_c and treat variation from this setting as systematic uncertainty.

Table 4.9: Results of CDF $b\bar{b}$ correlation studies. Run-I studies with simultaneous lifetime and impact parameter fittings to determine fraction of the two b-quarks in $\Delta\phi < 90$ degree range ($F_{forward}$) are shown. Run-II result of scaling factors determined using fitting $\delta\phi$ distributions between data and Monte Carlo of different mechanism's are also shown. Both results are consistent with Pythia predictions.

Run-I $F_{forward}(\%)$ measurements			
Channel	data	Pythia	CDFNote
J/ψ-e	$18.6^{+6.3\ +0.5}_{-5.7\ -0.6} \pm 1.7$	26.4 ± 0.2	7253
J/ψ-μ	$33.4^{+8.9\ +7.7}_{-7.9\ -3.0} \pm 2.3$	25.5 ± 0.4	7253
Run-II $J/\psi - \mu$ scaling studies			
S_{FC}	S_{FE}	S_{GS}	CDFNote
0.86 ± 0.08	0.82 ± 0.06	1.59 ± 0.28	7200.V1
0.90 ± 0.21	0.81 ± 0.37	1.36 ± 0.39	7200.V2

We first check the opening angle distribution between the two b quarks on the $r-\phi$ plane at the generator level without detector simulation and kinematic cuts for their decay products. The event was generated with the requirement that one of the b-quark have a minimal p_T of 5 GeV/c and to be within pseudo-rapidity of 1. The three major $b\bar{b}$ production sources were generated using different processes (MSEL =5 for FC, MSEL=1 for FE and GS in addition to FC) as prescribed in references [61] and [64] to use CPU efficiently. As shown in Fig. 4.11, the flavor creation produces $b\bar{b}$ pairs mostly back-to-back as expected while flavor excitation and gluon splitting have sizable events with the $b\bar{b}$ pairs closely together. We then looked the opening angle distribution between J/ψ and electron with kinematic cuts. The shape of the three sources

SUNGKYUNKWAN UNIVERSITY

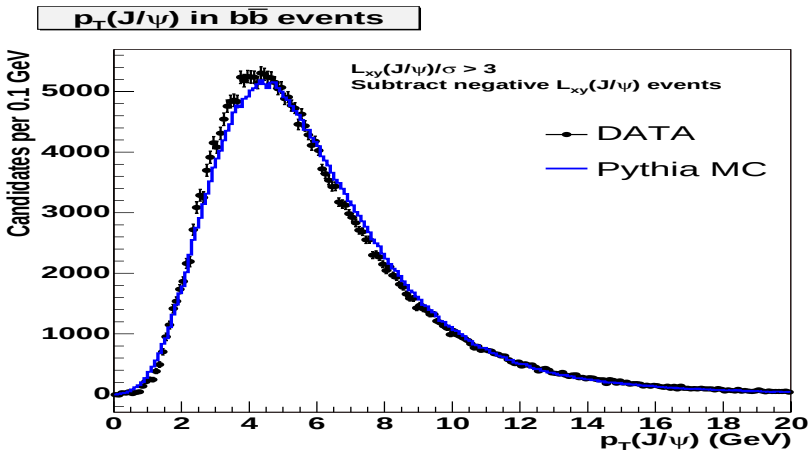

Figure 4.10: J/ψ p_T distribution between Pythia MC (blue lines) with "Rick Filed"tunning and data (black dots). Fake J/ψ is subtracted using sideband subtraction technique for data. The prompt J/ψ contribution in data were also subtracted using J/ψ with negative value of L_{xy}.

stay more or less the same to that before kinematic cuts, as shown in Fig. 4.12.

The Monte Carlo event were then going through full detector simulation using proper setting suggested by the Monte Carlo working group. We analyzed the $b\bar{b}$ events as same as the data and applied all cuts including the 90 degree opening angle cut. Muon tracks from J/ψ are required to be from the expected decay chains using generator level true information. Electron tracks are required to be from different b and in the pseudo-rapidity range of $\mid \eta \mid < 1.0$ but no requirement is made for them to be identified as electron with calorimeter information. The electron identification efficiencies obtained from isolation-weighted methods, dE/dx cut efficiencies and CES fiducial coverage measured using $B^+ \rightarrow J/\psi K^+$ data sample are used to scale down the background number. The Monte Carlo events was normalized using the $B^+ \rightarrow J/\psi K^+$ yields in Monte Carlo sample and in data. In doing so, we found the relative signal ratio of $N(B^+ \rightarrow J/\psi K^+)/N(b \rightarrow J/\psi X)$ in Monte Carlo is lower than the ratio found in data by a factor of 1.15, as shown in

Fig. 4.13. We checked effect of muon p_T turn-on curve effect by re-calculating

SUNGKYUNKWAN UNIVERSITY

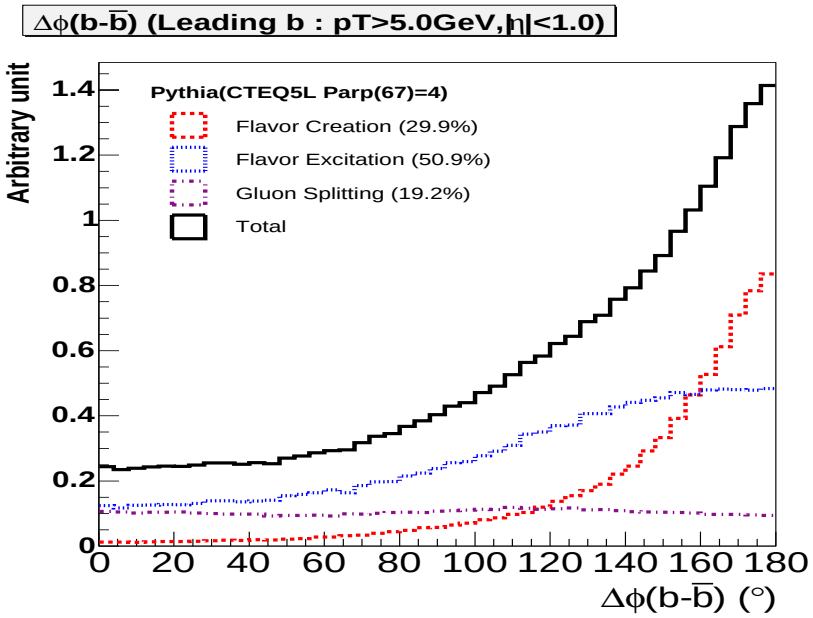

Figure 4.11: Generator level opening angle $\Delta\phi$ distributions of $b\bar{b}$ events for the three sources of flavor creation (black dots with solid line error bars),flavor excitation (red squares with dashed line as error bars) and gluon splitting (blue triangles with dashed line as error bars).Default result from MSEL=1 process (purple dash-doted line) is also shown. The normalized fractions of the three sources are 29.9%:50.9%:19.2% (FC:FE:GS).

the the ratio by using only muons with $p_T > 2.5$ GeV but found the difference persistence. We thus attributes this as the decay table problem in Monte Carlo and decided to scale down the background contributions estimated by 15% accordingly. The J/ψ-electron invariant mass distributions are shown in Fig. 4.14 and the numeric values are tabulated in Table 5.3.

As mentioned before the relative fraction of the three sources differs greatly for different Pythia parameter settings and between different event generators. The combined opening angle distributions of three sources after detector simulation and kinematic selection for these variations are shown in Fig. 4.15. The distributions are quite different over the whole opening angle range and as a result the numbers of $b\bar{b}$ background to B_c are also very different, as shown in Table 4.11. We take the maximum differences from estimation in these tables,

SUNGKYUNKWAN UNIVERSITY

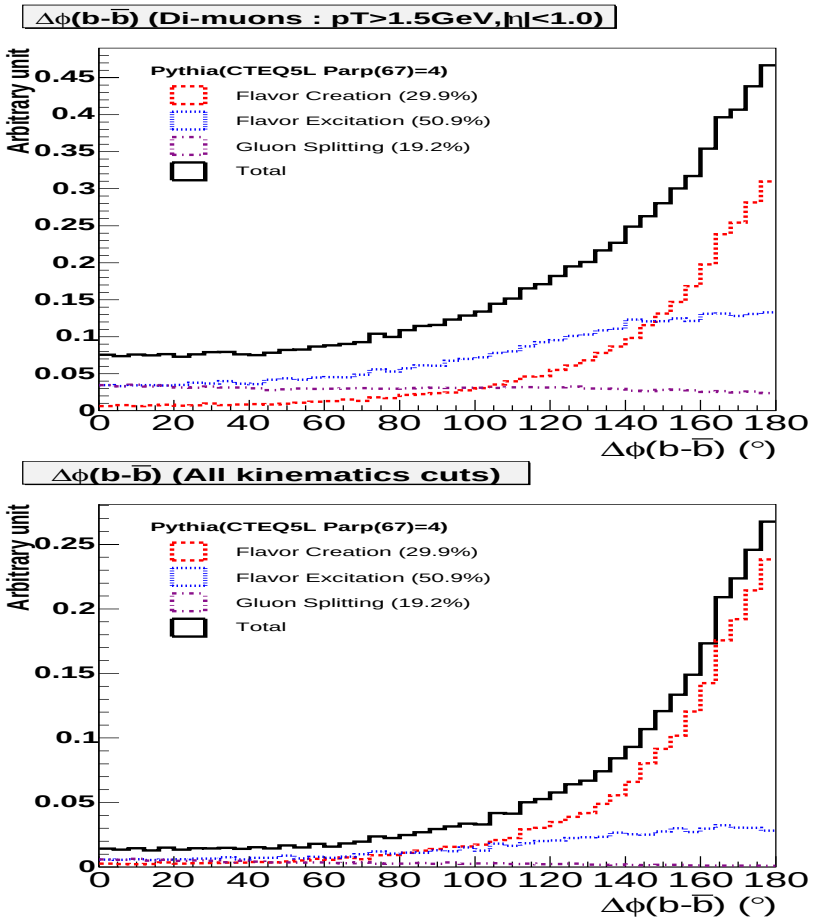

Figure 4.12: Generator level opening angle $\Delta\phi$ distributions between J/ψ and electron from $b\bar{b}$ events for the three sources of flavor creation (black dots with solid line error bars),flavor excitation (red squares with dashed line as error bars) and gluon splitting (blue triangles with dashed line as error bars). The normalized fractions of the three sources are 29.9%:50.9%:19.2% (FC:FE:GS). Top plot requires muons have $p_T > 1.5$ GeV and $\mid \eta \mid < 1.0$. Bottom plot requires additionally $p_T(J/\psi) > 3$ GeV and $p_T(J/\psi + 3rdtrk) > 5$ GeV.

SUNGKYUNKWAN UNIVERSITY

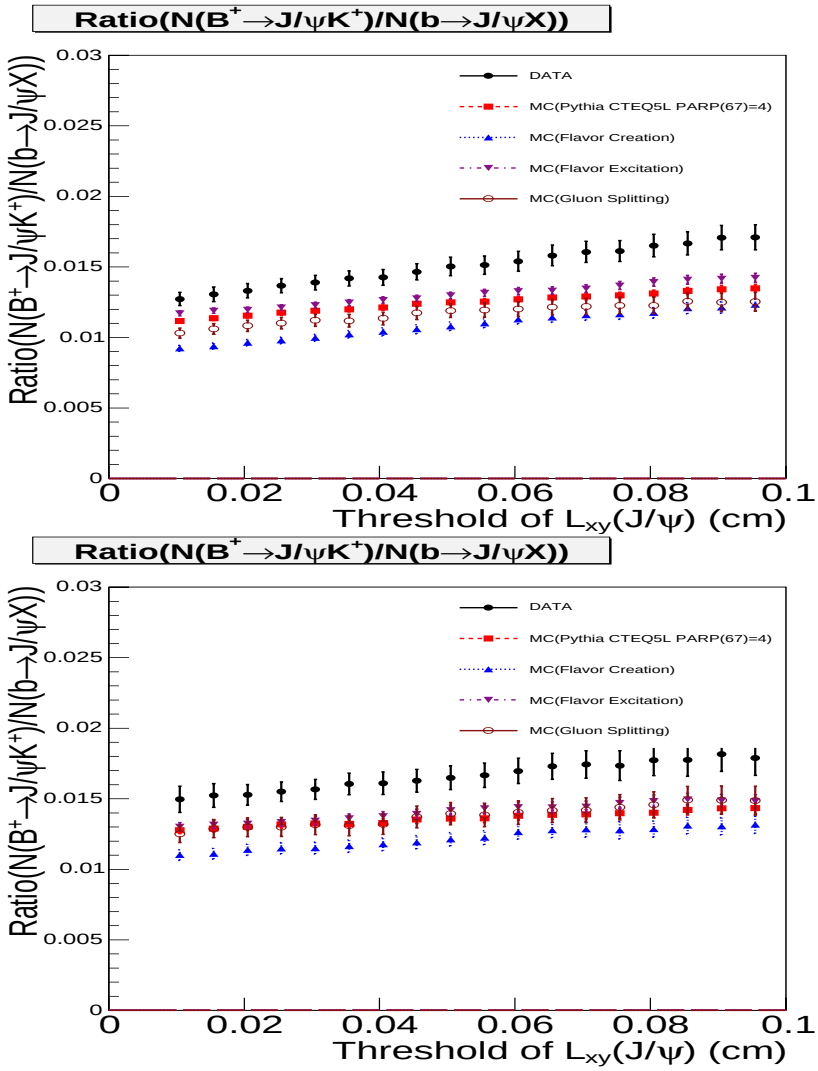

Figure 4.13: Ratio of $N(B^+ \to J/\psi K^+)/N(b \to J/\psi X)$ for data (black dots) and Monte Carlo samples (red squares) as function of minimum J/ψ decay length. Ratios calculated separately for the three $b\bar{b}$ production sources are also included. Top plot are for default muon p_T cut and bottom plot requires all muons have a minimum p_T of 2.5GeV.

SUNGKYUNKWAN UNIVERSITY

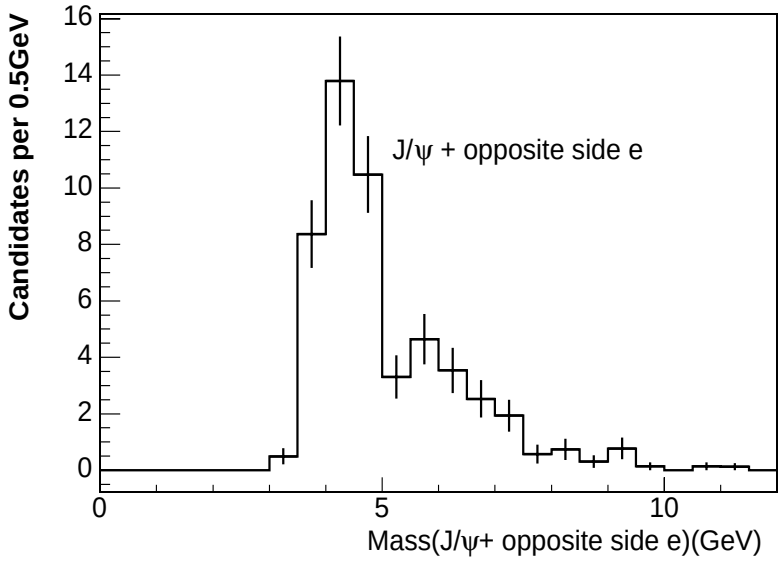

Figure 4.14: Invariant mass distribution of J/ψ-electron pair from $b\bar{b}$ background.

10.55 events as our uncertainties due to Monte Carlo modeling. This is the biggest contribution to the systematic uncertainties in the estimation of $b\bar{b}$ background to the B_c signal.

The number of $B^+ \to J/\psi K^+$ events in Monte Carlo was used as a normalization for luminosity. As discussed before, we found the relative ratios of $N(B^+ \to J/\psi K^+)/N(b \to J/\psi X)$ for the three processes, FC/FE/GS, during the Monte Carlo event generation, are found to be different by about 10%. We treat this differences as an systematic uncertainties related with the normalization of the Monte Carlo event generation.

The next piece of systematic error considered is from the uncertainties of electron identification efficiency. The error on electron identification efficiency from isolation was estimated using the differences of isolated-weighted efficiency and the one directly from $\gamma \to e^+e^-$ sample, as shown in Table 3.3. We assigned a systematic error 2% (0.67 events). The efficiency dependence on the number of silicon hits was also checked by calculating the efficiency for conver-

SUNGKYUNKWAN UNIVERSITY

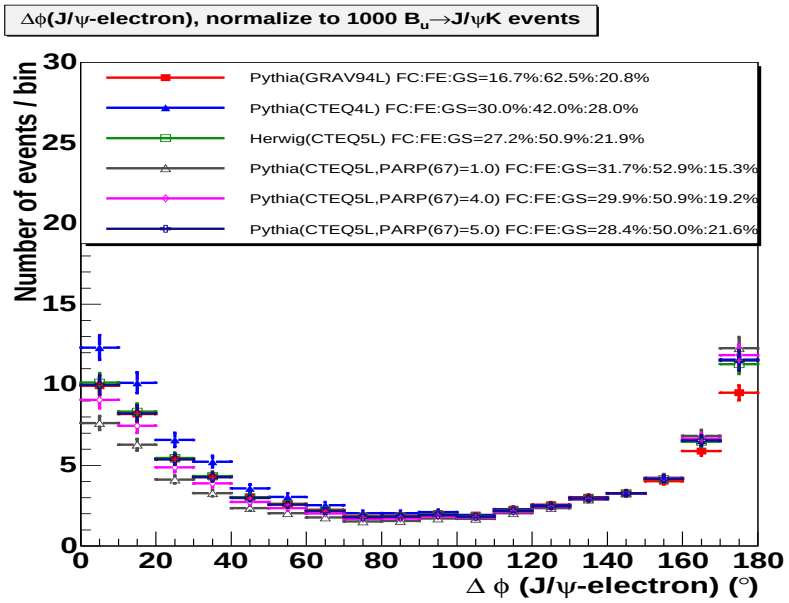

Figure 4.15: Opening angle $\Delta\phi$ distributions of J/ψ and electron from different generators with different parameter settings. Detector simulations were included and all B_c selection cut beside the electron identification and opening angle cuts were applied. The muon and electron tracks were required to come from $\bar{b} \to J/\psi$ and $b \to eX$ with sequential semileptonic decay included.

SUNGKYUNKWAN UNIVERSITY

sion electron tracks with only 3 silicon hits and 4 or more silicon hits. and we found its contribution is 0.39 event. We also checked the sample dependences on the efficiency calculation by using the conversion sample collected with 4 GeV electron in the e+SVT sample instead of the inclusive 8 GeV electron sample. We found 0.46 events.

Finally, the statistical errors from number of $B^+ \rightarrow J/\psi K^+$ event in data sample (2.1%), from CES fudicial coverage (0.33%) and dE/dx efficiency (2.1%) are directly transfered to the uncertainty on the number of $b\bar{b}$ background.

SUNGKYUNKWAN UNIVERSITY

Table 4.10: The relative fraction of FC/FE/GC for $b\bar{b}$ Monte Carlo.

PDF/ISR	FC:FE:GS
GRAV94L/PARP(67)=4	16.7:62.5:20.8
CTEQ4L/PARP(67)=4	30.0:42.0:28.0
CTEQ5L/PARP(67)=1	31.7:52.9:15.3
CTEQ5L/PARP(67)=4	29.9:50.9:19.2
CTEQ5L/PARP(67)=5	28.4:50.0:21.6
Herwig/CTEQ5L	27.2:50.9:21.9

Table 4.11: $b\bar{b}$ background estimated from different Monte Carlo models. The choice of the setting are described in CDFNote 5558 and 6254. The relative fraction of FC/FE/GC are obtained in the generator level with requirement of leading b quark have minimum p_T of 5 GeV/c and in the range of $\mid \eta \mid < 1$. The result is corrected for electron identification efficiency from the cut-based electron reconstruction studies, dE/dx efficiency and CES fiducial coverage.

3-4GeV	4-6GeV	6-7GeV	7-12GeV	0-12GeV
10.81 ± 1.28	35.64 ± 2.36	6.85 ± 1.04	5.43 ± 0.92	58.73 ± 3.02
13.11 ± 1.61	42.60 ± 2.94	8.16 ± 1.29	6.40 ± 1.14	70.27 ± 3.77
8.46 ± 0.99	27.78 ± 1.82	5.23 ± 0.79	4.32 ± 0.72	45.79 ± 2.34
9.90 ± 1.17	32.39 ± 2.15	6.15 ± 0.94	4.97 ± 0.84	53.41 ± 2.75
10.82 ± 1.29	35.36 ± 2.36	6.74 ± 1.04	5.39 ± 0.92	58.31 ± 3.03
10.96 ± 1.31	35.83 ± 2.39	6.84 ± 1.05	5.45 ± 0.93	59.08 ± 3.07

SUNGKYUNKWAN UNIVERSITY

Chapter 5

B_C signal

The signal excess of B_c is discussed in this chapter. We also give the estimates for all systematic errors of background estimates.

5.1 Result of B_c reconstruction

Finally, the J/ψ-electron candidates were counted as function of the invariant mass using selections discussed earlier in Table 3.8. The electrons were required to pass the standard selection cuts. dE/dx requirement of $Z_e/\sigma_Z > -1.3$ was also applied conversion electron was removed if they satisfy $|\Delta \cot \Theta| < 0.05$, $-0.3cm < d_{XY} < 0.5cm$ and $p_T(partner) > 400\ MeV$. In addition, J/ψ-electron pair was removed from the candidate list if the invariant mass of the pair is within 50 MeV/c^2 of the B^+ PDG mass value after assign the electron with a kaon mass. The numbers of J/ψ-electron candidates for different mass window are tabulated in Table 5.3 and plotted in Fig. 5.1.

From counting the candidates in the expected B_c window in 4-6 GeV/c^2 invariant mass window, we found the number of $B_c \to J/\psi eX$ candidates as 185.5 ± 14.7 over an estimated background of $75.1 \pm 4.2 \pm 13.2$. The net excess of signal is 110.4 ± 15.3 events. Background estimations and B_c signal excess in all invariant mass windows are listed in Table 5.4. In the higher mass window, $7 < M(J/\psi + e) < 12$ GeV where the B_c signal is not expected

SUNG KYUN KWAN UNIVERSITY

present, we see an excess of 1.58 events per 1 GeV mass window. Here the excess is calculated from the difference of the number of events between the data and the background then subtracted the combined errors from data and background including both statistical and systematic errors. Although the excess is still consistent with statistical fluctuation, we conservatively assign an systematic error from it by assuming a linear extrapolation to the B_c signal region. The estimated total background in the 4-6 GeV/c^2 mass window is $75.1 \pm 4.2 \pm 13.2$. with the signal events as $110.4 \pm 15.3 \pm 13.2$, where the first error is statistical and second error as systematical error. In Fig. 5.2, the expected B_c signal shape is compared with the data.

Table 5.1: Electron selection variables and their efficiencies. Multiplying efficiencies of each individual cuts, we get an efficiency of 56.5%.

Variable	cut	Efficiency (%)
E_{had}/E_{em}	0.05	87.0
E/P	0.7	92.6
$\mid \Delta X_{CES} \mid$	3 cm	97.4
$\mid \Delta Z_{CES}/ \mid$	3 cm	95.4
χ^2_{strip}	20	98.8
χ^2_{wire}	20	99.6
E_{CES}/p^*	0.2	93.6
E_{strip}/E_{wire}	0.65	93.7
E_{CPR}	1.5	87.1
ΔX_{CPR}	3 cm	99.7

SUNGKYUNKWAN UNIVERSITY

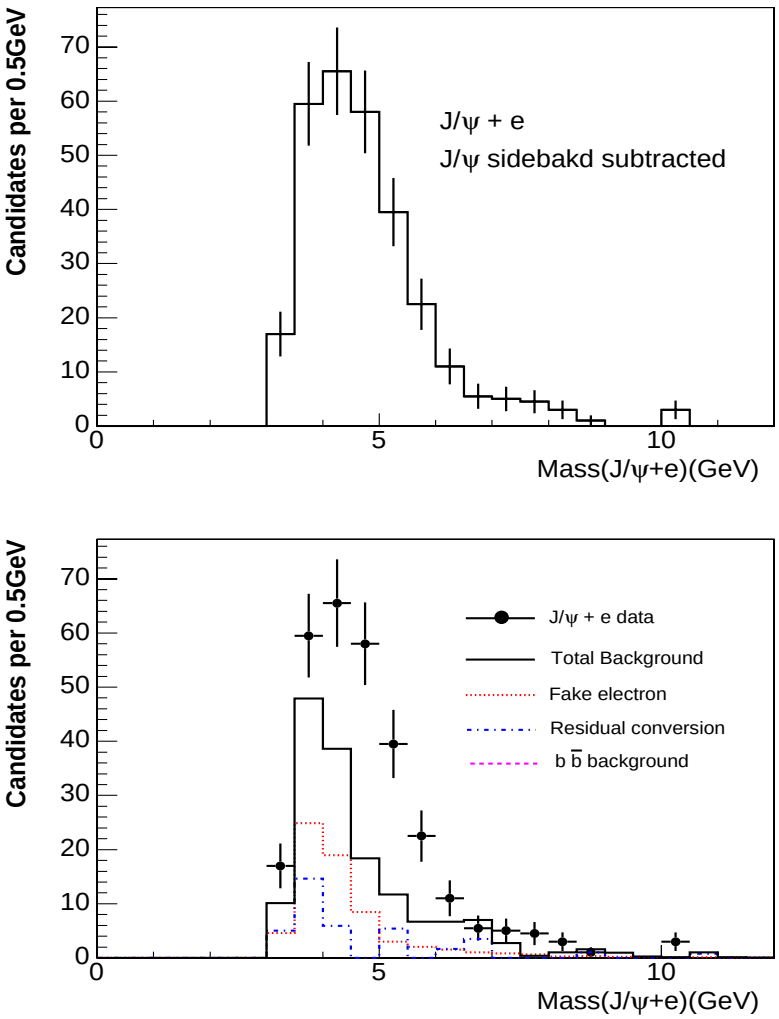

Figure 5.1: Invariant mass distribution of J/ψ-electron candidates reconstructed using likelihood-based electron identification package. Top plot is for signal candidates only and bottom plot include also background contribution. Fake J/ψ contributions for both plots are excluded with mass sideband subtractions.

SUNG KYUN KWAN UNIVERSITY

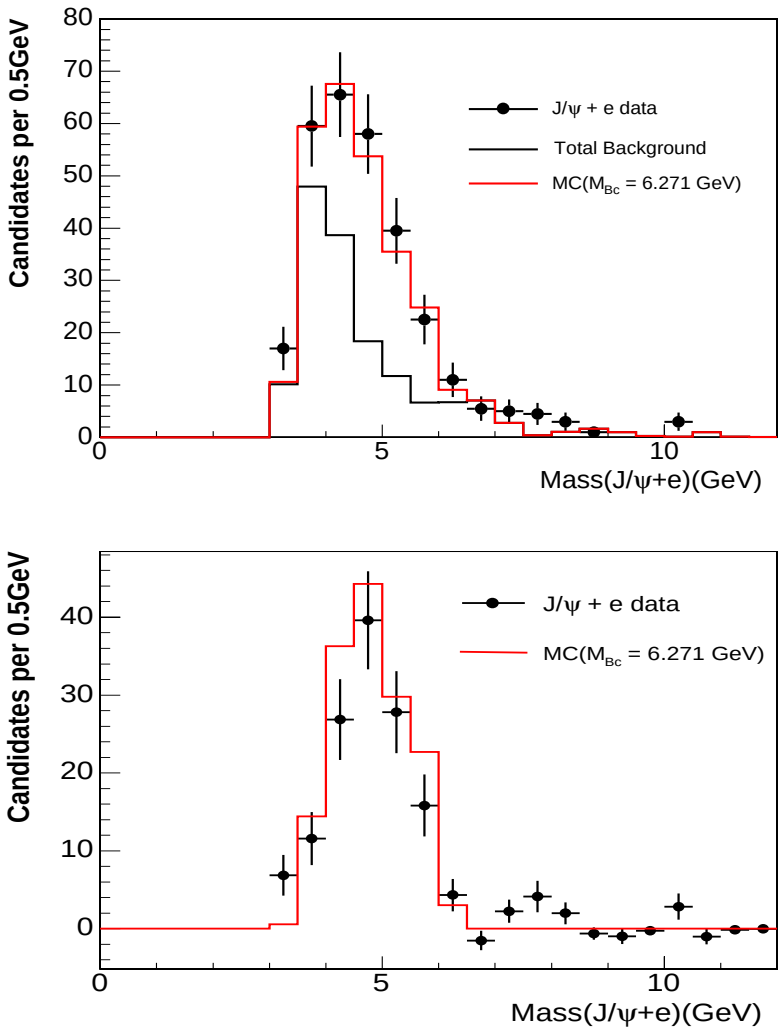

Figure 5.2: Comparison of the expected B_c signal to the data for the invariant mass distribution of J/ψ-electron. Top plot shows all data point with estimated background and expected signal shape. Bottom plot shows the extracted signal shape from data and that expected from Monte Carlo.

SUNGKYUNKWAN UNIVERSITY

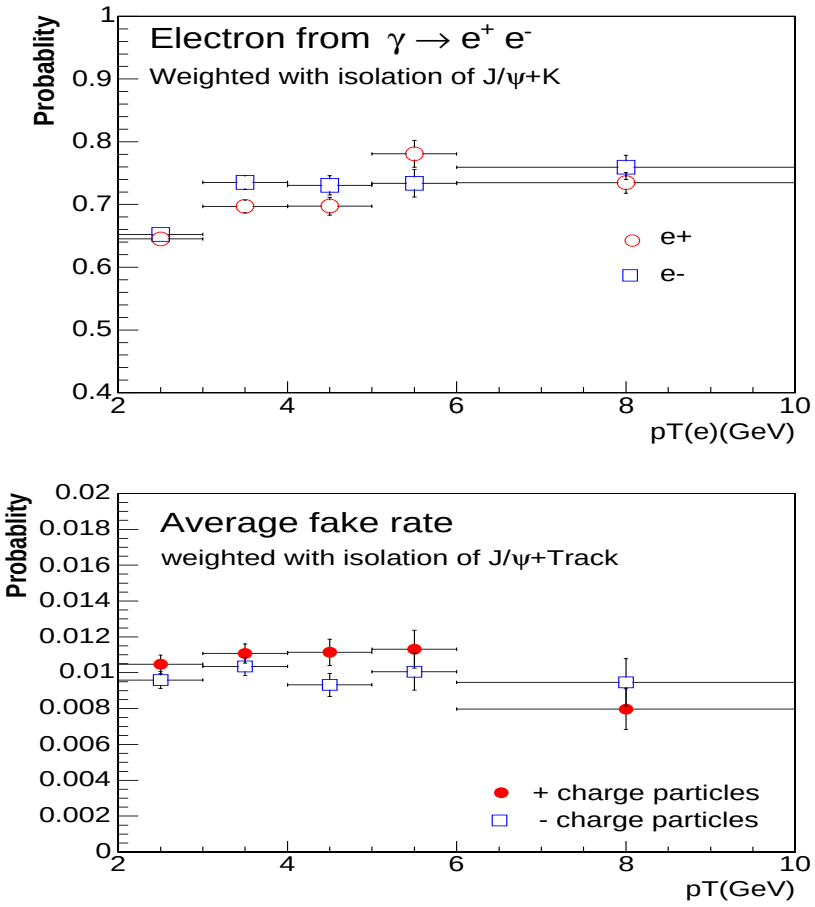

Figure 5.3: The electron reconstruction efficiency (top) and averaged hadron faking electron probabilities (bottom) as function of track p_T. Isolation corrections were made using event-re-weighting method.

SUNGKYUNKWAN UNIVERSITY

Table 5.2: Electron reconstruction efficiency (%) and averaged hadron faking electron probabilities (%) as function of track p_T for cut-based electron identification method. The efficiencies were obtained using electrons identified from photon conversion reconstructed in 8 GeV triggered single electron sample. Isolation corrections were made by event re-weighting method to force the photon conversion sample have same distribution as from $B^+ \to J/\psi K^+$. Fake rates were obtained by averaging pion, kaon and proton's fake rates obtained in $D^0 \to K\pi$ and $\Lambda \to p\pi$ decays and by using the particle-type fractions obtained in Pythia MC sample. Isolation correction were also made to the D^0 and Λ sample by re-weighting to force them have the same isolation distribution as from the J/ψ+track sample.

p_T (GeV/c)	Efficiency		Averaged fake rate	
	+ charge	- charged	+ charged	- charged
2-3	64.5 ± 0.65	65.23 ± 0.67	1.16 ± 0.03	1.02 ± 0.03
3-4	69.69 ± 1.03	73.52 ± 1.12	1.19 ± 0.04	1.08 ± 0.04
4-5	69.73 ± 1.43	73.05 ± 1.54	1.18 ± 0.06	0.95 ± 0.06
5-6	78.07 ± 2.14	73.39 ± 2.20	1.19 ± 0.09	1.04 ± 0.09
> 6	73.46 ± 1.65	75.93 ± 1.94	0.98 ± 0.10	1.13 ± 0.13

SUNGKYUNKWAN UNIVERSITY

Table 5.3: Background estimations and data excess in $J/\psi + e$ invariant mass windows. We choose the signal range between $4GeV/c^2$ to $6GeV/c^2$. There are 2850 ± 60 $B^+ \to J/\psi K^+$ events reconstructed in the same data set. The selections for $J/\psi + e$ and B^+ are listed in Table 3.8 and Table 3.9.

$M(J\psi e)(GeV/c^2)$	signal region	total range
Fake e (J/ψ peak)	38.43 ± 0.62	77.13 ± 0.88
Fake e (sideband x2)	13.01 ± 0.36	21.90 ± 0.47
Fake Electron	31.93 ± 0.65	66.18 ± 0.91
Tagged Conv. (J/ψ peak)	15.00 ± 3.87	46.00 ± 6.78
Tag. Conv. (sidebands x2)	5.00 ± 2.24	12.00 ± 3.46
Res. Conv. (J/ψ peak)	13.00 ± 3.42	41.92 ± 6.26
Res.Conv. (sidebands x2)	4.38 ± 1.97	10.63 ± 3.10
Res. Conv electron	$\mathbf{10.81 \pm 3.56}$	$\mathbf{36.61 \pm 6.45}$
$b\bar{b}$	$\mathbf{32.39 \pm 2.15}$	$\mathbf{53.41 \pm 2.75}$
Total background	$\mathbf{75.13 \pm 4.21}$	$\mathbf{156.20 \pm 7.07}$
DATA in (J/ψ peak)	205.00 ± 14.32	328.00 ± 18.11
DATA (sidebands x2)	39.00 ± 6.24	66.00 ± 8.12
DATA J/ψ +e	$\mathbf{185.50 \pm 14.66}$	$\mathbf{295.00 \pm 18.56}$
Excess	$\mathbf{110.37 \pm 15.25}$	$\mathbf{138.8 \pm 19.86}$

SUNGKYUNKWAN UNIVERSITY

Table 5.4: Summary of systematic errors. We choose the signal range between $4GeV/c^2$ to $6GeV/c^2$.

$M(J\psi e)(GeV/c^2)$	signal region	total range
isolation	1.96	3.79
numSiHits	0.39	0.70
π/K/p frac.	0.53	0.95
fake rate stat. err.	2.17	4.14
Fake e - total	$31.93 \pm 0.65 \pm 3.00$	$66.18 \pm 0.91 \pm 5.74$
p_T spectra	4.88	17.52
dalitz	0.15	0.66
lifetime	0.39	1.52
ϵ_{conv} stat. err.	0.81	2.44
Conversion -total	$10.81 \pm 3.56 \pm 5.26$	$36.61 \pm 6.45 \pm 17.93$
PDF/ISR	10.21	16.86
dE/dx efficiency	0.67	1.10
stat. err. of ϵ_e	0.46	0.73
eID ϵ_e-isolation	1.61	2.72
Br(B^+)	4.86	8.01
N(B^+) in data	0.60	0.98
N(B^+) in MC	0.71	1.18
CES coverage	0.91	1.50
eID ϵ_e-sample	0.46	0.67
numSiHits	0.39	0.7
$b\bar{b}$ - total	$32.39 \pm 2.15 \pm 11.68$	$53.41 \pm 2.75 \pm 19.38$
high mass excess	1.16	5.23
Total background	$75.13 \pm 4.21 \pm 13.21$	$156.20 \pm 7.07 \pm 27.52$
DATA	185.50 ± 14.66	295.00 ± 18.56
EXCESS	$110.37 \pm 15.25 \pm 13.21$	$138.8 \pm 19.86 \pm 27.52$

SUNG KYUN KWAN UNIVERSITY

Chapter 6

Production Cross-section measurement

From the B_c yield in Table 5.3, the B_c production cross section times the $B_c^+ \to J/\psi e^+\nu$ branching fraction $\sigma \cdot BR(Bc^+ \to J/\psi e^+\nu)$ was calculated. We express this physics quantity relative to that for the topologically similar decay of $B^+ \to J/\psi K^+$. The reconstructed number of events were corrected by efficiencies and acceptances to calculated cross section ratio:

$$\begin{aligned} \frac{\sigma(B_c^+) \cdot BR(B_c^+ \to J/\psi e^+\nu)}{\sigma(B^+) \cdot BR(B^+ \to J/\psi K^+)} &= \frac{N(B_c^+)/(KA(B_c^+) \times \epsilon(B_c^+))}{N(B^+)/(KA(B^+) \times \epsilon(B^+))} \\ = \frac{N(B_c^+)}{N(B^+)} \times \frac{KA(B^+)}{KA(B_c^+)} \times \frac{\epsilon(B^+)}{\epsilon(B_c^+)} &= \frac{N(B_c^+)}{N(B^+)} \times R^K \times R^\epsilon, \end{aligned}$$

where $KA(B_c^+)$ and $KA(B^+)$ denote as kinematic acceptances for for B_c^+ and B^+ including effects from momentum, geometry and lifetime selection cuts; $\epsilon(B_c^+)$ and $\epsilon(B^+)$ are the trigger and reconstruction efficiencies for B_c^+ and B^+; R^K is kinematic acceptance ratio between B^+ and B_c^+, $R^K = KA(B^+)/KA(B_c^+)$; and R^ϵ is the trigger and reconstruction ratio between B^+ and B_c^+, $R^\epsilon = \epsilon(B^+)/\epsilon(B_c^+)$. The efficiency ratio R^ϵ can be further broken down to

$$\begin{aligned} R^\epsilon &= \frac{\epsilon^u(trigger) \times \epsilon^u(vertex) \times \epsilon^u(J/\psi) \times \epsilon^u(K_{trk})}{\epsilon^c(trigger) \times \epsilon^c(vertex) \times \epsilon^c(J/\psi) \times \epsilon^c(e_{trk}) \times \epsilon(eID) \times \epsilon(dE/dx)} \\ &= \frac{1}{\epsilon(eID) \times \epsilon(dE/dx)}, \end{aligned}$$

SUNG KYUN KWAN UNIVERSITY

where $\epsilon^{u/c}(trigger)$ are the di-muon trigger efficiencies for $B^+ \rightarrow J/\psi K^+$ and $B_c \rightarrow J/\psi e^+\nu$, $\epsilon^{u/c}(vertex)$ the 3-prong vertex reconstruction efficiencies, $\epsilon^{u/c}(J/\psi)$ the reconstruction efficiencies for $J/\psi \rightarrow \mu^+\mu^-$ decay, $\epsilon^u(K_{trk})$ and $\epsilon^c(e_{trk})$ are the tracking efficiencies for the kaon and electron tracks, and $\epsilon(eID)$ $\epsilon(dE/dx)$ are the electron identification selection efficiency and COT dE/dx cut efficiency on the electrons. Most of the efficiencies are expected to be same for B^+ and B_c except the additional $\epsilon(eID)$ $\epsilon(dE/dx)$.

The explicit cut on the combined momentum of J/ψ and electron, $p_T(J/\psi + e) > 5$ GeV imposed a limit on the $p_T(B_c)$ ranges we are sensitive to. From MC simulation, as shown in Fig. 6.1, we are limited to the transverse momentum range of $p_T(B_c) > 4$ GeV and the rapidity range of $\mid y \mid < 1$. So the cross section here is defined as that for kinematic range of $P_T(B) > 4$ GeV with $\mid y(B) \mid < 1$. Accordingly, the definition of the kinematic acceptance, $KA(B^+)$ and $KA(B_c^+)$, is the fraction of events passing kinematic cuts (p_T, η and L_{xy}) for the B decay channels generated in the kinematic range of $p_T(B) > 4$ GeV and $\mid y(B) \mid < 1$

6.1 Acceptance estimation for B_c^+ and B^+

Monte Carlo simulated events were used to estimate the kinematic acceptance. Pure signal $B_c^+ \rightarrow J/\psi e\nu$ and $B^+ \rightarrow J/\psi K^+$ events were generated using Bgenerator. The events were generated with $p_T > 4$ GeV and $\mid y \mid < 1$ for pure signals $B_c \rightarrow J/\psi e\nu$ and $B^+ \rightarrow J/\psi K^+$ in "Bgenerator" and pass through full detector simulation. Monte Carlo event were analyzed in the same way as for data.

The input p_T spectrum for B_c is from a theoretical calculation [29, 58] and the mass and lifetime of B_c are chosen to be 6.271 GeV/c and 0.55 ps for our central value of acceptance calculation. The inclusive B p_T spectrum measured from CDF [65] is used for B^+ spectrum. The two spectra are shown in Fig. 6.2. The input B_c spectrum is much softer than that of B^+. We compared the p_T distribution between data and this Monte Carlo for J/ψ, electron and J/ψ+electron combined, as shown in Fig. 6.3. The comparisons were done

SUNG KYUN KWAN UNIVERSITY

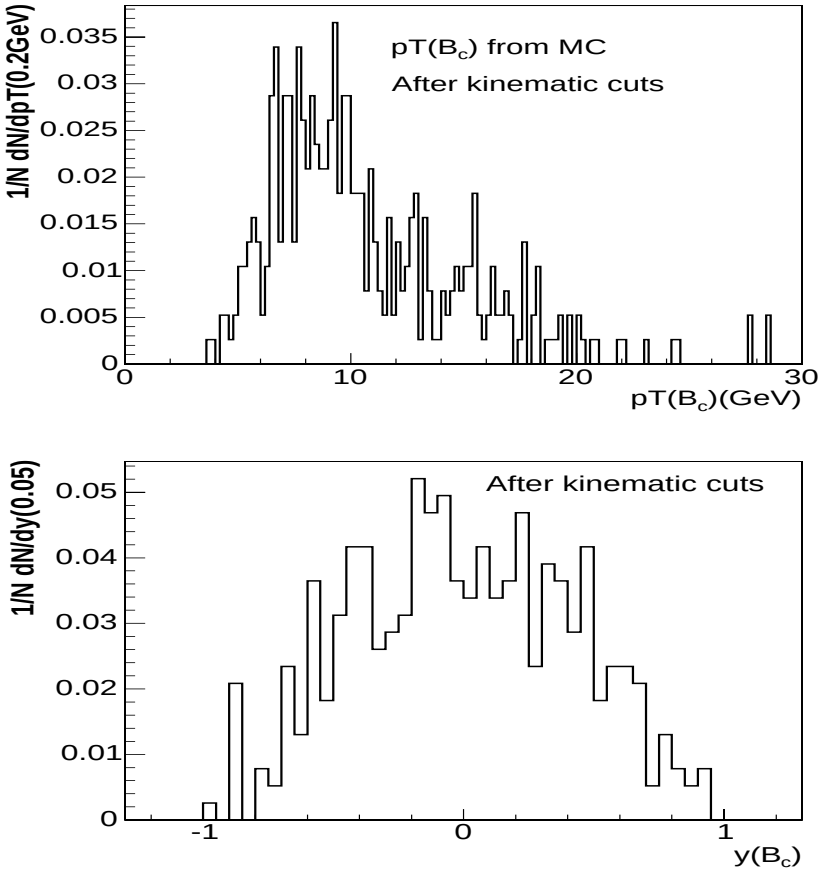

Figure 6.1: The kinematic limited range of p_T (top) and rapidity (bottom) for B_c meson in the Monte Carlo simulation events after event selection criteria the same as for data applied. The input p_T spectrum of B_c is that from reference [29].

SUNG KYUN KWAN UNIVERSITY

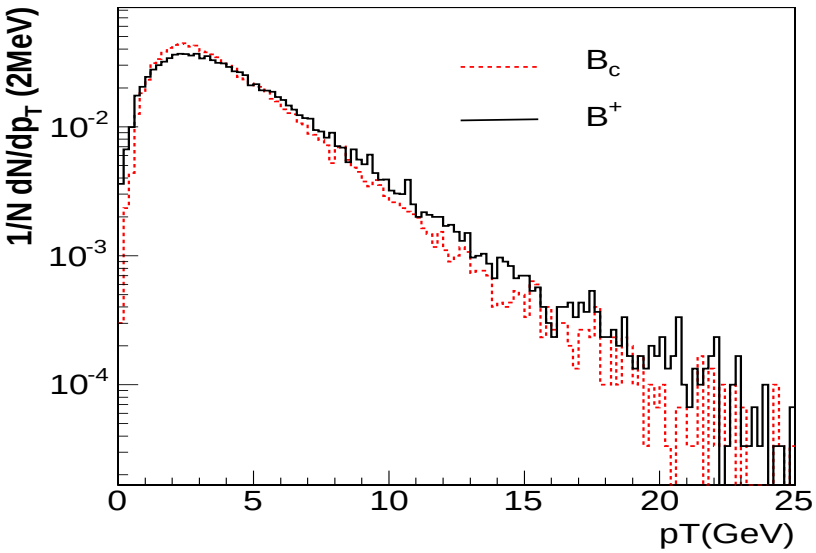

Figure 6.2: Input p_T spectrum for B_c meson (red, dashed lines) and B^+ (black, solid lines) in the Monte Carlo simulation.

using B_c decay since its p_T spectrum is less understood. The agreements are in general satisfactory but since there is no experimental measurement for the B_c spectrum yet, we will vary the spectrum during the acceptance calculation as one source of systematic error.

One of the important cut during event selection is the decay length significance of the 3-prong vertex, $L_{xy}/\sigma > 3$, where the signed decay length is calculated from the distance of the 3-prong vertex, reconstructed using dimuon and electron or kaon tracks, to that of the beam spot where $b-$hadron is assumed to be produced. We first checked the error calculation in Monte Carlo simulation by comparing the error distribution and also by comparing the pull distributions as shown in Fig. 6.4. In general, the Monte Carlo events tends to have a larger error than in the data and the width of the pull distribution tends to be close to 1 while in data the pull distribution has a width larger than 1. This is in a good agreement with the observation of CDFNote-7500 [66] where an error scaling factor for $B^+ \to J/\psi K^+$ of 1.241 ± 0.016 was extracted. For

SUNGKYUNKWAN UNIVERSITY

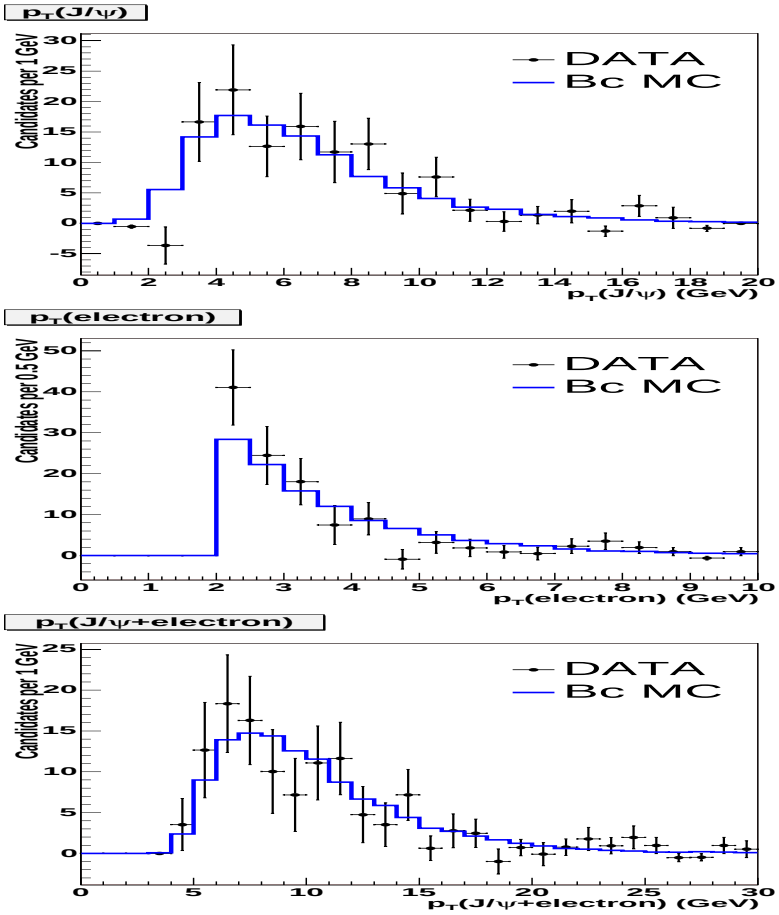

Figure 6.3: The comparison of p_T distributions between data (data with error bars) and signal $B_c \to J/\psi e\nu$ Monte Carlo (solid lines) for $p_T(J/\psi)$, $p_T(e)$ and $p_T(J/\psi + e)$. Result from likelihood-based analysis with background subtraction were used for data points.

SUNG KYUN KWAN UNIVERSITY

our central value calculation for acceptance, we scaled down the error on decay length for Monte Carlo events to force it have a pull distribution of 1.241. We add the differences before and after error scaling as one source of systematic errors.

In Table 6.1, the acceptance ratios $R^K = KA(B^+)/KA(B_c^+)$ for different Monte Carlo input parameters were listed. The uncertainties on the B_c p_T spectrum and lifetime are the source of two biggest systematic errors on the acceptance ratio. The variation on the p_T spectrum came from the difference between using a theory prediction as in reference [29] and that measured by CDF for inclusive $H_b \to J/\psi X$ [65]. We also checked variations of the p_T spectrum estimated from reference [29] for different B_c mass assumed and different B_c production processes, such as $gg \to B_c$, $gg \to B_c^*$ and $q\bar{q} \to B_c$. We found the changes on the acceptance ratio much smaller than the one obtained using inclusive $H_b \to J/\psi X$ spectrum. The range from lifetime variation is from 0.5ps to 0.7ps as in reference [25]. The error from the mass variation are within statistical error and we take the largest of the two changes as the symmetric error. Beside the lifetime variation, we use the symmetrical errors from variations on p_T spectrum and decay length error scaling to cover any potential changes in the opposite direction.

The Monte Carlo events for the acceptance calculation were generated with the exclusive $B_c \to J/\psi e\nu$ decays. Other inclusive semileptonic decays where the J/ψ or electron are decay products from higher mass states, are expected to have a lower reconstruction efficiency since they produce a J/ψ and electron pair with softer momentum and also with a smaller invariant mass. We generated these events using branching ratios predicted in a theory calculation [25], as shown in Table 6.1. The acceptance ratio R^K for these decays were found to be 18.64 ± 0.53 for $p_T > 0$ and 16.70 ± 0.48 for $p_T > 4$ GeV comparing to 4.929 ± 0.091 and 4.416 ± 0.082 respectively for the exclusive decays. These numbers imply that the exclusive B_c semileptonic decays other than that of $B_c \to J/\psi e\nu$ have an averaged acceptances only 26% of that for the $B_c \to J/\psi e\nu$. The contributions from these non-exclusive decays for the reconstructed semileptonic decays is about 3.4% instead of the 11.6% calcu-

SUNG KYUN KWAN UNIVERSITY

lated from using branching ratios. So we treat this contributions as one source of systematic error for the acceptance calculation. In Table 6.1, the differences on R^K before and after including the exclusive decays are around 8% as expected.

We followed CDFNote 6391 [67] to estimate uncertainty on the kaon track detection from detector material counting in the simulation. On average, the kaon track has a probability of 4% to decay inside the CDF detector due to nuclear interactions, see Table 14 of CDFNote 6391. We took an uncertainty of 25% on this probability and assign a 1% systematic error on the acceptance of $B \to J/\psi K$. We followed the $W \to e\nu$ cross section analysis [68] to assign a 1% uncertainty on the electron track detection due to detector material counting in Monte Carlo. The overall uncertainty on the acceptance ratio R^K due to material counting in Monte Carlo simulation is thus taken 2%.

There is no di-muon trigger simulation implemented during the central value Calculation for the acceptance ratio. We expect the di-muon trigger has similar efficiency for both B_c and B^+ channel. Nevertheless, we estimated the effect by re-weighting the reconstructed events by the efficiency curves from reference [70] and re-calculate the acceptance ratio, as shown in Table 6.1. The acceptance ratio is found to be about 2.7% lower which could be traced down the small differences of the muon p_T and open angle distributions of the $B_c \to J/\psi$ and $B \to J/\psi K$ decays.

After adding all variations in quadrature and then averaging the asymmetric errors as the total systematic error, we obtained:

$$R^K(p_T > 0, \mid y \mid < 1) = KA(B^+)/KA(B_c^+) = 4.93 \pm 0.09 \pm 1.50,$$
$$R^K(p_T > 4, \mid y \mid < 1) = KA(B^+)/KA(B_c^+) = 4.42 \pm 0.08 \pm 1.02. \qquad (6.1)$$

SUNG KYUN KWAN UNIVERSITY

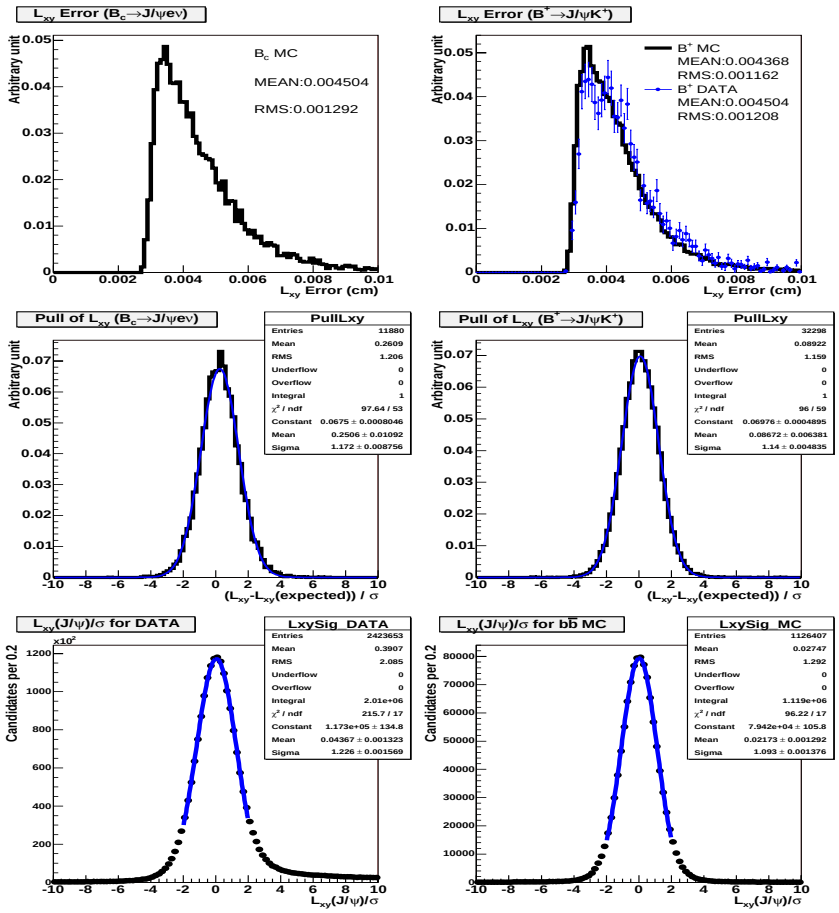

Figure 6.4: Input p_T spectrum for B_c meson (red, dashed lines) and B^+ (black, solid lines) in the Monte Carlo simulation.

SUNG KYUN KWAN UNIVERSITY

Table 6.1: The calculated acceptance ratio of $R^K = KA(B^+)/KA(B_c^+)$. The central values were calculated using with $M_{B_c} = 6.271$ GeV, $\tau_{B_c} = 0.55$ ps, p_T spectrum from reference [30, 25, 27] and with L_{xy} scaling down. The acceptance ratios for both B mesons with $p_T > 4$ GeV, $\mid y \mid < 1$ and $p_T > 0$ GeV, $\mid y \mid < 1$ are listed.

MC parameters	$R^K(p_T > 0)$	ΔR^K	$R^K(p_T > 4)$	ΔR^K
Central value	4.929 ± 0.091	0	4.416 ± 0.082	0
$M_{Bc} = 6.291$ GeV	4.914 ± 0.091	± 0.015	4.403 ± 0.082	± 0.013
$M_{Bc} = 6.251$ GeV	4.904 ± 0.091	± 0.025	4.394 ± 0.082	± 0.022
$\tau_{Bc} = 0.70$ ps	4.549 ± 0.083	-0.38	4.076 ± 0.074	-0.34
$\tau_{Bc} = 0.50$ ps	5.59 ± 0.11	+0.66	5.006 ± 0.096	+0.59
$H_b \rightarrow J/\psi X$ spectrum	3.578 ± 0.062	± 1.351	3.578 ± 0.062	± 0.838
No L_{xy} error scaling	5.108 ± 0.096	± 0.179	4.576 ± 0.086	± 0.16
Including $J/\psi X e\nu$	5.32 ± 0.10	+0.391	4.769 ± 0.090	+0.353
Trigger simulation	4.798 ± 0.088	-0.131	4.299 ± 0.079	-0.117

Table 6.2: The inclusive B_c semileptonic decays and their branching ratios. The effective branching ratio $Br(B_c \rightarrow J/\psi e X \nu)$ is obtained by multiplied of all branching ratio in the process.

Decay	$Br(B_c \rightarrow XY\nu)(\%)$	$Br(X \rightarrow J/\psi)$ or $Br(Y \rightarrow e)$	$Br(B_c \rightarrow J/\psi e X \nu)$ (%)
$B_c \rightarrow J/\psi e\nu$	1.9	100	1.9
$B_c \rightarrow J/\psi \tau\nu$	0.48	17.84	0.086
$B_c \rightarrow \psi(2S) e\nu$	0.094	57.6	0.054
$B_c \rightarrow \psi(2S) \tau\nu$	0.008	57.6*0.1784	0.00082
$B_c \rightarrow B_s e\nu$	4.03	1.094	0.044
$B_c \rightarrow B_s^* e\nu$	5.06	1.094	0.0554
$B_c \rightarrow B^0 e\nu$	0.34	1.094	0.0037
$B_c \rightarrow B^{0*} e\nu$	0.58	1.094	0.0064

SUNG KYUN KWAN UNIVERSITY

6.2 Production cross-section results

Using the acceptance ratio calculated from Monte Carlo simulation, $4.93 \pm 0.09 \pm 1.50$ for B mesons with all p_T in rapidity of $| y | < 1$ and $4.42 \pm 0.08 \pm 1.02$ for B mesons with $p_T > 4$ GeV and $| y | < 1$, the electron identification efficiency on Table 5.1 and the dE/dx cut efficiency $90.56 \pm 0.87\%$ measured using electrons from data, we corrected the $B_c \to J/\psi e\nu$ and $B^{\to} J/\psi$ signal yields, $110.4 \pm 15.3 \pm 13.2$ and 2850 ± 60 to obtain the cross section ratio:

$$\begin{aligned} \frac{\sigma(B_c^+) \cdot BR(B_c^+ \to J/\psi e^+ \nu)}{\sigma(B^+) \cdot BR(B^+ \to J/\psi K^+)} &= 0.317 \pm 0.044(\text{stat.}) \pm 0.048(\text{yield}) \pm \\ &\quad 0.096(\text{acceptance}) \quad (p_T > 0, | y | < 1) \\ &= 0.284 \pm 0.040(\text{stat.}) \pm 0.043(\text{yield}) \pm \\ &\quad 0.065(\text{acceptance}) \quad (p_T > 4, | y | < 1), \end{aligned}$$

where the first error is the statistical error from B_c and B^+ yields, the second error the systematic error due to from B_c yield systematic error and electron identification and dE/dx efficiency uncertainties both statistical and systematic errors, and the third error the systematic error from the acceptance ratio calculation uncertainties.

The values of $\sigma(B^+) \cdot BR(B^+ \to J/\psi K^+)$ is extracted using CDF's inclusive H_b cross section result of $\sigma(H_b, | y | < 0.6) = 17.6 \pm 0.4^{+2.5}_{-2.3}$ μb [65], $f(H_b \to B^+) = 39.7 \pm 1.0\%$ [71] and $BR(B^+ \to J/\psi K^+) = 0.100 \pm 0.004\%$ [71],

$$\begin{aligned} \sigma(B^+) \cdot BR(B^+ \to J/\psi K^+) &= 11.65 \pm 1.64 \; nb \; (p_T > 0, | y | < 1) \\ &= 5.23 \pm 0.74 \; nb \; (p_T > 4, | y | < 1). \quad (6.2) \end{aligned}$$

Using these values, we obtained:

$$\begin{aligned} \sigma(B_c^+) \cdot BR(B_c \to J/\psi e\nu) &= 3.7 \pm 0.5 \pm 1.3 \; nb \; (p_T > 0, | y | < 1) \\ &= 1.48 \pm 0.20 \pm 0.44 \; nb \; (p_T > 4, | y | < 1) \quad (6.3) \end{aligned}$$

SUNG KYUN KWAN UNIVERSITY

Where the first error as the statistical error and the second error the systematic error from all sources combined. Assuming a value of $BR(B_c \to J/\psi e\nu) = 1.9\%$ as in reference [25] and in Table 6.1, we obtain the B_c production cross-section as

$$\begin{aligned} \sigma(B_c^+) &= 194.7 \pm 26.3 \pm 68.4 \; nb \; (p_T > 0, \mid y \mid < 1) \\ &= 77.9 \pm 10.5 \pm 23.2 \; nb \; (p_T > 4, \mid y \mid < 1), \end{aligned} \tag{6.4}$$

SUNG KYUN KWAN UNIVERSITY

SUNG KYUN KWAN UNIVERSITY

Chapter 7

Result

From a J/ψ triggered data sample of $360pb^{-}1$ collected by the CDF II detector, we measured the production cross section of the B_c meson using its semileptonic decay channel. From a correlation studies of the J/ψ - electron pairs, background from fake electron source, residual conversion electron and generic $b\bar{b}$ events were estimated. A signal of $B_c \to J/\psi e\nu$ of the size 110.4 ± 15.3 over a background level of $75.13 \pm 4.21 \pm 13.21$ was observed. A production cross section of $0.284 \pm 0.040(\text{stat.}) \pm 0.043(\text{yield}) \pm 0.065(\text{acceptance})$, relative to $B^+ \to J/\psi K$ for B meson in the kinematic range of $p_T > 4$ GeV and $\mid y \mid < 1$ was extracted after acceptance and reconstruction efficiency corrections.

SUNG KYUN KWAN UNIVERSITY

SUNG KYUN KWAN UNIVERSITY

Appendix A

A detail of Event selection

A.1 Electron from photon conversion sample, $\gamma \rightarrow e^+e^-$

Single lepton trigger dataset (blpc0d) is used to obtain conversion sample. Level 3 trigger bit "ELECTRON_CENTRAL_8" is selected. There is no biased track in $p_T < 8GeV$ region. The first step of a conversion-finding is to constraint a pair of oppositely charged tracks to originate from a common vertex. At the point of conversion, both particles are paralleled and follow the direction of the parent photon. In our case, one of the tracks is required to be identified as electron. We then look for an opposite-signed track as a conversion partner that satisfy$|d_{XY}| < 0.2cm$ and $|\Delta cot\Theta| < 0.02$, where $\Delta cot\Theta$ and d_{XY} is the $\cot\Theta$ and $R\delta phi$ separations of the two tracks at the point of conversion. Conversion radius is required to be at most 12 cm. One track with $p_T > 8GeV$ and $EmEt > 8GeV$ is selected as trigger lepton, and another track is used as non-biased electron. Tracks are selected to satisfy same quality cuts as Bc analysis. Pointing CES fiducial is also required. Pointing different wedges for the 2 tracks is required to avoid trigger bias on unbiased track. Sideband in $\Delta cot\Theta$ is subtracted to obtain pure e electron signatures.

SUNG KYUN KWAN UNIVERSITY

A.2 $D^0 \to K\pi$ sample

Two track trigger dataset (xbhd0d) is used to obtain D^0 sample. Level-3 trigger bit "B_CHARM" is chosen. Tracks are selected to satisfy same quality cuts as Bc analysis. Additionally impact parameter around beam line is required to be $90\mu m < d_0 < 110\mu m$, $d_0(K) \times d_d(\pi) < 0$. Two tracks are required to be pointing CES fiducial and different wedges. CTVMFT vertex fit is applied and the fit $\chi^2 < 30\%$, $p_T(D^0) > 5.5GeV$, impact parameter of $D^0 < 100\mu m$ and $L_{xy}(D^0) > 350\mu m$ cuts are required.

A.3 $\Lambda^0 \to P\pi$ sample

Two track trigger dataset (xbhd0d) is used to obtain Λ^0 sample. Level 3 trigger bit "B_CHARM" is chosen. Proton track is selected to satisfy same quality cuts as Bc analysis. Additionally impact parameter around beam line is required to be at least $120\mu m$, and p_T of proton is greater than that of pion. Proton track is required to be pointing CES fiducial and different wedges. z_0 distance between proton and pion is at most $2cm$. CTVMFT vertex fit is applied and $Prob(\chi^2) > 0.1\%$, $L_{lxy} > 0.85cm$ and impact parameter of $\Lambda^0 < 0.007cm$ cuts are required.

A.4 $K_s \to \pi^+\pi^-$ sample

Two track trigger dataset (xbhd0d) is used to obtain K_s^0 sample. Level 3 trigger bit "B_CHARM" is chosen. Tracks are selected to satisfy same quality cuts as Bc analysis. Additionally impact parameter around beam line is required to be at least 2 sigma. 2 tracks are required to be pointing CES fiducial and different wedges. CTVMFT vertex fit is applied and $Prob(\chi^2) > 0.1\%$ and $L_{lxy} > 0.85cm$ is required. Sideband is subtracted in mass($\pi\pi$) to obtain pion signatures.

SUNGKYUNKWAN UNIVERSITY

Appendix B

$b\bar{b}$ Monte Carlo simulation in Pythia

B.1 $b\bar{b}$ production process

As described in [64], the parton shower model implemented in the Pythia and Herwig Monte Carlo programs is one of approach to estimating the effects of higher-order correction. The parton shower approach is not exact to any order in α_S but rather tries to approximate corrections to all orders by using leading-order matrix elements for the hard two-to-two QCD scatter and adding addition initial and final-state radiation using a probabilistic approach. In this approximation, the diagrams for $b\bar{b}$ production can be divided into three categories:

Flavor Creation(FC) The lowest-order two-to-two QCD $b\bar{b}$ production diagrams including $q\bar{q}$ annihilation and gluon fusion, plus higher-order corrections to these processes. Since this process is dominated by two-body final states, back-to-back events in $\Delta\phi$ and balanced p_T events tend to be generated.

Flavor Excitation(FE) $b\bar{b}$ pair is generated from the sea quarks of the proton or anti-proton and one of b quark is excited in the hard QCD interaction with a parton from the other beam particle. Produced b quarks

SUNGKYUNKWAN UNIVERSITY

tend to have asymmetric p_T and one of b quarks will be produced with high rapidity.

Gluon Splitting(GS) $b\bar{b}$ pair arises from $g \to b\bar{b}$ splitting in the initial or final state. Neither of the b quarks from the $b\bar{b}$ pair participate in the hard QCD scatter. Depending on the p_T, gluon splitting production tends to have small opening angle.

B.2 Generating $b\bar{b}$

Pythia is used to generate $b\bar{b}$ event sample. Flavor creation, flavor excitation, and gluon splitting mechanisms do not interfere with each other in the parton shower model, each mechanism is generated separately following Kevin Lannon's study [61]. Offline version 5.3.3 is used for the full simulation, where Pythia version is 6.216. CTEQ5L PDF and PARP(67)=4.0 with "Underlying Event Tuning A" are chosen since PRD paper [64] concludes reasonable matching to data with this setting.

B.3 Decay force

To perform $b\bar{b}$ simulation more efficiently, decay force is necessary. QQ Module decayer is chosen. In that module, only $\bar{b}$ side decays are forced (b side decays are not touched at all). Every B hadrons in $\bar{b}$ quark side are forced to J/ψ, and J/ψ to $\mu^+\mu^-$ pair, where $b \to \chi_{c0} \to J/\psi$, $b \to \chi_{c1} \to J/\psi$, $b \to \chi_{c2} \to J/\psi$, $b \to \psi(2S) \to J/\psi$ are also included, and their branching ratios are properly recalculated.

B.4 FC/FE/GS normalization

Three MC samples are prepared, then combining them into one is necessary. To do that, fraction of the three process has to to be known. Pythia predicts cross section of $b\bar{b}$ production for each process. Form Kevin Lannon's study

SUNGKYUNKWAN UNIVERSITY

in CDFNote 6254, the fraction of FC:FE:GS cross section with such a Pythia setting is 29.9%:50.9%:19.2%, where one of B hadrons has $p_T > 5.0GeV$, $|\eta| < 1.0$. $B^+ \rightarrow J/\psi K^+$ event within such kinematic range is used to normalize them. This channel is also used to normalize to data. Yields of $B^+ \rightarrow J/\psi K^+$ events for each MC sample are shown in Fig. B.1.

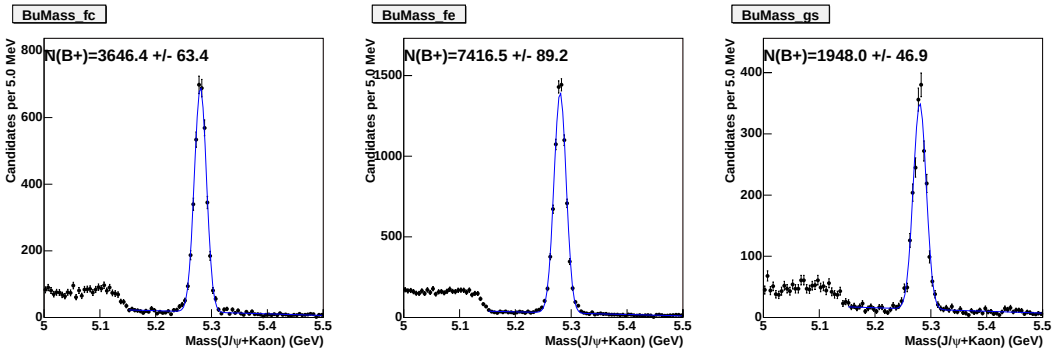

Figure B.1: $B+$ yield of each MC sample, flavor creation(left), flavor excitation(center), and gluon splitting(right).

SUNGKYUNKWAN UNIVERSITY

SUNG KYUN KWAN UNIVERSITY

Bibliography

[1] J.D.Bjorjen, draft report 07/22/86 (1986) [unpublished].

[2] C.-H. Chang, Y.-Q. Chen, "Hadronic production of the B_c meson at TeV energies," Phys, Rev.D **48** (1993) 4086; Ch.-H. Chang, Y,-Q. Chen, G.-P. Han , H.-T. Jiang, AS-ITP-94-24, hep-ph/9408242.

[3] V.V.Kiselev, "Hard approximation in two particle hadronic decays of B_c at large recoils," Phys.Lett **B372**, 326 (1996) hep-ph/9605451.

[4] C.-H. Chang *et al.*, "A Study of b quark fragmentation into B^0 and B^+ mesons," Phys. Lett **B364**, 78 (1995)

[5] K. Kolodziej, A. Leike, R. Rückl, "Photonic production of P wave states of B_c mesons ," Phys. Lett **B355**, 337 (1995);

[6] A.V. Berezhnoy, V.V. Kiselev, A.K. Likhoded, "Photonic production of S and P wave B_c state and doubly heavy baryons," Z. Phys **A356**, 79 (1996).

[7] A. V. Tkabladze,"Physics of B(c) mesons," Phys. Usp. **38**, 1 (1995) [Usp. Fiz. Nauk **165**, 3 (1995)] hep-ph/9504319.

[8] V. V. Kiselev, A. K. Likhoded and A. V. Tkabladze, "Hadronic Production Of Mixed Flavor Heavy Particles," Sov. J. Nucl. Phys. **46**, 535 (1987) [Yad. Fiz. **46**, 934 (1987).

[9] S. S. Gershtein, A. K. Likhoded and S. R. Slabospitsky, "General Characteristics Of B(C) Mesons. Production Mechanisms And Decays," Int. J. Mod. Phys. A **6**, 2309 (1991);

SUNG KYUN KWAN UNIVERSITY

[10] D. Ebert, R. N. Faustov and V. O. Galkin, "Properties of heavy quarkonia and B/c mesons in the relativistic quark model," Phys. Rev. D **67**, 014027 (2003) hep-ph/0210381.

[11] D. Ebert, R. N. Faustov and V. O. Galkin, "Properties of heavy quarkonia and B/c mesons in the relativistic quark model," Phys. Rev. D **67**, 014027 (2003) hep-ph/0210381.

[12] N. Brambilla and A. Vairo, "The B/c mass up to order alpha(s)**4," Phys. Rev. D **62**, 094019 (2000) hep-ph/0002075.

[13] L. P. Fulcher, "Phenomenological predictions of the properties of the B/c system," Phys. Rev. D **60**, 074006 (1999) hep-ph/9806444].

[14] K. Anikeev *et al.*, "B physics at the Tevatron: Run II and beyond," hep-ph/0201071.

[15] M. A. Shifman, A. I. Vainshtein and V. I. Zakharov, "QCD And Resonance Physics: Applications," Nucl. Phys. B **147**, 448 (1979),

[16] V. A. Novikov, L. B. Okun, M. A. Shifman, A. I. Vainshtein, M. B. Voloshin and V. I. Zakharov, "Charmonium And Gluons: Basic Experimental Facts And Theoretical Introduction," Phys. Rept. **41**, 1 (1978);

[17] L. J. Reinders, H. Rubinstein and S. Yazaki, "Hadron Properties From QCD Sum Rules," Phys. Rept. **127**, 1 (1985).

[18] T.Mannel, G.A.Schuler, "Hadronic decays of excited heavy quarkonia ," Z. Phys. **C67**, 159 (1995).

[19] V. V. Kiselev, "Semileptonic B $\to$ D* lepton neutrino decays: The Slope of Isgur-Wise function and |V(bc)| value in potential quark model," Mod. Phys. Lett. A **10**, 1049 (1995) hep-ph/9409348.

[20] V. V. Kiselev, "Model for gluon propagator from analysis in renormalization group," Mod. Phys. A**a9**, 4987 (1994).

SUNG KYUN KWAN UNIVERSITY

[21] V.V.Kiselev, A.K.Likhoded, A.V.Tkabladze, "Production of four heavy quarks and B_c mesons at the Z_0 boson ploe," Phys. Atom. Nucl. **56**, 643 (1993), Yad. Fiz. **56**, 128 (1993).

[22] V.V.Kiselev, A.K.Likhoded, A.E.Kovalsky, "B(C) decays and lifetime in qcd sum rules," Nucl. Phys. **B585**,353 (2000),

[23] S. S Gershtein,*et el.*, "Theoretical status of the B_c meson," preprint IHEP 98-22 (1998) hep-ph/9803433

[24] V.V.Kiselev, "Exclusive Decays and Lifetime of B_c meson in QCD rum rules," hep-ph/0211021 (7 Feb 2003).

[25] V.V.Kiselev, "Decay of the B_c meson," hep-ph/0308214 (21 Aug 2003).

[26] S. S. Gershtein,*et el.*, "Spectroscopy of doubley heavy baryons," Heavy Ion Phys.**9**:133-144,1999, Phys.Atom.Nucl.**63**, 274 (2000), Yad.Fiz.**63**, 334 (2000)

[27] S.Godfrey, "Spectroscopy of B_c mesons in the relativized quark model," Phys.Rev.D **70**,054017 (2004).

[28] I.P. Gouz, *et el.*, "Prospects for the B_c studies at LHCb," Phys.Atom.Nucl.**67**, 1559 (2004), Yad.Fiz.**67**, 1581 (2004) hep-ph/0211432

[29] C.-H. Chang, *et el.*, "BCVEGPY: An event generator for hadronic production of the B_c meson" , Comput.Phys.Commun.**159**,192 (2004) hep-ph/0309120

[30] C.-H. Chang, *et el.*, "Uncertainties in estimating haronic production of the B_c and comparisons between Tevatron AND LHC," Eur.Phys.J.**C38**,267 (2004) hep-ph/0309121

[31] E.J.Eichten and C. Quiqq, "Mesons with beauty and charm: Spectroscopy," Phys.Rev.D **49**,5845 (1994).

[32] J. Cockcroft and E. Walton. Proc. Roy. Soc., 136:619, 1932

SUNG KYUN KWAN UNIVERSITY

[33] W. K. H. Panofsky *et al.,* Berkeley Proton Linear Accelerator. Rev. Sci. Instrum., 26:111, 1955.

[34] D. Mohl, G. Petrucci, L. Thorndahl, and Simon Van Der Meer. Physics and Technique of Stochastic Cooling. Phys. Rept., 58:73-119, 1980.

[35] `http://www-cdfonline.fnal.gov/opshelp/stores/`

[36] `http://www-cdf.fnal.gov/internal/people/links/JacoboKonigsberg/instr02.ps`

[37] S. Kilemnko *et al.*, "The CDF Run II Luminosity Monitor," CDF Note 4330.

[38] Muge Karagoz Unel and Richard Tesarek, "Beam Halo Monitoring at CDF," Nucl. Instrum. Meth. A **506**, 7 (2003), FERMILAB-PUB-02/304-E.

[39] S. Nahn, "Status of the CDF Run II Silicon Detector," CDF Note 6264.

[40] COT group, A. Mukherjee, R. Wagner, "CDF Central Outer Tracker," Nucl. Instrum. Meth. A **526**, 249 (2004), CDF Note 6267.

[41] Shin-Shan Yu *et al.*, "COT dE/dx Measurement and Corrections," CDF Note 6361.

[42] K. Anikeev *et al.*, "Construction and Installation of the CDF Time-Of-Flight Counters for Run II," CDF Note 5818.

[43] C. Grozis *et al.*, "The Time-Of-Flight Detector at CDF," Nucl. Phys. Proc. Suppl. A **47**, 344 (2001); Int. J. Mod. Phys. A16S1C, 1119 (2002).

[44] F. Abe *et al.*, Nucl. Instrum. Meth. A **271**, 387 (1988).

[45] CDF Collaboration, F. Abe *et al.*, Phys. Rev. D **52**, 4784 (1995) and D. Acosta *et al.*, Phys. Rev. D **65**, 112003 (2002).

[46] *The CDF II Detector Technical Design Report,* FERMILAB-PUB-96/390-E (1996).

SUNGKYUNKWAN UNIVERSITY

[47] F.Abe,*et el.*,The CDF Collaboration, "Observation of B_c mesons in $p\ \bar{p}$ collisions at $\sqrt{s} = 1.8TeV$," Phys.Rev.D **58**, 112004 (1998).

[48] "http://www-cdf.fnal.gov/internal/physics/bottom/bpak/" under "B Analysis Basics".

[49] M.Campanelli and E. Gerchtein, "Calibration of the momentum scale for Kalman refitter using J/ψ events," CDF Note 6905.

[50] S. D'Auria *et el.*, "Track-based calibration of the COT specific ionization," CDF Note 6932.

[51] J. Bellinger *et el.*, "A Guide to Muon Reconstruction for Run 2," CDF Note 5870.

[52] T. Moulik *et el.*, "B Flavor tagging using opposite side electrons," CDF Note 6793.

[53] C. Campagnari *et el.*, "Low p_T electron identification," CDF Note 2161.

[54] T. Moulik, "Offline Central PreRadiator Reconstruction in RunIIa," CDF Note 6192.

[55] M. Riveline, "CES Clustering in Run II," CDF Note 5863.

[56] A.Cerri *et el.*, "D^0 Studies Using SVT Special Runs," CDF Note 5771.

[57] S. Yu *et el.*, "COT dE/dx Measurement and Corrections," CDF Note 6361.

[58] S. D'Auria *et el.*, "Search of a $B_c \to J/\psi\pi$ signal: Monte Carlo validation," CDF Note 7018.

[59] K. Anikeev *et el.*, "B Meson Lifetime Measurements Using Exclusively Reconstructed Decays $B \to J/\psi X$," CDF Note 6266.

[60] P. Luckens, "A technique for photon convesion detection, applications for material," CDF Note 2797.

SUNGKYUNKWAN UNIVERSITY

[61] K. Lannon and K. Pitts, "Bottom Quark Production Using Pythia and Herwig," CDF Note 6253.

[62] CDF b-Group MonteCarlo page: "http://www-cdf.fnal.gov/internal/physics/bottom/b-montecarlo/".

[63] R.Field, "The Sources of b-Quarks at the Tevatron and their Correlations," Phys.Rev.D**65**, 094006 (2002)

[64] K.Lannon *et al.*, "Measurements of Bottom Quark-Antiquark Azimuthal Production Correlations," Phys.Rev.D **71**, 71092001 (2005)

[65] D. Acosta *et al.* The CDF Collaboration, "Measurement of the J/ψ meson and b-hadron production cross sections in $p\bar{p}$ collisions at $\sqrt{s} = 1.96\ TeV$," Phys.Rev.D **71**, 032001 (2005).

[66] CDF B_s working group, "Scale Factors for Proper Time Uncertainties," CDF Note 7500.

[67] S. D'Auria *et el.*, "Brahching ratios and direct CP violation in Cabibbo supressed decays of D^0," CDF Note 6391.

[68] D. Amidei *et el.*, "Measurements of $\sigma * Br(W \to e\nu)$, $\sigma * Br(Z \to ee)$ and the ratio R using CDF Run II Data," CDF Note 6681

[69] M. Coca *et el.*, "$W \to e\nu$ Cross Section Analysis with Run II Data," CDF Note 6300.

[70] D.Glenzinski *et el.*, "Measurement of Level 1, 2 and 3 low p_T dimuon efficiencies for the $B_s \to \mu\mu$ analysis," CDF Note 7314.

[71] S. Eidelman *et el.*, Phys.Lett. **B592**,1 (2004).

SUNGKYUNKWAN UNIVERSITY